2

Synthesis and Advanced Structural and Magnetic Characterization of Mesoporous Transition Metal–doped SnO₂ Powders and Films

Junpeng Fan

Tesi Doctoral

Programa de Doctorat en Ciència de Materials

Eva Pellicer Vilà (directora i tutora)

Jordi Sort Viñas (director)

Miguel Guerrero Hernández (director)

Departament de Física

Facultat de Ciències

2017

Memòria presentada per aspirar al Grau de Doctor per

Junpeng Fan

Vist i plau

Dra. Eva Pellicer Vilà

(directora i tutora)

Prof. Jordi Sort Viñas Hernández

Dr. Miguel Guerrero

(director)

(director)

Bellaterra, 01/09/2017

Group of smart nanoengineered materials, nanomechanics and nanomagnetism

La **Dra. Eva Pellicer Vilà**, investigadora Ramón y Cajal del Departament de Física de la Universitat Autònoma de Barcelona,

El **Prof. Jordi Sort Viñas**, professor ICREA del Departament de Física de la Universitat Autònoma de Barcelona,

i el **Dr. Miguel Guerrero Hernández**, investigador del Departament de Física de la Universitat Autònoma de Barcelona,

CERTIFIQUEN:

Que **Junpeng Fan** ha realitzat sota la seva direcció el treball d'investigació que s'exposa a la memòria titulada "*Synthesis and Advanced Structural and Magnetic Characterization of Mesoporous Transition Metal–doped SnO_2 Powders and Films*" per optar al grau de **Doctor per la Universitat Autònoma de Barcelona**.

Que el disseny dels experiments, síntesi de mostres, llur caracterització, l'anàlisi dels resultats, la redacció dels articles i d'aquesta memòria són fruit del treball d'investigació realitzat per Junpeng Fan.

I perquè així consti, signen el present certificat,

Dra. Eva Pellicer Vilà   Prof. Jordi Sort Viñas   Dr. Miguel Guerrero Hernández

Bellaterra, 1 de setembre de 2017

Acknowledgments

First, I would like to thank my supervisors Dr. Eva Pellicer and Prof. Jordi Sort, for their support, patient guidance and kind advices. I would also like to thank my supervisor Dr. Miguel Guerrero, who helped me to properly design the experiments and improve my academic writing skills. In a word, thanks to all of you for helping me to broaden my research horizons in nanomaterials science and magnetism fields.

I would like to thank Prof. Maria Dolors Baró and Prof. Santiago Suriñach for their fruitful advices and help in all the aspects. Similarly, I would like to thank Dr. Jordi Malapeira for his patient explanations.

I am grateful to all co–authors of the articles I have published or submitted so far.

I would also like to thank all the lab–mates who have shared the lab life with me: Alberto, Doga, Enric, Evangelia, Jordina, Pau, Irati, Jin, Feng and Shauna.

It is a great pleasure to acknowledge the support and help coming from the technicians from the Microscopy and X–ray Diffraction services at UAB, ICMAB, Scientific and Technological Centers (CCiTUB) from University of Barcelona, ICN2 and Helmholtz–Zentrum Berlin for their assistance in SEM, TEM, XRD, EELS, and XMCD analyses.

Thanks to the grant from China Scholarship Council (CSC). Without that, I would not have the chance to pursue my PhD at UAB. What is more, without it, I would not have this unforgettable experience in this fascinating country.

I would like to thank my Chinese friends Wenjie, Changyong, Chunyi and Yu for their help while living abroad. I am also grateful for the support of my girlfriend, Flavia Tan. Thanks for your companionship.

Thanks to my mother and father for their understanding and encouragement. I am very grateful that they always stand by my side and support my choice.

Finally, I would like to thank myself. Thanks for your choice to study abroad. It is not easy, but you have persisted in order to obtain it. In the future days, I hope you can go beyond yourself, to achieve the wildest dreams. Please remember, life is never easy for those who dream.

Junpeng Fan

Abstract

This Thesis dissertation covers the synthesis by means of nanocasting and evaporation–induced self–assembly (EISA) methods as well as the advanced characterization of Ni, Cu–doped mesoporous SnO_2 powders and films. The origin of the magnetic properties in these materials is also discussed in detail.

Firstly, ordered mesoporous SnO_2 powders doped with different Ni amounts were synthesized by nanocasting from mesoporous KIT–6 silica. Successful replication of the silica template was verified by scanning electron microscopy. No extra phases attributed to Ni or NiO were detected in the corresponding X–ray diffractograms except for the sample with the highest doping amount (e.g., 9 at.% Ni), for which NiO as secondary phase was observed. The oxidation state and spatial distribution of Ni in the powders was investigated by X–ray photoelectron spectroscopy and electron energy loss spectroscopy, respectively. Ni–containing powders exhibit ferromagnetic response at low and room temperatures, due to uncompensated spins at the surface of NiO nanoparticles and the occurrence of oxygen vacancies.

Secondly, continuous mesoporous Ni–doped SnO_2 thin films were synthesized from variable [Ni(II)]/[Sn(IV)] molar ratios through a sol–gel based self–assembly process, using P–123 triblock copolymer as a structure directing agent. A deep structural characterization revealed a truly 3–D nanoporous structure with thickness in the range of 100–150 nm, and average pore size about 10 nm. Grazing incidence X–ray diffraction experiments indicated that Ni had successfully substituted Sn in the rutile–type lattice, although energy–dispersive X–ray analyses also revealed the occurrence of small NiO clusters in the films produced from high [Ni(II)]/[Sn(IV)] molar ratios. Interestingly, the magnetic properties of these mesoporous films significantly vary as a function of the doping percentage. The undoped SnO_2 films exhibit a diamagnetic behaviour, whereas a clear paramagnetic signal with small ferromagnetic contribution dominates the magnetic response of the Ni–doped mesoporous films.

Thirdly, the magnetic properties of ordered mesoporous Cu–doped SnO_2 powders, prepared by hard–templating from KIT–6 silica, were also studied. While Fe contamination or the presence of oxygen vacancies might be a plausible explanation of the room temperature ferromagnetism, the low–temperature ferromagnetism was mainly and uniquely assigned to the nanoscale nature of the formed antiferromagnetic CuO nanoparticles (uncompensated spins and shape–mediated spin canting). The reduced blocking temperature, which resided between 30 and 5 K, and small vertical shifts in the hysteresis loops confirmed size effects in the CuO nanoparticles.

Resum

Aquesta Tesi doctoral comprèn la síntesi mitjançant nanoemmotllament (de l'anglès, *nanocasting*) i autoassemblatge per evaporació induïda (de l'anglès, *evaporation–induced self–assembly*) i la caracterització exhaustiva de pols i capes de SnO_2 mesoporós dopat amb Ni i Cu. L'origen de les propietats magnètiques d'aquests materials es discuteix en detall.

En primer lloc, es van sintetitzar per nanoemmotllament a partir de motlles de sílice KIT–6, pols mesoporosa ordenada de SnO_2 dopada amb diferents quantitats de Ni. Es va verificar la replicació correcta del motlle de sílice mitjançant microscòpia electrònica de rastreig. No es van detectar fases extres atribuïbles a Ni o NiO en els corresponents difractogrames excepte per a la mostra amb el dopatge més alt (9 at.% Ni), per a la qual es va observar la presència de NiO com a fase secundària. Es va estudiar l'estat d'oxidació i la distribució espaial de Ni en la pols mitjançant espectroscòpia fotoelectrònica de raigs X i espectroscòpia de pèrdua d'energia d'electrons, respectivament. Les mostres dopades amb Ni presenten resposta ferromagnètica tant a temperatura ambient com a baixa temperatura, com a conseqüència de la presència d'espins no compensats a la superfície de nanopartícules de NiO i vacants d'oxigen.

En segon lloc, es van sintetitzar capes primes contínues i mesoporoses de SnO_2 dopades amb Ni a partir de diferents relacions molars [Ni(II)]/[Sn(IV)] mitjançant un procés d'autoassemblatge sol–gel, utilitzant el copolímer tribloc P–123 com a agent director d'estructura. Una caracterització estructural profunda va evidenciar l'obtenció d'una estructura nanoporosa 3–D, de gruix comprès entre els 100 i 150 nm, i mida de porus de 10 nm. Els experiments de difracció de raigs X d'incidència rasant van posar de manifest que el Ni ocupava posicions substitucionals en la xarxa tipus rutil del SnO_2, tot i que les anàlisis per dispersió d'energies de raigs X també van revelar la presència de petits clústers de NiO en les capes produïdes a partir de les relacions molars [Ni(II)]/[Sn(IV)] més elevades. Convé remarcar que les propietats magnètiques de les capes mesoporoses varien significativament en funció del percentatge de dopant. Les capes de SnO_2 no dopades presenten un comportament diamagnètic, mentre que les dopades amb Ni mostren un clar senyal paramagnètic amb una petita contribució ferromagnètica.

En tercer lloc, també es van estudiar les propietats magnètiques de pols mesoporosa ordenada de SnO_2 dopada amb Cu, obtinguda mitjançant nanoemmotllament a partir de sílice KIT–6. Per bé que una eventual contaminació amb impureses de Fe or la presència de vacants d'oxigen podrien explicar el comportament ferromagnètic observat a temperatura ambient, el ferromagnetisme a baixa temperatura es va atribuir únicament a la naturalesa nanoestructurada de les nanopartícules antiferromagnètiques de CuO formades (espins no compensats i *shape–mediated spin canting*). La menor temperatura de bloqueig, situada entre 30 i 50 K, i l'existència de petits desplaçaments verticals en els cicles d'histèresi van confirmar efectes de mida en les nanopartícules de CuO.

Glossary

- AFM: atomic force microscopy
- BET: Brunauer–Emmett–Teller
- CTAB: cetyltrimethylammonium bromide
- CMC: critical micelle concentration
- CVD: chemical vapour deposition
- DMIs: diluted magnetic insulators
- DMSs: diluted magnetic semiconductors
- DSSCs: dye–sensitized solar cells
- EDX: energy dispersive X–ray spectroscopy
- EELS: electron energy loss spectroscopy
- EISA: evaporation–induced self–assembly
- FE–SEM: field emission scanning electron microscopy
- FFT: fast Fourier transform
- GMR: giant magnetoresistance
- H_C: coercivity
- HR: high resolution
- M_r: remanent magnetization
- M_s: saturation magnetization
- MAUD: materials analysis using diffraction

- MS: mesoporous silica
- PCEs: power conversion efficiencies
- PSCs: perovskite–base solar cells
- RKKY: Ruderman–Kittel–Kasuya–Yosida
- SAED: selected area electron diffraction
- SQUID: superconducting quantum interference device
- STEM: scanning transmission electron microscopy
- T_C: Curie temperature
- T_N: Néel temperature
- TEM: transmission electron microscopy
- TEOS: tetraethyl orthosilicate
- THF: tetrahydrofuran
- TM: transition metal
- VSM: vibrating sample magnetometry
- XAS: X–ray absorption spectroscopy
- XMCD: X–ray magnetic circular dichroism
- XPS: X–ray photoelectron spectroscopy
- XRD: X–ray diffraction

Preface

The contents of this Thesis have been organized in different chapters as follows:

- **Chapter 1 Introduction:** This chapter covers the concept of mesoporous materials and describes common methods to synthesize mesoporous metal oxides, with special emphasis on the processes of nanocasting and evaporation–induced self–assembly. Furthermore, the basic principles of magnetism and the state–of–the–art of diluted magnetic semiconductors are also introduced.

- **Chapter 2 Experimental section:** This chapter describes, in brief, the various techniques used for the synthesis and characterization of the transition metal–doped SnO_2 powders and thin films (e.g., electron microscopies, X–ray diffraction, electron energy–loss spectroscopy and X–ray magnetic circular dichroism) and provides information on the working conditions.

- **Chapter 3 Results and discussion:** In this chapter, the main results related to the morphology, structure, and magnetic behaviour of transition metal–doped mesoporous SnO_2 powders and thin films are presented and thoroughly discussed.

- **Chapter 4 General conclusions:** This chapter presents the general conclusions and the main contributions brought by this PhD.

- **Chapter 5 Further perspectives:** Future perspectives are briefly outlined.

Table of contents

List of Figures

2

List of tables

1. Introduction

This chapter aims to introduce the basic concepts related to mesoporous materials, as well as the types of mesoporous materials that have been synthetically produced.

1.1 General introduction to micro– and mesoporous materials

Porous materials are classified into several types depending on their pore size. According to The International Union of Pure and Applied Chemistry notation [1], *microporous* materials have pore widths smaller than 2 nm, *mesoporous* materials possess pore widths between 2 and 50 nm, while *macroporous* materials have pore widths larger than 50 nm. Likewise, the IUPAC establishes that mesoporous materials can show either an ordered or disordered arrangement of pores. Hence, a mesoporous material can be regarded as a solid with certain degrees of porosity and long–range order.

Some examples of porous materials are zeolites, porous coal, alumina, structured silica and metal oxides. Natural zeolites (e.g. analcime, chabazite, clinoptilolite, etc.) are structured porous aluminosilicates with cavities of dimensions in the range from 8 to 10 Å (micropores). Due to their highly–structured pores, zeolites are considered to be a molecular sieve, a term that refers to a particular characteristic of these materials, which means that they possess the aptitude to selectively classify molecules under discrimination by size.[2] Therefore, the maximum size of molecules or ions that can enter zeolite pores is controlled by the dimensions of their channels. Natural zeolites are used in processes to soften water by means of the so–called zeolite ion–exchange softening. In zeolite softening, water containing scale–forming ions, such as calcium and magnesium, passes through a resin bed containing strong acid cation resin in the sodium form. In the resin, the hard ions are exchanged with sodium, and the sodium diffuses into the bulk water solution. Due to their great capacity for ionic exchange and affinity to heavy metals cations (e.g. Strontium–90, Cesium–137), zeolites are used as well in the manipulation and destruction of nuclear residues, because they can absorb radioactive isotopes from the solution and keep them trapped inside their crystalline cage structure. Zeolites react easily with glass and cement systems so that the radioactive residues remain arrested within their host medium and decay to innocuous levels. Zeolites are also used as catalysts in the petrochemical industry.[3] Currently, more than 100 different types of synthetic zeolites have been artificially produced by various routes.

Mesoporous silica (see section 1.2.4) is a mesoporous form of silica and can be regarded as one of the most shining developments in nanotechnology. Mesoporous silicas have been used in diverse applications, such as in stationary phases for liquid chromatography, supports for immobilizing biomolecules, catalysts, agents for polymer reinforcement and hard templates for the preparation of mesoporous carbons.[4]

Porous carbons constitute an important class of non–siliceous based mesoporous materials.[5] One of the synthetic strategies to obtain porous carbon is nanocasting (*vide*

infra), in which the porous carbon is obtained as a reverse copy of an inorganic template, typically mesoporous silica. One of the main types of porous carbons synthesized by nanocasting is the CMK–3. Porous carbon materials can be used in many different applications such as gas storage (H_2, CH_4), lithium battery anodes, electrode double–layer capacitors, support electrocatalysts in fuel cells, and immobilization/adsorption of large biomolecules (enzymes, proteins, drugs, etc.). In all these applications, the porosity of the carbon material is the key property, therefore each of these applications has very specific constraints on the porous structure of the material.

In the last decades, ordered mesoporous silicas and carbons have been used as matrices for the synthesis of mesoporous transition metal oxides,[6] which has widened the range of available materials with pores at the mesoscale. Importantly, these materials show long–range ordering of the mesopores because the replicas inherit the characteristics of the matrices. Today, metal sulphides, metal nitrides, carbonitriles, metal organic frameworks, and composite materials can be also synthesized in mesoporous form. The vast majority of recent works focus on biological applications of mesoporous materials, mainly as drug delivery systems. Other bio–oriented applications include biomass conversion and biofuels, magnetic resonance imaging, ultrasound therapy, enzyme immobilization, antigen targeting, biodegradation of inorganic materials, applications for improved digestion, and antitumor activity.[7] Yet, non–biological applications of mesoporous materials have also been recently pursued like photocatalysis, photo–electrocatalysis, lithium ion batteries, heterogeneous catalysis, extraction of lanthanide and actinide species, CO_2 capturing, and magneto–optical devices, among others. Of them, heterogeneous catalysis has attracted more interest. According to S. L. Suib, there have been over 40,000 articles on mesoporous materials published in the last 4 years and about 1,388 reviews. This is a vivid proof of the interest that mesoporous materials spark worldwide.[7]

1.2 Ordered mesoporous materials prepared by soft–templating method

Soft–templating is defined as a process where organic molecules are used as a (soft) template to produce inorganic porous nanostructures. The removal of the organic molecules results in a negative copy of the parent molecules.

In the last two decades, the synthesis of a wide variety of highly ordered structures, using cationic, anionic and non–ionic surfactants by the soft–templating method has been described.[8,9] This approach is particularly well suited for the synthesis of mesoporous silica

materials. Given that it proceeds via polymerization of silica precursors, it is easily controllable by adjusting the reaction parameters such as pH and temperature.

1.2.1 Surfactants and micelles

Mesoporous Silica (MS) nanopowders and films are obtained from the reaction of silica precursors with a template of micelles formed from a surfactant dissolved in an acid media.

The term 'surfactant' comes from *surface active agent*. Surfactants are amphiphilic organic compounds i.e., they contain both hydrophobic and hydrophilic groups (Fig. 1.1). Therefore, when a surfactant is introduced in a polar solvent like water, the hydrophilic part tends to orientate toward the polar phase, while the hydrophobic part tends to align far away from the solvent, resulting in the formation of micelles.
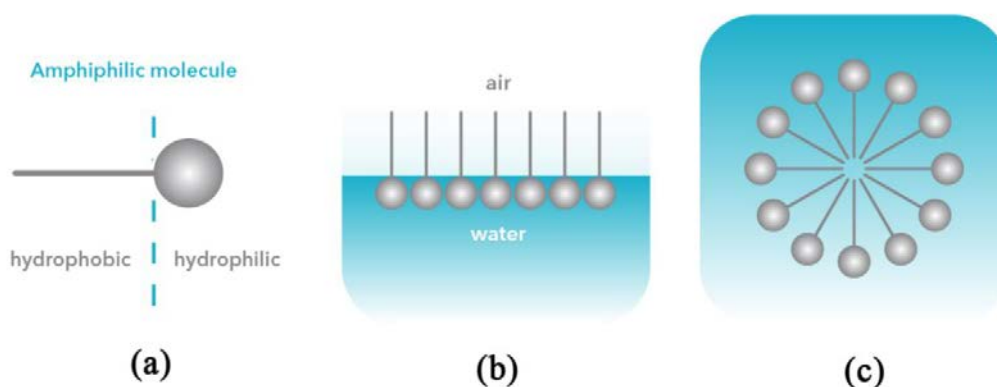
Fig. 1.1 Schematic drawing of a surfactant molecule, (a) an amphiphilic molecule contains hydrophilic and hydrophobic components, (b) the arrangement of amphiphilic molecules at the interface between water and air, (c) the arrangement of amphiphilic molecules in a polar solvent.[10]

The easiest form adopted by a surfactant dissolved in a polar solvent is a sphere. However, the specific shape depends on the conditions and the concentration of the surfactant. For example, the micelles tend to grow and form rods with increasing surfactant concentration. If the surfactant concentration keeps increasing, larger structures such as hexagonal rods and layered structures are formed. Various arrangements of micelles corresponding to different surfactant concentration are shown in Fig. 1.2.

Two basic types of surfactants are used in the synthesis of MS materials: ionic and non–ionic surfactants. An ionic surfactant contains a polar anionic or cationic functional group at the end of its polyether chain. In contrast, a non–ionic surfactant does not contain any charged group in its head. Usually, the derivatives of ethylene oxide and/or propylene

oxide with an alcohol containing an active hydrogen atom (e.g., hydroxyl or carboxyl) are the most common non–ionic surfactants.[11]
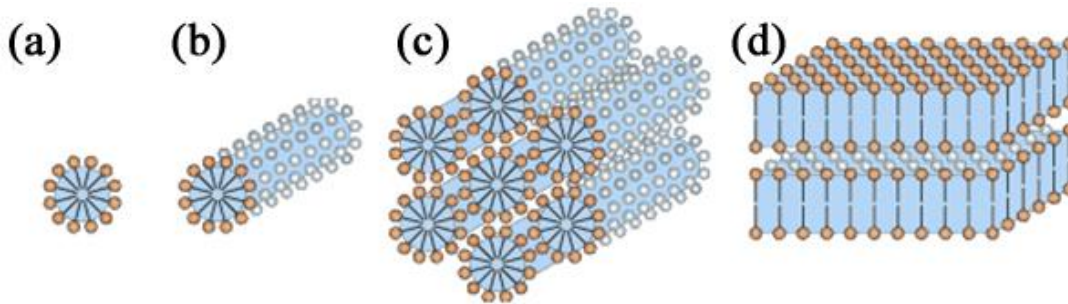
Fig. 1.2 Schematic representation of different types of micelles. (a) sphere, (b) rod, (c) hexagonally packed rods, (d) palisade, layered structure.[12]

1.2.2 Silica polymerization

As discussed above, MS materials are synthesized from the reaction of silica precursors in aqueous solution. Metal alkoxides are one of the most used precursors to synthesize MS materials because they react easily with water. Metal alkoxides are a particular class of organometallic compounds with one or more metal atoms in the molecule. Metal alkoxides (R–OM) can be considered derivatives of alcohols (R–OH) in which a hydroxyl hydrogen is replaced by a metal. The formation of a metal oxide from metal alkoxides proceeds via the connection of metal centers with oxo bridges (M–O–M) or hydroxo (M–OH–M) groups.

The most well–known silica precursors are the alkoxysilanes such as tetramethyl orthosilicate (TMOS) and tetraethyl orthosilicate (TEOS). In the past, many studies focused on the conditions and mechanisms of hydrolysis and polymerization influencing the formation of silica from TEOS.[13]

The chemical formula of TEOS is given by:

$$Si(OCH_2CH_3)_4$$

or

$$Si\,(OR)_4 \quad (R = ethyl)$$
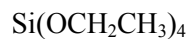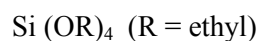
During the hydrolysis reaction, water molecules react with TEOS as follows:

$$Si(OR)_4 + H_2O \rightarrow HO–Si(OR)_3 + R–OH \qquad \text{[eq. 1.1]}$$

$$Si(OR)_4 + 4H_2O \rightarrow Si(OH)_4 + 4R–OH \qquad \text{[eq. 1.2]}$$

14
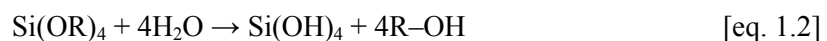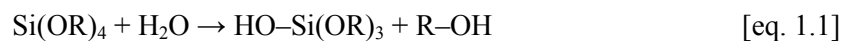
Depending on the amount of water present in the synthesis, partial hydrolysis [eq 1.1] or total hydrolysis [eq. 1.2] of alkoxides groups is achieved.

When two or more molecules are partially hydrolyzed, these undergo a condensation reaction to form siloxane groups [Si–O–Si], releasing smaller molecules like water [eq. 1.3], alcohols [eq. 1.4] or gaseous HCl [eq. 1.5].

$$(OR)_3–Si–OH + HO–Si–(OR)_3 \rightarrow [(OR)_3Si–O–Si \, (OR)_3] + H_2O \qquad [eq. \, 1.3]$$

$$(OR)_3–Si–OR + HO–Si–(OR)_3 \rightarrow [(OR)_3Si–O–Si \, (OR)_3] + R–OH \qquad [eq. \, 1.4]$$

$$(OR)_3–Si–Cl + HO–Si–(OR)_3 \rightarrow [(OR)_3Si–O–Si \, (OR)_3] + HCl \qquad [eq. \, 1.5]$$
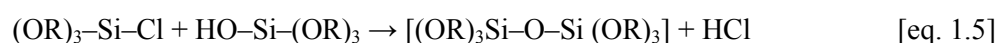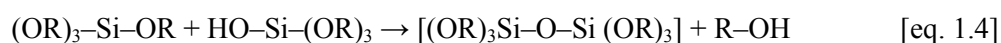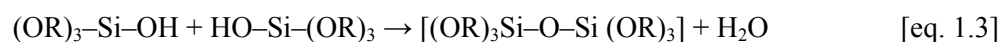
Thus, polymerization of TEOS molecules renders a polysiloxane characterized by complex 1, 2 and 3–dimensional structures which is converted to SiO_2 upon calcination.

1.2.3 Formation mechanism

Since the first ordered MS material, named MCM–41, was reported by scientists from the Mobil Corporation Laboratories in 1992,[14, 15] many research groups have focused their efforts on understanding the influence of surfactants on the synthesis of MS and unraveling the mechanisms leading to ordered mesostructures.

Based on recent developments, two main pathways, *cooperative self–assembly* and *liquid crystal templating processes*, are seemingly efficient to synthesize ordered MS materials from the soft–templating method, as shown in Fig. 1.3.[16] The two types of surfactants previously exposed (non–ionic and ionic) are closely linked with each synthesis pathway. It is worthy to remark that the soft–templating synthesis is rather versatile but also complex and unpredictable. The mesostructures derived from the self–assembly of micelles are greatly dependent on the temperature, the solvent, the concentration, the hydrophobic/hydrophilic properties, the interface interactions, and the ionic strength, among others. This makes any prediction on the resulting mesostructure even more complicated.

• **Cooperative surfactant–templating assembly with inorganic oligomers**

This route is based on the coulombic interaction originated between silica precursors and surfactants due to their opposite electrical charges (Fig. 1.3 (a)). Cetyltrimethylammonium bromide (CTAB) and sodium dodecyl sulfate (SDS) are examples of cationic surfactants, while the oligomers are examples of anionic silica precursors. In the following, to simplify the description, we define S^+ = surfactant cations, S^- = surfactant anions, I^+ = inorganic

precursor cations, I^- = inorganic precursor anions, X^+ = cationic counterions, X^- = anionic counterions.

Silica precursors interact by Coulomb forces in order to minimize the energy of the system. At the interface, silica precursors cooperate in the polymerization, while inorganic outer layers change the charge density. Thus, a change in the charge density that occurs at the interface of surfactants/silica precursors is the mechanism that regulates the assembly process.

After extensive materials research, G. D. Stucky and colleagues proposed four routes to synthesize ordered MS taking advantage of organic–inorganic interactions.[17] These four routes are S^+I^-, S^-I^+, $S^+X^-I^+$ and $S^-X^+I^-$. The first two follow the principle described above, while the latter describes the synthetic mechanism from silica precursors and surfactant with the same charge. These systems involve ions that act as a bridge (i.e., in the acidic environment $S^+X^-I^+ \rightarrow S^+ (XI)^-$, where X = Cl^-, Br^-, I^-).

(a)

(b)
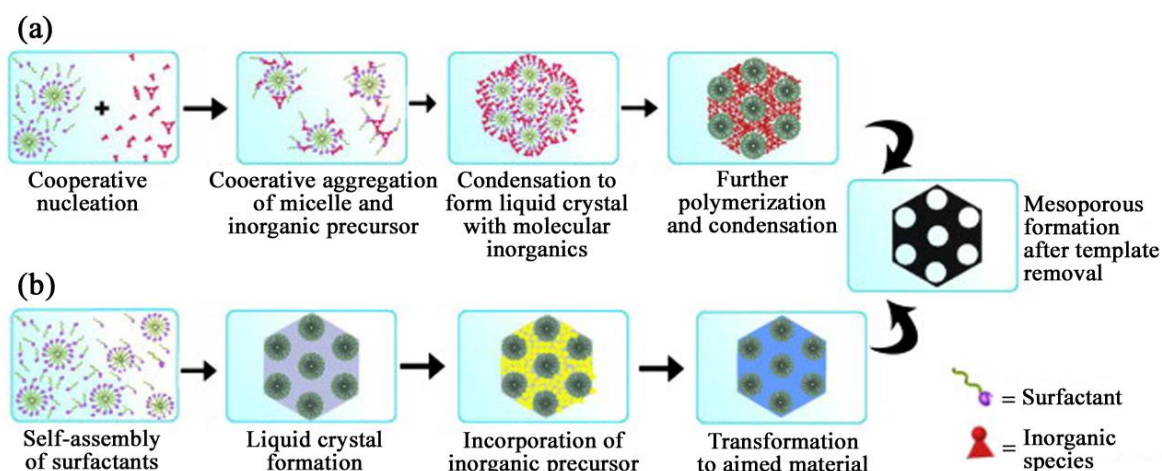
Fig. 1.3 The two mechanisms of soft–templating: (a) cooperative self–assembly and (b) liquid–crystal templating process.[16]

- **Liquid–crystal template pathway**

This route relies on the production of a liquid crystal mesophase from high concentrations of non–ionic surfactants, used as templates (Fig. 1.3 (b)). Recent studies have shown that polymerization (condensation) reaction of inorganic precursors improves when these are confined around the surfactants forming ceramic–like frameworks.[8,18]

High concentrations of surfactant can be obtained using the evaporation–induced self–assembly process, known as EISA (See Section 1.4.1 for more detailed information). EISA, as one of the most promising routes for the large–scale synthesis of ordered MS materials, has shown great flexibility to adapt to the synthesis conditions, offering a greater variety of structures and pore sizes.

These pathways are relatively new. The only requirement for the MS synthesis using non–ionic surfactants is the need for an acid environment to induce TEOS hydrolysis. Diblock and triblock copolymers are typically used as non–ionic surfactants. These surfactants are composed of blocks of different polarity (see Table 1.1). Among all the non–ionic surfactants, Pluronic P–123 is one of the most commonly used triblock copolymers for the synthesis of MS materials. P–123 is composed of 70 polypropylene oxide structural units linked to 20 polyethylene oxide units on each end. Table 1.2 shows a list of non–ionic surfactants employed in the synthesis of mesoporous materials.
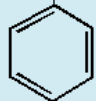
Name	Polypropylene oxide	Polyethylene oxide	Polyethylene	Polystyrene
Abbreviation	PPO	PEO	PE	PS
Chemical formula	$\left(CH_2-CH-O\right)_n$ with CH_3	$\left(CH_2-CH_2-O\right)_n$	$\left(CH_2-CH_2\right)_n$	$\left(CH_2-CH\right)_n$ with phenyl ring
Description	Hydrophobic	Hydrophilic	Hydrophobic	Hydrophobic

Table 1.1 Chemical formulas of some common block copolymers.

Name	PLURONIC® P–123	PLURONIC® F–127	PLURONIC® F–68
Abbreviation	P–123	F–127	F–68
Chemical formula	$PEO_{20}PPO_{70}PEO_{20}$	$PEO_{106}PPO_{70}PEO_{106}$	$PEO_{76}PPO_{29}PEO_{76}$

Table 1.2 Chemical formulas of non–ionic surfactants employed in the synthesis of mesoporous materials.

1.2.4 Typical ordered mesoporous silicas

• 2–D mesoporous silica structures with hexagonal symmetry

The 2–D MS materials with hexagonal symmetry are one of the easiest silicas to obtain. MCM–41, FSM–16, SBA–3, and SBA–15 are examples of this type of MS, which are characterized by being composed of cylindrical pore channels, arranged in hexagonal arrays (P6mm space group).

MCM–41 is obtained using ammonium cationic surfactant templates such as CTAB. Its morphology, pore size, and BET (Brunauer–Emmett–Teller) surface area are highly adjustable during the synthesis steps. The polymerization reaction of silica precursors takes place in alkaline medium (pH $\approx$ 11.5). Non–interconnected cylindrical pore channels,[19] with a diameter between 1.5 and 8 nm and pore wall thickness relatively thin, from 0.6 to 1.2 nm, are obtained. MCM–41 isotherm does not show an obvious hysteresis loop, but the corresponding BET surface area values are relatively high, between 1000 and 1200 m^2/g.[20,21] However, the major limitation of this material is its low hydrothermal stability caused by the thinness of the pore wall.

SBA–15 is obtained under acidic conditions using triblock copolymer surfactants as a template. Actually, the ideal template for SBA–15 synthesis is Pluronic P–123. SBA–15 silica consists of uniform cylindrical pore channels with a pore size from 6.5 to 10 nm, and a pore wall thickness of about 4 nm. In addition to the thicker pore wall compared with MCM–41, SBA–15 exhibits disordered micropores network connecting the cylindrical channels. This microporosity between walls is caused by the penetration of the hydrophobic PPO groups block copolymer chains in the silica matrix. The micro/mesopore ratio can be tuned depending on the application, while keeping the thickness of the pore wall, which confers good hydrothermal stability to the structure.

- **3–D bicontinuous cubic mesoporous silica structures**

Since the discovery of MCM–48, several 3–D bicontinuous cubic silica mesostructures, the SBA–n, KIT–n, AMS–n and FDU–n series have been reported. MCM–48, KIT–6, and FDU–5 with cubic symmetry Ia3̄d and 3–D bicontinuous mesochannels are examples of these types of mesostructures. The best representation of these structures is a gyroid minimal surface, which can be interpreted as two symmetrical sets of cylindrical channels interwoven in a spiral fashion.

The FDU–5 mesostructure was the first bicontinuous cubic mesostructure prepared under acidic conditions.[22] This structure is characterized by the lack of micro–mesoporosity in the silica walls.[23] The pore size of FDU–5 is around 8 nm and it exhibits relatively large BET surface areas (~804 m^2/g) and pore volumes (~1.04 cm^3/g).[24]

MCM–48 is synthesized in the same way as MCM–41, in alkaline conditions with gemini surfactants. The average pore diameter is 2.8–3.4 nm, whereas the pore wall thickness is approximately between 0.8 and 1.0 nm. The specific surface area and pore volume are 660–1010 m^2/g and 0.53–0.80 cm^3/g, respectively.[25,26]

The KIT–6 silica mesostructure is synthesized using a mixture of n–butanol and P–123 as a mesophase under acidic conditions. It was manufactured by Ryoo's group in 2003 for the first time.[27] The pore sizes of KIT–6 can be adjusted in a relatively large range (8–10 nm). Unlike FDU–5 and MCM–48, plenty of disordered microporous or mesoporous tunnels (1–2.5 nm) exist in the pore walls of KIT–6. The specific surface area of KIT–6 is in the range of 527–797 m^2/g, while the pore volume is in the range of 0.73–1.02 cm^3/g.[28] The KIT–6 silica mesostructure has been synthesized in this Thesis to further produce mesoporous SnO_2 replicas by the nanocasting method.

- **3–D cubic mesoporous silica cage–like structures**

The 3–D cubic mesostructures named SBA–16 and FDU–12 belong to the cage–like type and consist of interconnected spherical pores.

The SBA–16 mesostructure is obtained using surfactants with relatively large chains, such as F–127 or P–123. The resultant product is a cubic (Im3m) material with cage–like mesopore sizes between 5–15 nm. Each one is connected with eight neighboring pores whose diameter size is approximately of 4 nm. The specific surface area and pore volume of SBA–16 silica are ~750 m^2/g and ~0.65 cm^3/g, respectively.[29]

The FDU–12 mesostructure has a cubic symmetry (Fm$\bar{3}$m) with cage–like mesopore sizes from 10 up to 12.3 nm. The FDU–12 is synthesized through a similar pathway as for SBA–16. Remarkably, lowering the synthesis temperature and increasing the hydrothermal temperature can expand the pore size to 14–22 nm and the entrance sizes can be adjusted from ~4 to 16.7 nm, respectively.[30,31] Compared with other 3–D cubic mesoporous materials, FDU–12 possesses a higher specific surface area (800–1000 m^2/g), and the pore volume of FDU–12 is between 0.65 and 0.72 cm^3/g.[32]

Schematic representations for 2–D, 3–D bicontinuous cubic, and 3–D cubic cage–like mesoporous silicas are shown in Fig. 1.4 (left, middle and right, respectively).
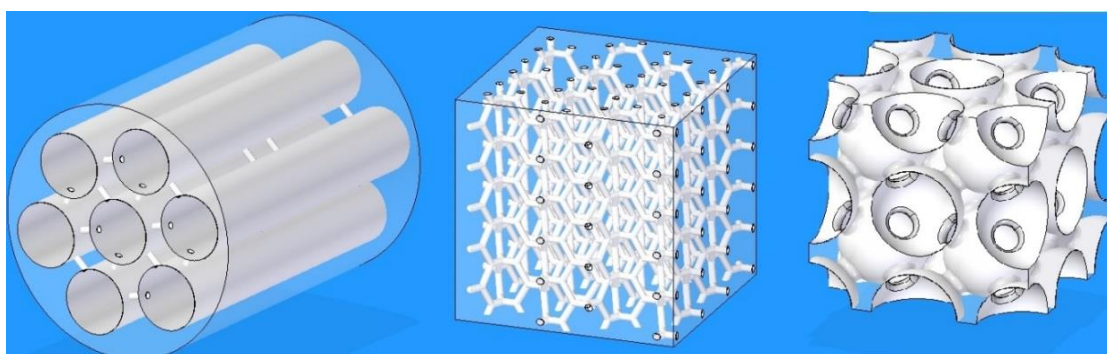
Fig. 1.4 Schematic drawings of mesoporous silicas: 2–D (left), 3–D bicontinuous cubic (middle), and 3–D cubic cage–like (right).

1.3 Ordered mesoporous materials prepared by hard–templating method (nanocasting)

Hard–templating, commonly known as nanocasting, is a process where a precursor, typically a fluid, is infiltrated in the nanosized pore channels of a template which, in turn, has been previously obtained by a soft–template process (section 1.2). The precursor is then confined inside the template and converted into the target product (for example, by annealing in air). When the template is removed after the appropriate treatment, the target product is released and a negative copy of the template is obtained. Thus, the nanocasting process enables an accurate control and prediction of the morphology of the product, as it is defined by the pore architecture of the template. However, the available morphologies of the hard–templated matrices limit the number of structures that can be achieved by the nanocasting process.

1.3.1 The concept of nanocasting

The casting technique dates older than 6,000 years. The casting process involves heating a material that is solid at room temperature until it becomes liquid or enters the plastic regime. The liquid material is then poured into a preformed mold or template, which contains a hollow cavity of the desired shape. Once the liquid material has solidified it is ejected from the mold, thus obtaining a replica of the original template (Fig. 1.5).

Casting has become an important industrial process because it allows both the mass production of solids with complex surfaces with reduced manufacturing times and lower production costs compared to other manufacturing techniques such as machining.
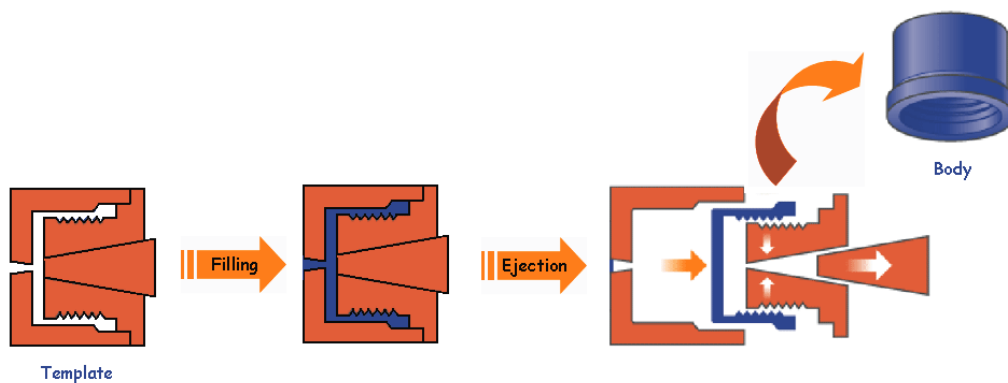
Fig. 1.5 Schematic drawing of the traditional casting process.[33]

The casting process is divided into two distinct subgroups: expendable and non–expendable template casting. The expendable template casting, as the name implies, involves the use of temporary, non–reusable molds and the best known are made of sand or wax. On the contrary, in non–disposable template casting the mold is reusable over time.

However, the technique described above is limited to the macro world, typically for materials in the range of centimeters. Nowadays, advanced engineering applications require nanoscale materials with increasingly complex surfaces that cannot be manufactured by other methods, offering new challenges to researchers.

In 1998, Göltner and coworkers used a porous silica monolith with interconnected pores as a template to prepare mesoporous organic polymer networks with well–defined nanostructure, introducing the nanocasting concept for the first time. [34] Basically, nanocasting involves two main steps: provision of a suitable template and the casting step itself.

1.3.2 The process of nanocasting

- **Formation mechanism**

Precursor infiltration in the pore channels of the mold is the first step in the nanocasting route. Indeed, this can be done by several means. The evaporation–induced capillary condensation consists in diluting the precursor in a volatile solvent to form a dilute solution. This solution is then mixed with the template. The precursor/template weight ratio is calculated based on the density of the precursor and the total pore volume of the template. In most cases, due to the capillary force, the solution infiltrates into the mesochannels of the template. During solvent evaporation, the precursor migrates on the surface, thus filling all the available template voids. The next step is the precursor conversion to the target product and this conversion depends on the type of precursor used. For example, inorganic salts such as nitrates, oxalates, acetates, citrates, etc. decompose at high temperatures, so a heat treatment at high temperatures makes the precursor conversion to the target product feasible. In most cases, only a proportion of the template pores is occupied. In such a case, the precursor molecules must be homogeneously distributed within the mold network so they can retain the mesostructure after template removal. Basically, there are three typical distributions of target products that can retain the mesostructure after removal of the template.

In the first case, the transformation of precursors into the target product takes place in an uncertain channels area as shown in Fig 1.6 (a). The first step of the transformation is nanocrystals nucleation, and the second step is nanocrystals growth. Driven by diffusion and migration, the precursors can transfer from one domain (i.e., the place where the nanocrystal seeds form) to another, until the domain is completely filled with target products.

Metal oxide mesoporous replicas are shining examples of materials synthesized in this way. Although these replicas have the same mesoscopic symmetry as the template used, their

morphology and regular units are smaller. This is because the metal oxides volume conversion ratio is normally less than 15%, so that over 85% of pores remain empty. Several studies recommend subsequent infiltrations in order to minimize the amount of empty pores. However, the choice of two or more infiltrations is limited by the type of MS material used as the template. For example, in 2–D hexagonal structures (SBA–15) precursors are confined inside the channels for further dissemination and migration. Because of its size and channel geometry (1–D), a second infiltration is recommended in this type of structures. In 3–D cage structures (SBA–16 or FDU–12), the target products adopt spherical morphology and then block the channels, [23,35] so that subsequent injections are not always effective.

In the second case, the precursors are dispersed homogeneously within the template cavities as shown in Fig. 1.6 (b). During the precursor transformation into the target product, the mass loss is compensated by volume expansion. This, together with the homogeneity of the infiltration, renders replicas with a regular morphology and structural units similar to the template. Mesoporous carbons are examples of materials synthesized in this way.

In the third case (Fig. 1.6 (c)), due to the strong interaction between the precursor and the template, the precursors are distributed homogeneously on the surface of the pores. If the amount of precursor infiltrated is not enough to fill the template channels, subsequent template removal renders a nanopipes network. This typically happens when the CMK–5 mesostructure is replicated.
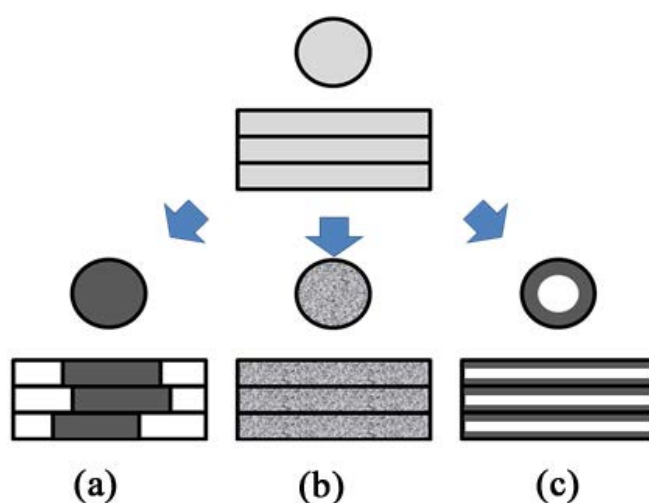
Fig. 1.6 Three typical distributions of precursor inside a mesoporous template: (a) the target product aggregates in small domains inside the mesopore channels, (b) the target product disperses fully and homogeneously in the mesopore channels, (c) the target product is homogeneously distributed on the inner surface of mesopore channels forming a coating.[23]

- **Precursors**

As mentioned above, the main challenge of the nanocasting technique is the capability of filling pores whose diameter ranges between 2 and 50 nm. Although the use of mechanical forces to inject the precursors into the template pores has been recently proven feasible,[36] infiltration by wet chemistry still remains the most useful approach. Hence, infiltration necessarily proceeds via capillary forces and/or hydrophilic affinity between the precursor and the template. During solvent evaporation, ion precursor interacts by intermolecular forces forming aggregates while being adsorbed on the pores surfaces. Thus, the capillary force and the ions mobility on the surface is a key factor affecting the pores filling. If the intermolecular stress interaction of the precursor is strong in relation to the interaction between the precursor and the silica template, the precursor does not penetrate into the pores and tends to form aggregates outside the template. On the contrary, if the precursor intermolecular stress interaction is weak relative to the interaction between the precursor and the silica template, the precursor migrates to any area of the template, clogging pores and creating a coating around the template. Only when there is a balance between template–precursor and precursor–precursor interactions, the template is successfully filled.

Gaseous compounds have also been used to fill the template pores using chemical vapor deposition (CVD) process. However, these processes tend to block the pore entrances, and therefore to form precursor aggregates outside the template. A key parameter that should be adjusted to minimize the aggregation of precursors outside the template is the deposition rate. Fast deposition rates lead to clogged pores, whereas slow deposition rates produce an undercharge of precursor leading to high–quality replicas.

Most frequently, the target product in the nanocasting process is obtained by direct thermal decomposition of the precursor within the template pores. During this step, the precursor must be kept inside the pores otherwise the final product will form outside. Metal chlorides are examples of precursors that can be easily liquefied and therefore tend to move out of the template. Precursor transformation by thermal decomposition generally involves gas formation and other by–products that must be able to leave the pores network of the host. Also, a thermal decomposition has an associated contraction of volume, so the use of precursors with high volume contraction affects the quality of the mesostructure obtained after removing the template. Metal sulfides are examples of precursors with large contraction percentage.

Metal nitrates are the most common precursors used in nanocasting. Unlike metal chlorides, they are retained inside the pores during the whole processing, thus minimizing the formation of aggregates outside the template. However, the theoretical efficiency of metal nitrates transformation into the target product is relatively low. The theoretical efficiency

of a precursor is evaluated through a parameter termed volume contraction ratio [eq. 1.6]. This value can be considered intuitively as the template volume percentage that is occupied by the target product after precursor processing.

$$\text{Vol. contr. ratio} = \frac{\text{Vol. of target product}}{\text{Vol. of precursor}} \qquad [eq.1.6]$$

where,

$$\text{Vol. of target product} = \frac{\text{Molecular weight of target product}}{\text{Density of target product}} \qquad [eq.1.7]$$

$$\text{Vol. of precursor} = \frac{\text{Molecular weight of precursor}}{\text{Density of precursor}} \qquad [eq.1.8]$$

Typical contraction volume ratios of precursors used in the synthesis of mesoporous materials by nanocasting technique are listed in Table 1.3. The volume contraction rate for most inorganic precursors is only 10%, e.g. if precursors infiltration has completely filled the vacancies of the template, after the precursor transformation, only 10% of pores are filled with the target product, while 90% of pores remain empty. Therefore, the particle size of the resulting replica is smaller than that of the parent template.

Precursor	Target product	Volume contraction (%)
$Mg(NO_3)_2 \cdot 6H_2O$	MgO	6.22
$Al(NO_3)_3 \cdot 9H_2O$	Al_2O_3	5.89
$Ti(OC_3H_7)_4$	TiO_2	6.98
$Cr(NO_3)_3 \cdot 9H_2O$	Cr_2O_3	6.56
$Mn(NO_3)_2 \cdot 6H_2O$	MnO_2	10.73
$Fe(NO_3)_3 \cdot 9H_2O$	Fe_2O_3	6.34
$Ni(NO_3)_2 \cdot 6H_2O$	NiO	7.07
$Cu(NO_3)_2 \cdot 3H_2O$	CuO	12.09
$Zn(NO_3)_2 \cdot 6H_2O$	ZnO	10.10
$Zr(NO_3)_4 \cdot 5H_2O$	ZrO_2	9.10
$Co(NO_3)_2 \cdot 6H_2O$	Co_3O_4	8.54

Table 1.3 Target products and typical volume contraction of various precursors used in the synthesis of mesoporous metal oxides.[23]

- **Solvent**

The solvent is also an important factor to be considered in the nanocasting technique. As explained earlier, many precursors require a solvent to be transported and thus infiltrated into the host. Moreover, the choice of the solvent influences the interactions that take place with the template surface pores, changing the wettability and the capillary force. Typically, higher solubility leads to a better filling of precursors and higher efficiency of infiltration. Likewise, inorganic precursor solvation influences the migration and aggregation of them. In general, solvents with a relatively low boiling point such as tetrahydrofuran (THF), water or ethanol, can be used in the nanocasting technique. The first two are not widely used though. Precursors have a low solubility in THF, while water has a strong solvation effect, which promotes the migration and aggregation of the precursors on the template surface pores. Ethanol is the most widely used solvent in nanocasting for many reasons: most inorganic precursors are soluble in ethanol; it has a low boiling point and high volatility; and interacts weakly with precursors, which facilitates the migration and accumulation of these inside the pores. Besides, ethanol provides a number of hydroxyl groups to the system, yielding more hydrophilic domains on the silica surface. Ethanol also has amphiphilic properties compatible with the silica pore wall, which increases the capillary force.

- **Template removal**

Template removal is the last step to obtain replicas by the nanocasting technique. The entire process of nanocasting is shown in Fig. 1.7.
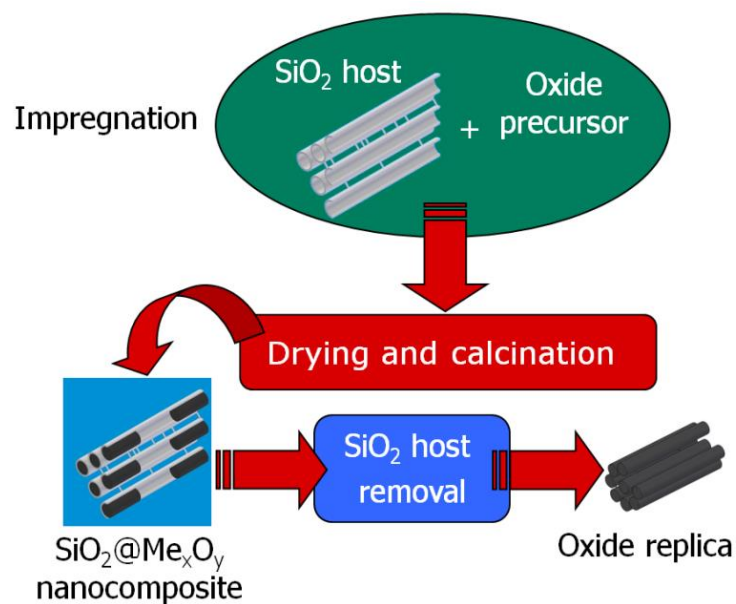
Fig. 1.7 Illustration of the nanocasting process toward mesoporous transition metal oxide powders.

Silica templates can be removed by a dilute HF solution at room temperature or with NaOH solution at ≈ 70 °C. The selection of one or the other depends on the chemical stability of the target product. Removal from HF allows the complete dissolution of the silica template within less than 30 minutes, while the removal with NaOH typically requires 24 h. Although the use of HF reduces the amount of residual silica, its use should be undertaken with extreme caution.

1.4 Mesoporous (metal oxide) thin films

As mentioned above, a large variety of porous materials have been fabricated and successfully used in many different fields.[37,38] However, most of them are synthesized only as particles of different sizes (i.e., in powder form). It is well–known that there are some drawbacks related to particles/powders, such as macroscopic size limit, difficulty to be integrated into devices, or their recovery from a solution (i.e., recycle and reuse). Mesoporous thin films benefit from the advantages of porous structures and overcome these drawbacks. Consequently, mesoporous metal oxide films with different compositions, thickness, and pore topology have been pursued for a variety of applications.[39,40] For example, F. Giordano and co–workers reported on the synthesis of Li–doped mesoporous TiO_2 films. They also demonstrated that, by reducing electronic trap states, the mesoporous films exhibited superior electronic properties.[41] Via surfactant templated method, J. C. Yu and co–workers successfully synthesized transparent zeolite–like mesoporous TiO_2 nanocrystalline thin films with high photocatalytic activity.[42]

1.4.1 Sol–gel synthesis of mesoporous (metal oxide) thin films

The term sol–gel can be broadly defined as the synthesis of solid materials such as metal oxides from solution–state precursors.[43] It involves the preparation of inorganic polymers or ceramics from solution through a transformation from liquid precursors to a sol (colloidal suspension) and finally to a network structure called a 'gel'. A wide range of crystalline and amorphous transition metal oxide structures such as thin films[44,45] or monodisperse particles has been demonstrated by sol–gel.[46]

Besides physical methods to control structure in sol–gel chemistry, templates can also play an important role in introducing both ordered and disordered porosity. For this purpose, soft templates such as amphiphiles, block copolymers, ionic liquids, biopolymers and proteins have been employed in sol–gel syntheses. Alternatively, hard materials such as colloidal particles, bacterial filaments or cellulose nanocrystals are used. In some cases, alkoxides can be modified to enhance interaction of the sol–gel precursors with a soft or a

hard template and produce ordering or porosity on multiple length scales.[47] The template can either be left in the oxide to produce an inorganic/organic nanocomposite or removed by dissolution or calcination.

A particularly important sol–gel derived approach that used amphiphiles for templating sol–gel materials is evaporation–induced self–assembly (EISA). Rather than simple direction of the sol–gel condensation within solution, EISA relies on gradual evaporation of volatile species from the mixture to form a mesophase (see below). Inorganic materials accumulated around this liquid–crystal template, which results in well–ordered mesostructuring in the resulting metal oxide.[43]

1.4.2 Evaporation–induced self–assembly (EISA)

EISA was described for the first time by C. J. Brinker *et al.* in 1999[48] and involves a mixture of sol–gel precursors such as water, ethanol and a metal alkoxide or chloride, combined with amphiphiles such as CTAB or block copolymers. When compared to other synthetic strategies, which are costly and time–consuming, EISA presents several advantages such as a high versatility, short phase formation times and large variety of mesophases.[49] Generally, the organized structures or patterns (Fig. 1.8) are obtained by the solvent evaporation and the spontaneous association of individual components through noncovalent interactions (π–π stacking, hydrogen bonding, etc.).[50,51]
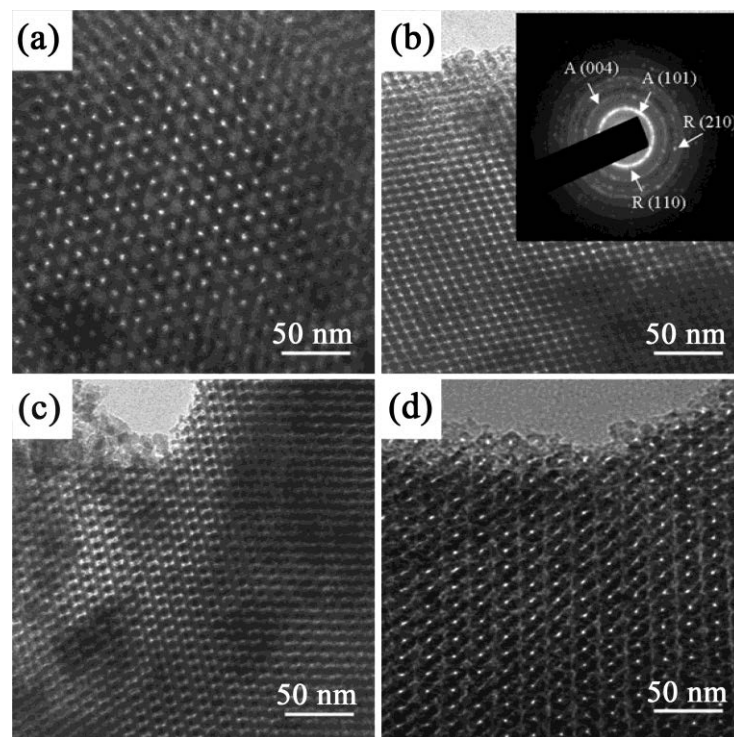
Fig. 1.8 TEM images of mesoporous TiO_2 film synthesized by EISA. The sample was viewed from different planes: (a) [111], (b) [110], (c) [311], (d) [100]. The inset is the corresponding electron diffraction pattern.[52]

In the EISA process, organic–inorganic hybrid building blocks are the most common building blocks used for generating nanoscale porosity in the target material. Usually, the organic parts play the role of structure directing agent, which can form organic templates and contribute to the formation of the porous structure. The general classification of the structure directing agents is shown in Fig. 1.9. Among all the different directing agents that are commonly used, non–ionic block copolymers (e.g. P–123, F–127, Table 1.1 and 1.2, page 16), have recently emerged as a promising tool yield materials with tailored mesostructures, ranging from hexagonally arranged cylinders to three–dimensional bi–continuous cubic networks.[53]
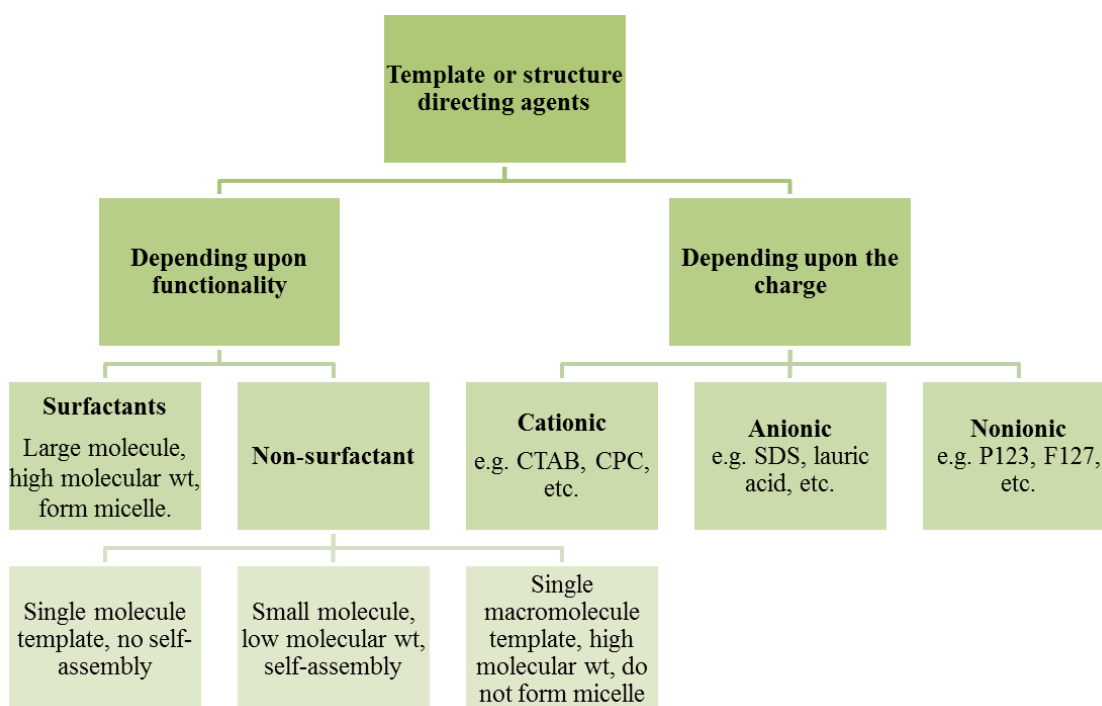
Fig. 1.9 Schematic classification of structure directing agents. CPC: cetylpyridinium chloride, SDS: sodium dodecyl sulphate.

In the formation of mesoporous thin films through EISA method, a homogeneous solution consisting of a soluble metal alkoxide or metal salt precursor and solvent (usually water and/or alcohol) are mixed thoroughly with a structure directing agent at a lower concentration than its critical micelle concentration (CMC).[54] Then, part of the solution is transferred to the substrate surface by spray, spin or dip–coating, In the spin–coating method, a small amount of precursor liquid is dropped on the center of the substrate. Then, the substrate is rotated at a certain speed to spread the material into a uniform thin film by centrifugal force. In the dip–coating method, the film is formed by immersing a substrate in a precursor liquid and then withdrawing it under a well–defined speed and controlled humidity (as shown in Fig. 1.10). Later, the evaporation of the volatile components takes

place at the interface. During this process, the surfactant directing agent molecules, in the form of a lyotropic liquid–crystalline phase, lead to the assembly of an ordered mesostructured composite. Subsequent ageing, thermal treatment, or exposure to acid/base catalysts are used to induce the inorganic precursor condensation and solidify the skeleton.[48] Remarkably, EISA process is tricky and not always evident. Thus, the final morphology of the synthesized materials is determined by many factors, such as the nature of precursors and the template molecule, temperature, solvents, the ratio of the surfactant to the precursor or presence of counter ions in the reaction media. [49,55]

Nowadays, EISA is considered as an efficient method for producing ordered metal oxide thin films, such as TiO_2 with tailored mesostructure,[56] Al_2O_3 coated TiO_2 films for dye–sensitized solar cells,[57] WO_3 thin films with improved electrochromic performance,[58] or Nb_2O_5 films for sensing applications.[59]
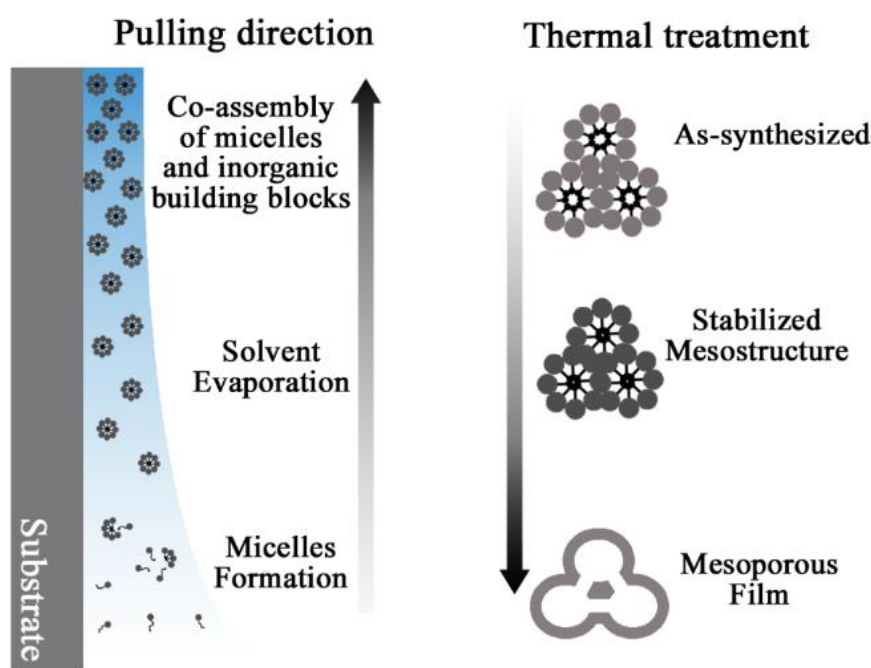
Fig. 1.10 Scheme of the evaporation–induced self–assembly (EISA) process (left). Schematic view of the pore system evolution along the consolidation and thermal treatment processes (right). Adapted from Ref. [60]

As mentioned above, EISA can be considered as a simple, efficient, and rapid method for the fabrication of highly uniform thin films. Furthermore, when EISA process is combined with the dip–coating technique, it is possible to tune the final mesostructure of the film (i.e., sealed cabinet equipped with gas flow controller allows to perfectly adjust the relative humidity of the system). [61,62,63]

1.5 Applications of mesoporous materials

• **Sensors**

Compared with conventional sensors, those in which the active material is mesostructured show several advantages such as enhanced sensitivity and lower detection limits.[64] Consequently, more and more mesoporous materials are currently being fabricated and used for monitoring the concentration of glucose,[65] proteins,[66,67,68] metal cations,[69] or for the detection of the relative humidity.[70,71] In addition, when impregnated with dyes, the resulting hybrid films are very promising for optical sensing applications, such as pH sensing.[72] When a certain material with mesoporous structure is used as a sensor, factors that affect the sensibility and selectivity should be considered, including pore accessibility, the chemical nature of the pore surface and the pore size and topology with respect to the sensing species.[40,73]

• **Photocatalysis**

Because mesoporous materials possess a high surface area, the density of photoactive sites is higher and, therefore, the catalytic activity increases. Mesoporous materials are thus ideal candidate materials for the purification of air and water or the decomposition of pollutants [74,75] and dyes.[76,77] Among all the mesoporous oxides with photocatalytic properties, porous TiO_2 is the most widely studied material.[78] Besides the possibility to tune the morphology and pore accessibility, anions can also be introduced in the TiO_2 matrix to further decrease the bandgap and therefore improve the photocatalytic activity.[79]

• **Solar cells**

Along with the extensive investigation of the 3rd generation photovoltaic devices, mesoporous materials have been widely used as the skeleton structure in dye–sensitized solar cells (DSSCs)[80] and perovskite–base solar cells (PSCs).[81,82] The former is recognized as a cost–effective alternative to conventional silicon photovoltaic devices, while the latter has undergone impressive improvement in power conversion efficiencies (PCEs), jumping from 3.8% to 20.1%.[83,84] In general, mesoporous metal oxides and semiconductor materials are most commonly used as acceptors of the photo–generated electrons. These electrons are produced from dyes or perovskites in intimate contact with the mesoporous materials, which are immediately transmitted to the conductive substrate.

• **Low–k dielectric materials**

Because porosity is one of the factors that considerably affects the performance of low–k dielectric materials, mesoporous materials have attracted much attention in this field. For example, T. Maruo *et al.* reported that the dielectric constant of mesoporous silica films for

ultralarge–scale integrated circuits reduced into the 1.5–1.7 range when treated with trimethyl ethoxysilane.[85] It is well known that water absorption can increase the k value. Thus, hydrophobic surfaces are required to increase the durability of the mesoporous films and avoid the deleterious effects of water absorption.[86,87] Noteworthily, besides the porosity, the magnitude of other factors, such as elastic modulus, thermal stability, hardness and residual stress, thermal expansion coefficient, etc., should also be considered.[88]

• **Electrochromism and photochromism**

It is believed that in the near future smart homes will become a reality. In this context, functional windows[89] and various electronic displays[90,91] will play important roles. Essentially, the electrochromic property of materials is exploited in both cases. Electrochromism is a physical phenomenon where absorption and/or emission of some materials are modified upon applying an external voltage. Tungsten oxide (WO_3) is the dominant electrochromic material. Interestingly, its electrochromic response can be improved by tuning the morphology to achieve superior performances.[92] Because large specific surface areas afford faster insertion kinetics,[93] mesoporous WO_3 films attract a great deal of attention.[94,95,96] Fig. 1.11 shows the typical electrochromic cycles of ordered mesoporous WO_3 films.
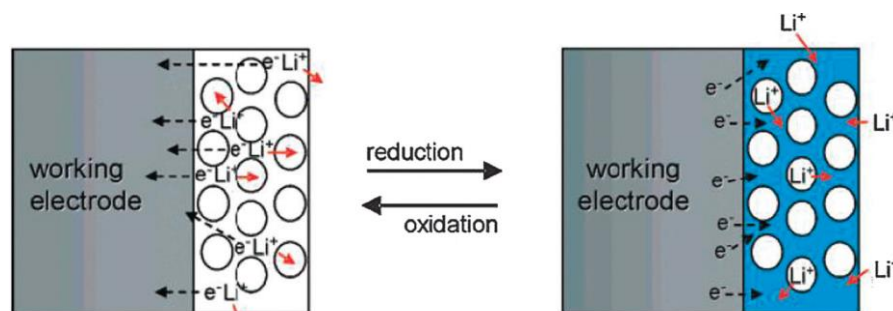
Fig. 1.11 Schematic illustration of electrochromism in mesoporous WO_3 films; the migratory direction of lithium and the associated coloration/bleaching of the inorganic matrix are also shown.[97]

Some mesoporous materials can be also synthesized for photochromic applications when combined with silver nanoparticles[98,99] or photoactive organic molecules[100,101]. For example, L. Bois *et al.* reported the synthesis of mesoporous TiO_2 template with embedded silver nanoparticles from ammonium silver salt by using a chemical reductive treatment.[102]

Although the applications of mesoporous metal oxides are numerous, magnetism and spintronics are areas in which the potential of these exiting materials has been rather overlooked. In this Thesis, the magnetic properties of mesoporous transition metal–doped SnO_2 powders and films are studied in view of their potential uses in magnetic storage and spintronic nanodevices.

1.6 State–of–the–art on mesoporous SnO₂ materials

Mesoporous transition metal oxide–based materials with different morphologies have attracted much interest due to their unique physico–chemical properties arising from their high porosity and specific surface area. Tin dioxide (SnO_2), an n–type semiconductor (band gap E_g=3.6 eV at 300 K) with tetragonal rutile structure (Fig. 1.12 (a)),[103,104] has been one of the most investigated materials due to its fascinating optical and electrical properties.[105,106] In particular, SnO_2 has been largely used in solid–state gas devices (Fig. 1.12 (c)–(d)) owing to its mechanical hardness, electrical resistivity, and chemical inertness (e.g. as CO detector).[107] However, one of the key issues limiting its wide gas–sensing applications is its low selectivity and durability. Thus, much effort has been devoted to the enhancement of its gas–sensing performance by suitably doping it with noble metals, semi–metals or halogens.[108,109,110]
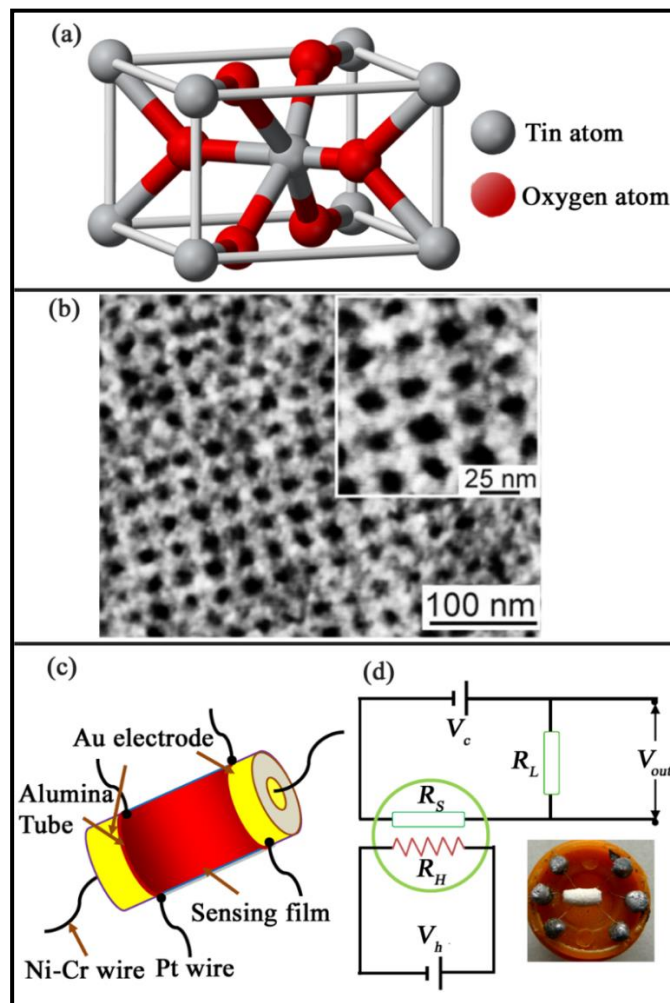
Fig. 1.12 (a) Schematic illustration of SnO_2 rutile (cassiterite) structure, (b) AFM image (inset: higher–magnification image) of a SnO_2 thin film,[111] (c) general scheme of a gas sensor, (d) common electric circuit in the gas sensing.[112]

Typically, ordered mesoporous SnO_2 particles have been obtained as a negative replica of SBA–15[113] and KIT–16[114] MS templates and chloride precursors (e.g. $SnCl_2 \cdot 2H_2O$). However, the synthesis of mesoporous SnO_2 from MCM–41 or cage–like SBA–16 silica templates has also been reported.[115,116] One of the difficulties is that the SnO_2 replica contains between 5 and 15% residual MS, which has been claimed to contribute, at least in part, to the high surface areas (100 m^2/g) reported in some works. For this reason, the synthesis of mesoporous SnO_2 powders by soft–templating has been also pursued. However, this approach also entails obvious difficulties, like pore structure collapse after calcination, yielding a non–porous powder. Recently, the direct synthesis of good quality mesoporous SnO_2 networks by soft–templating has been reported, showing thermal stability up to 500 °C.[117]

The literature related to the manufacture of mesoporous SnO_2 films is far scarcer than for powders. Regarding the fabrication of mesoporous SnO_2 by EISA, highly crystalline films with periodically ordered large pores were[111] obtained with a special KLE type amphiphilic polymer (poly(ω–hydroxypoly(ethylene–*co*–butylene)–*co*–poly(ethylene oxide))), which is however not yet commercially available. The preparation of crystalline mesoporous SnO_2 films with a larger pore size using commercially available Pluronic polymers (F–127 is the most used) has sometimes provided either only partially crystalline films,[118] or has required a post–synthesis treatment like the exposure of the films to a stream of water vapor at elevated temperature to promote the ordering of as–prepared disordered films.[119] Moreover, the choice of available precursors is rather restricted, mostly limited to $SnCl_4$ or $SnCl_2$ due to the high cost of tin alkoxides. In 2007 J. H. Pan *et al.* synthesized cubic and hexagonal mesoporous SnO_2 thin films, using $SnCl_4$ as the precursor and pluronic F–127 as structure directing agent. In this case, EISA was combined with spin–coating.[120] $SnCl_4$ was also utilized as the precursor in the synthesis of mesoporous cassiterite SnO_2 films in ammonium hydroxide environment in another work. The resulting films showed worm–like porosity with a wall to wall distance of ca. 18 nm and a surface area of 55±5 m^2/g.[121]

Nanostructured mesoporous SnO_2 materials (both powders and thin films) have been utilized in various applications, although gas–sensing is perhaps the main one. M. Dimitrov *et al.* used mesoporous SnO_2 powders in the catalytic total oxidation of ethyl acetate.[122] In the research of H. Oh *et al.*, mesoporous M–doped SnO_2 (M = Sb, In, F) bulk powders were fabricated as catalyst supports in electrolytic cells.[123] Recently, Yang *et al.* have proved the higher electrochemical performance of mesoporous SnO_2 powders in combination with graphene as anode material in lithium–ion batteries. [124] As aforementioned, mesoporous SnO_2 powders have been extensively studied for gas sensing applications. D. Wang *et al.* reported mesoporous SnO_2–based sensors for the detection of

chlorine gas.[125] The results showed that the fabricated sensors showed a very fast response toward diluted Cl_2 gas. Similarly, mesoporous SnO_2 spheres showed higher sensitivity to H_2 and enhanced response to CO gas compared with commercial (non–mesoporous) SnO_2 powders.[126]

Mesoporous SnO_2 films have also attracted a great deal of technological interest over the past two decades. For example, Y. Wang and co–workers recently prepared ordered mesoporous M–doped SnO_2 films (M = Sb, Nb, and Ta), with high electrical conductivity.[127] Also, in the study of J. T. Park *et al.*, multifunctional mesoporous SnO_2 films were obtained by sol–gel method. These films were further used as interfacial layer (combined with TiO_2 and F–doped SnO_2 substrates) to enhance light harvesting, improving electron transport and reducing interfacial/internal resistances in DSSCs.[128] Additionally, highly crystalline and ordered mesoporous Pd–doped SnO_2 thin films were successfully synthesized by S. Shao *et al.* Due to the long–range nanoporous periodicity, small particle size and excellent particle interconnectivity, samples showed enhanced acetone sensing performance. [129] Recently, H. Long *et al.* fabricated a low power microheater sensor platform for CO gas based on highly porous SnO_2 sensing film. This sensor exhibited low detection limit (2 ppm), fast response time (< 10 s) and short recovery time (< 30 s).[130] One important aspect when it comes to mesoporous transition metal oxide films, which also applies to SnO_2 case, is that the term 'films' is often used when mesoporous powders are post–deposited on a substrate. The concept of 'mesoporous film' used throughout this Thesis is different since the film is built in situ using a bottom–up approach, in our case, EISA combined with dip–coating.

1.7 Magnetism

1.7.1 Types of magnetic behaviours in nature

Based on modern magnetism theory, the magnetism of materials is originated from the existence of magnetic moment in the atoms associated either with the movement of electrons around the atomic nucleus (orbital moment) or electron rotation around their own axis (spin moment).[131] According to the different response to an applied external field, materials can be classified into five categories: diamagnetism, paramagnetism, ferrimagnetism, ferromagnetism and antiferromagnetism.[132]

- **Diamagnetism**

  As a quantum mechanical effect, diamagnetism occurs in all atoms. The origin of diamagnetism is the change of electron orbital motion in response to an applied magnetic

field. If an external field exists, diamagnetic materials will show a linear negative slope in the magnetization vs. field curve. Thus, diamagnetic materials are repelled by the applied field. Compared to paramagnetism or ferromagnetism, the phenomenon of diamagnetism is quite weak.[133] Consequently, in many materials, diamagnetism is always overshadowed by other stronger contributions (i.e., materials that are ferromagnetic or antiferromagnetic are also, at the same time, diamagnetic). Some elements are purely diamagnetic, like silicon, gold, silver or bismuth. Because diamagnetic materials do not present permanent magnetic moment when removing the applied external field, they do not exhibit hysteresis (contrary to ferromagnetic or ferrimagnetic materials, as will be described below).

- **Paramagnetism**

In paramagnetic materials, the magnetic moments are uncoupled to each other. When an external magnetic field is applied, just a small fraction of the magnetic moments are oriented along the field direction. Consequently, a linear relationship, with a weak positive slope, is established between the magnetization and the applied field. Nevertheless, in the normal situation, due to thermal agitation, the spin orientations of paramagnetic materials is at random (Fig. 1.13 (a)), thus resulting in the disappearance of magnetization in the absence of an external field. As diamagnetic materials, paramagnetic materials do not show hysteresis. Some examples are platinum, tin or sodium.

- **Ferromagnetism**

Ferromagnetism refers to the ability of some materials to partially retain their magnetic properties when the external magnetic field is removed. In other words, ferromagnetism is the property of some materials to be attracted by magnets or even act as permanent magnets. Ferromagnetism only occurs in materials whose atom shells (3d or 4f electronic bands) are only partially filled by electrons and have a net magnetic moment. In these materials, the spins of neighboring atoms are oriented parallel to each other since they are coupled via positive exchange interactions. In ferromagnetic materials, the magnetic moments tend to align parallel to each other (Fig. 1.13 (b)) within certain regions (domains). This effect originates a local spontaneous magnetization. When a large enough magnetic field is applied, the magnetization of the different domains aligns with the magnetic field. Ferromagnetic materials become paramagnetic above the so–called Curie temperature (T_C).

- **Antiferromagnetism**

In antiferromagnetic materials, as a result of negative exchange interactions, the magnetic moments existing in neighboring atoms orient antiparallel to each other. This phenomenon is schematically illustrated in Fig. 1.13 (c). Due to this antiparallel

alignment, even though the strength of each atomic moment can be high, the net moment decreases to zero after the external magnetic field is removed. As paramagnetic materials, antiferromagnetic materials show a linear relationship between the magnetization and applied magnetic field with a small positive slope. Antiferromagnetic materials become paramagnetic above the so–called Néel temperature (T_N).

- **Ferrimagnetism**

Like antiferromagnetic materials, the atoms of ferrimagnetic materials possess opposite magnetic moments (antiparallel alignment). The difference is that in ferrimagnetic materials, the two sublattices or antiparallel spins are unequal and, therefore, spontaneous magnetization exists (as shown in Fig. 1.13 (d)), leading to a non–zero net magnetic moment. From a phenomenological point of view, when an external field applied, ferrimagnetic materials exhibit a clear hysteresis loop, similar to ferromagnetic ones. Most ferrimagnetic materials are ceramics and can be used as good insulators in many high–frequency applications.[134]
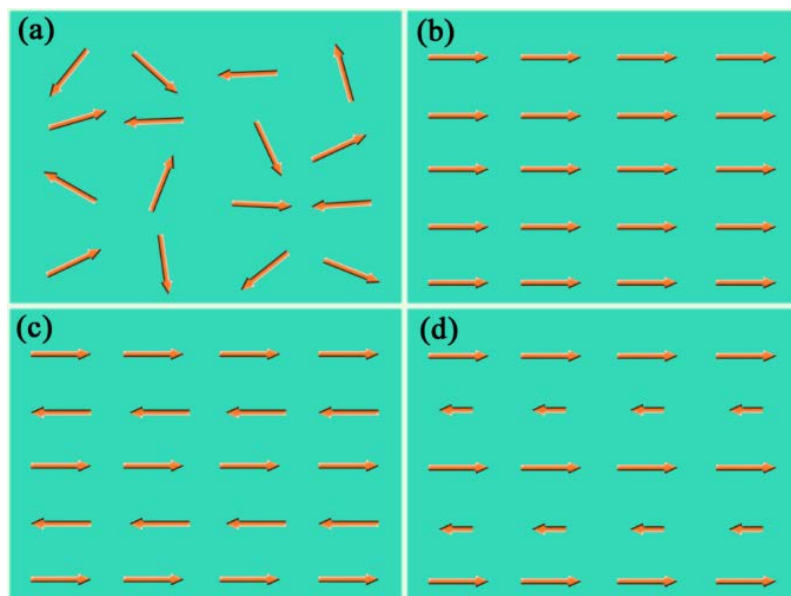
Fig. 1.13 Schematic drawing of the magnetic moments configuration: (a) paramagnetism, (b) ferromagnetism, (c) antiferromagnetism, (d) ferrimagnetism.

1.7.2 Hysteresis loops: basic parameters

Fig. 1.14 schematically illustrates the typical hysteresis loop (magnetization versus field) displayed by a ferromagnetic or ferrimagnetic material. As shown in this figure, the application of an external magnetic field causes the spins of the electrons progressively align with the field. When the strength of the field is sufficient, the magnetization levels off

and reaches a constant value, which is called saturation magnetization (M_s). When the magnitude of the applied field is reduced back to zero, the magnetization still retains a positive value, which is defined as remanent magnetization (M_r). The ratio of the remanent magnetization to saturation magnetization (M_r/M_s) is called squareness ratio and it varies from 0 to 1. The remanent magnetization can be removed by reversing the magnetic field strength to a value equal to the coercivity (H_c). When the reversed magnetic field is increased further, saturation is achieved in the reversed direction.

As the name implies, the hysteresis loop shows the "history dependent" nature of magnetization for a ferromagnetic material. The magnetic properties of nanostructured ferromagnetic materials are largely determined by the characteristics of their hysteresis loops. Ferromagnetic/ferrimagnetic materials can be roughly classified into two categories: soft and hard ferromagnetic/ferrimagnetic materials. Soft materials are characterized by narrow hysteresis loops: low values of H_C, typically lower than 10 Oe, and large values of M_s, usually higher than 100 emu/g. Some examples of soft ferromagnetic materials are Fe, Ni, permalloy or FeSi alloys. They are used in transformers cores, for example. Hard ferromagnetic/ferrimagnetic materials, also known as permanent magnets, show a broad hysteresis loop, with high values of H_C, typically larger than 350 Oe, and usually smaller values of M_s than soft magnetic materials. Some examples of hard ferromagnetic materials are Al–Ni–Co alloys, $SmCo_5$ or $Nd_2Fe_{14}B$.
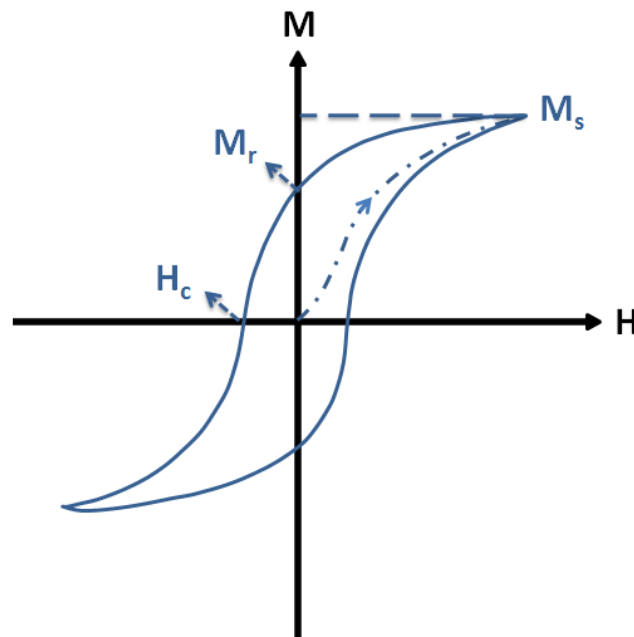
Fig. 1.14 Schematic illustration of a hysteresis loop in a ferromagnetic material. The field strength, H; magnetization, M; saturation magnetization, M_s; remanent magnetization, M_r; and magnetic coercivity, H_C; are indicated.

1.7.3 Magnetic properties of nanomaterials

In general, when the geometrical dimensions of materials decrease, they exhibit properties that are quite different compared with the bulk. For example, with the geometric confinement effect, the magnetic transition temperature, T_C (for a ferromagnetic or ferrimagnetic material) or T_N (for an antiferromagnetic material), is reduced from the bulk value, $T_C(\infty)$ or $T_N(\infty)$ as follows:[135]

$$\Delta T = \frac{T_C(\infty) - T_C(d)}{T_C(\infty)} = \left(\frac{\xi_o}{d}\right)^{\lambda}$$

[Eq. 1.9]

or

$$\Delta T = \frac{T_N(\infty) - T_N(d)}{T_N(\infty)} = \left(\frac{\xi_o}{d}\right)^{\lambda}$$

[Eq. 1.10]

where d is the sample size, ξ_0 is a constant for the exchange correlation length of the bulk phase at a certain temperature away from the ordering temperature and λ is the shift exponent.[136]

Besides the critical temperatures, there are other intrinsic properties of ferromagnetic/ferrimagnetic/antiferromagnetic materials that can be affected by the sample (or particle) size. "Magnetic anisotropy" in ferromagnets/ferrimagnets is the preference for the magnetization to lie along a particular direction in the material. Magnetic anisotropy can be either an intrinsic property of the material (e.g. magnetocrystalline anisotropy) or can be externally induced (e.g. shape anisotropy or stress anisotropy). Magnetocrystalline anisotropy is closely related to the crystalline structure of the material and is originated from the interaction between the spin part of the magnetic moment and the electronic orbital shape and orientation (spin–orbit coupling). Shape anisotropy is related to the magnetostatic energy and, in thin films, it causes the magnetization to preferably lie within the film plane.

If a magnetic field is applied to a single crystal ferromagnetic material, the field strength needed to saturate it is found to be smaller when applied along certain directions, which are called easy–axis directions. On the contrary, larger fields are required to saturate the material in other directions. These are called hard–axis directions. In addition, in absence of an external field, the magnetization prefers to lie along the easy directions. When a magnetic field is applied to a ferromagnetic material, a certain work is required in order to move the spins away from the easy axis direction. Therefore, a certain energy, called anisotropy energy, is stored in the magnet when the magnetic field is applied in a direction different from the easy axis. When the anisotropy energy becomes larger, the coercivity increases since more field is needed to induce magnetization reversal.

For non–interacting ferromagnetic/ferrimagnetic particles, a maximum is obtained when the coercivity, H_C, is plotted as a function of the crystallite size (or sample size), <d> (Fig. 1.15). For large values of <d>, when the direction of H is reversed, the magnetization reverses due to the formation and motion of domain walls (multi–domain state). However, if the crystallite size is reduced to $<d>_{Cr}$ (critical diameter), the formation of domain walls becomes energetically unfavourable, and the particles remain in a single–domain state. In such a case, the magnetization reverses by means of coherent rotation of spins, causing a higher value of H_C. If <d> is further reduced to below $<d>_{Cr}$, thermal fluctuations cause some magnetic disorder in the material and H_C is progressively reduced. Finally, if <d> is low enough the system becomes superparamagnetic and no hysteresis is observed. This happens when the thermal energy, $k_B T$ (k_B being the Boltzmann constant) at a given temperature becomes of the order of the effective magnetic energy, $K \cdot V$, where K is the magnetic anisotropy and V is the volume of the ferromagnetic/ferrimagnetic particle. Superparamagnetism leads to instability of the stored information in magnetic recording media. However, due to their zero net magnetization in absence of external magnetic field, superparamagnetic particles have the potential to be used in drug delivery, since they do not interact with each other once the field is removed, hence avoiding thrombosis and other medical problems.
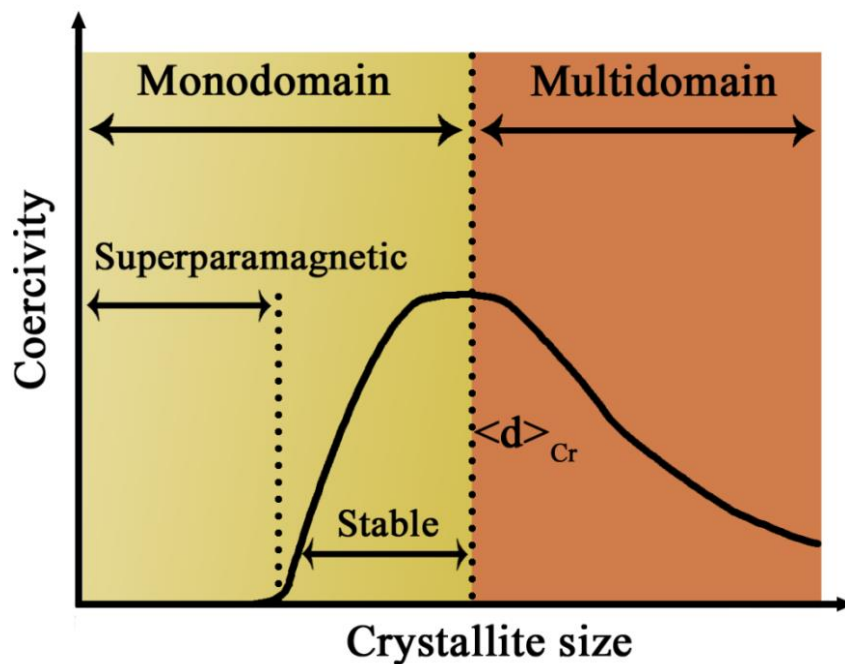
Fig. 1.15 Dependence of the coercivity on the crystallite size, <d>, for non–interacting ferromagnetic/ferrimagnetic particles.

1.8 State–of–the–art on diluted magnetic semiconductors (DMSs)

In recent years, a huge increase of the data processing speed and the integration density, together with a decrease of electric power consumption have been achieved by adding the spin degree of freedom to the charge of electrons (i.e., moving from electronics to spintronics).[137] The first generation of spintronics devices was fabricated based on passive magneto–resistive sensors taking advantage of the discovery of the giant magnetoresistance (GMR) effect[138,139] and the subsequent development of spin valves and tunneling junctions (Fig. 1.16).[140] Nowadays, the next generation of spintronics devices is at the edge of technological innovation.[141] Magnetic semiconductors could largely contribute to this new revolution since they can benefit from the well–established technologies for semiconductor processing in microelectronics with the added value given by the magnetic properties. Also, magnetic semiconductors would be more easy to integrate with conventional (i.e., non–magnetic) semiconductors than magnetic metallic alloys due to their better match in electric resistivity (in applications like spin injection, spin polarization, etc.). Hence, DMSs have recently attracted significant attention of scientists and engineers due to their potential application in the field of spin–based devices.
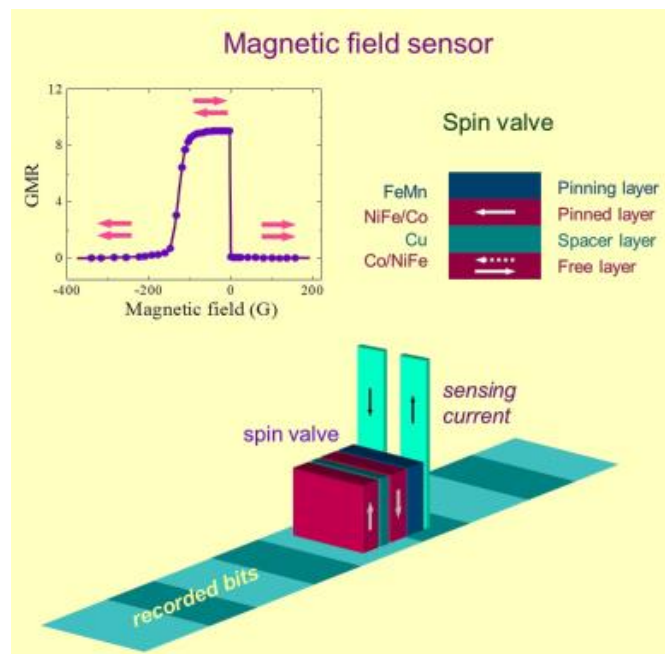
Fig. 1.16 Schematic representation of a G_{MR} read head sensor in a hard disk using a spin valve.[142]

Several examples of ferromagnetic semiconductor materials are: (i) manganese–doped indium arsenide and gallium arsenide (GaMnAs), with Curie temperature around 50–100 K and 100–200 K, respectively, (ii) manganese–doped indium antimony, which becomes ferromagnetic even at room temperature, (iii) oxide–diluted magnetic semiconductors (like transition metal doped ZnO, TiO_2, In_2O_3 or SnO_2), also ferromagnetic at room temperature.

40

1.8.1 Mn–doped P–type magnetic semiconductors

According to the model proposed by Zener, ferromagnetism in Mn–doped semiconductors is driven by the exchange interaction between band carriers and localized spins. [143] Furthermore, Ruderman–Kittel–Kasuya–Yosida (RKKY) interactions can also account in part for the observed ferromagnetic–like properties (Fig. 1.17 (a)). [144] In Mn–doped semiconductors, instead of free electrons, ferromagnetism is associated with the presence of deficient holes. [145] Y. Fukuma and co–workers observed homogeneous ferromagnetism with maximum Tc reaching 190 K on the $Ge_{0.92}Mn_{0.08}Te$ epilayers that grown on BaF_2 substrates. [146] At the same time L. Chen and co–workers also fabricated $Ga_{1-x}Mn_xAs$ films by molecular–beam epitaxy with different amounts of Mn. In their research, the maximum Tc was improved to 191 K by post–growth annealing on the sample $Ga_{0.8}Mn_{0.2}As$. [147] Recently, Bo Gu $et\ al$. used the density function theory together with quantum Monte Carlo simulations to demonstrate that DMSs can be achieved with a narrow band gap host semiconductors. In their prediction, the Curie temperature Tc of Mn–doped $BaZn_2Sb_2$ could be even higher than that of Mn–doped $BaZn_2As_2$, whose Tc reached 230 K. [148,149]
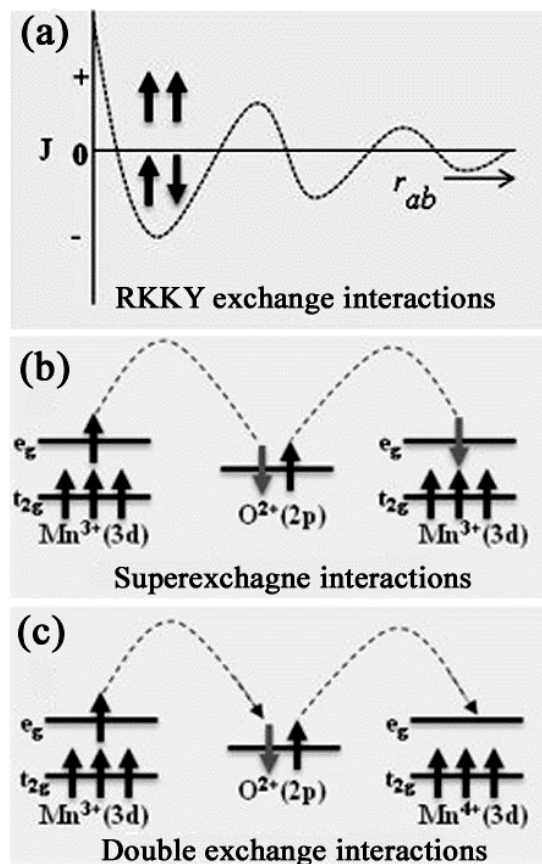
Fig. 1.17 Schematic illustration of different models of exchange interactions: (a) RKKY exchange parameter J as a function of interatomic distance of magnetic atoms, (b) example of superexchange interactions in MnO system, (c) double exchange interactions in MnO system. Adapted from ref. [150]

1.8.2 Transition metal–doped oxide semiconductors

Oxide diluted magnetic semiconductors are generally transparent materials with a wide–band gap, such as TiO_2–, In_2O_3– and ZnO–based magnetic semiconductors.[151,152,153] Over the past decade, different approaches, such as pulsed laser deposition, reactive sputtering, molecular beam epitaxy or ion implantation have been used to incorporate transition metals into oxide semiconductors to achieve ferromagnetism. According to the existing reports so far, especially after the prediction of room–temperature ferromagnetic response in Mn–doped ZnO (as shown in Fig. 1.18),[154] several wide–bang gap oxide semiconductors doped with transition metal cations are viewed as promising candidates with high T_C.
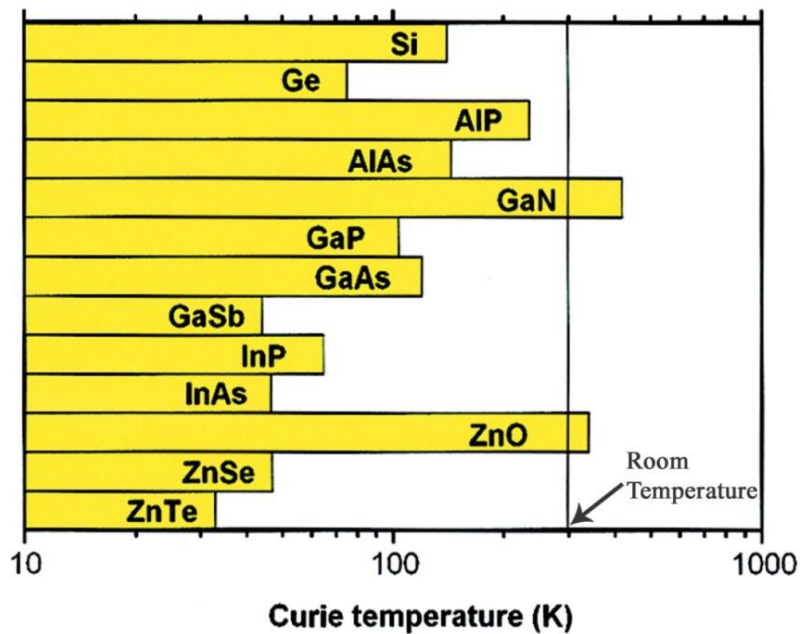
Fig. 1.18 Computed values of the Curie temperature (T_C) for various p–type semiconductors containing 5% of Mn and 3.5×10^{20} holes per cm^3.[154]

Ferromagnetic properties with high T_C are mostly observed in thin films and nanocrystals, while for the well–crystallized bulk materials, it is hard to get ferromagnetism at room temperature.[155, 156] For example, S. B. Ogale and co–workers reported that high–temperature ferromagnetism ($T_C = 650$ K) was found in Co–doped $SnO_{2-\delta}$ thin films.[157] The films were grown on single crystal sapphire by pulsed laser deposition and the magnetic moment was up to 7.5 ± 0.5 μ_B/Co. By using the same synthesis technique, H. Saadaoui et al. prepared Co–doped $TiO_{2-\delta}$ anatase films with homogeneous microstructure.[158] Moreover, they investigated the influence of deposition rate and oxygen partial pressure on the magnetism. F. Pan and co–workers prepared Co–doped ZnO films on Al_2O_3 (001) substrate via direct current reactive magnetron co–sputtering.[153] The transition from diluted magnetic insulators (DMIs) to DMSs was realized by decreasing oxygen partial pressure.

42

They also demonstrated that the structure defects seem to be necessary for the intrinsic ferromagnetic ordering. In the research of B. Prajapati *et al*., Fe–doped TiO_2 nanoparticles were synthesized via a sol–gel technique.[159] With the appropriate doping amount, the nanoparticles showed a weak ferromagnetic at room temperature.

In order to explain the origin of ferromagnetism, some theoretical models have been proposed. According to some pioneering simulation works, if the states derived from the transition metal d levels are partly occupied, ferromagnetism can be assigned to the ferromagnetic superexchange or double exchange (Fig. 1.17 (b) and (c)).[160,161,162] In another model, it is supposed that the ferromagnetic coupling between diluted transition metal spins are mediated by the electrons that reside in the conduction band or form magnetic polarons (i.e., bound magnetic quasiparticles arising from the interaction between electrons and atomic defects in semiconductors).[163,164] In addition, many researchers believe that there is a strong dependence between ferromagnetism and the distribution of oxygen vacancies.[165,166,167] Noteworthy, in a so–called d^0 model, ferromagnetism is related to spins of electrons that reside on defects and are coupled by an exchange interaction. Consequently, the presence of magnetic impurities is even either unnecessary or serves merely to change the Fermi level to the relevant defect states, and spontaneous ferromagnetism can occur in percolating defect–rich regions.[145,168]

Nowadays, although challenges in developing new materials with improved properties remains great and the origin of the intrinsic high–temperature ferromagnetism in the DMSs remains controversial, many efforts are under way to explore new materials for spintronics applications. Nonetheless, all former contradictions and speculations from the literature need to be addressed experimentally. So far, most reported oxide diluted magnetic semiconductors were prepared in fully–dense thin films,[169] nanowires[170,171] or coarse polycrystalline powders.[172] There are only few reports about DMSs with mesoporous structure,[173,174,175] as those mesoporous materials are usually synthesized for chemical or physicochemical purposes/applications. According to the existing reports, the magnetic behaviour of mesoporous oxide DMSs can be tuned by adjusting the transition metal doping level and the amount of oxygen vacancies. Additionally, mesoporous oxide DMSs could exhibit extra unique properties, as compared to their bulk counterparts, such as quantum–confinement effects, surface spin–glass or uncompensated spins, and combined optical and magnetic surface effects. This means that mesoporous frameworks may have a positive impact on the development of spintronic nanodevices. From a practical point of view, it will be very appealing if new progress in the field can lead to new pathways for spintronics study by combining mesoporous semiconductors fabrication and doping technology.

1.9 Objectives

This Thesis covers the fabrication of mesoporous transition metal (TM)–doped SnO_2 systems, both in powder and thin film configuration, their structural characterization and the investigation of their magnetic properties. In particular, Cu and Ni have been introduced as TM dopants in a mesostructured SnO_2 matrix. Special emphasis has been put to the valence state and distribution of these dopant species in order to understand the observed ferromagnetic response of the materials at either room or low temperature. This Thesis attempts to introduce, to a certain extent, a new direction in the synthesis of oxide–diluted magnetic semiconductors which could contribute to the next generation of spintronics devices.

The goals of this Thesis can be summarized as follows:

1) *Synthesis and characterization of ordered Ni–doped mesoporous SnO_2 powders by the nanocasting method.* The main purpose of this research is to produce ordered mesoporous SnO_2 powders from KIT–6 silica template and to solubilize different amounts of Ni in the SnO_2 lattice. Instead of wet impregnation, solid state grinding is used in the synthesis process. A second goal is to characterize the distribution of Ni within the SnO_2 skeleton. Moreover, the relationship between magnetic properties and the amount of Ni is to be established.

2) *Preparation of Ni–doped mesoporous SnO_2 thin films by the combination of evaporation–induced self–assembly (EISA) and dip–coating techniques*. This part of the work is devoted to semiconductor films with mesoporous structure. The main purpose is to achieve SnO_2 thin films with 3–dimensional connectivity, while ensuring successful doping with Ni species. The influence of the dopant valence state on the magnetic properties will be investigated as well.

3) *Synthesis and characterization of ordered Cu–doped mesoporous SnO_2 powders by the nanocasting method.* The first objective of this research is to illustrate the influence of another dopant (in this case, Cu) on the magnetic properties of SnO_2 mesoporous powders also produced by nanocasting. Changes in the magnetic behavior of the materials with both the temperature and the amount of Cu will be investigated. Advanced X–ray magnetic circular dichroism analyses will be performed to unravel the origin of ferromagnetism (if so) in the materials.

References

[1] J. Rouquerolt, D. Avnir, C. W. Fairbridge, D. H. Everett, J. H. Haynes, N. Pernicone, J. D. F. Ramsay, K. S. W. Sing and K. K. Unger, Recommendations for the characterization of porous solids, *Pure Appl. Chem.*, 1994, **66**, 1739–1758.

[2] M. E. Davis, Zeolites and molecular sieves: not just ordinary catalysts, *Ind. Eng. Chem. Res.*, 1991, **30**, 1675–1683.

[3] J. D. Sherman, Synthetic zeolites and other microporous oxide molecular sieves, *Proc. Natl. Acad. Sci. U. S. A.*, 1999, **96**, 3471–3478.

[4] L. F. Giraldo, B. L. López, L. Pérez, S. Urrego, L. Sierra and M. Mesa, Mesoporous silica applications, *Macromol. Symp.*, 2007, **258**, 129–141.

[5] B. Sakintuna and Y. Yürüm, Templated porous carbons: A review article, *Ind. Eng. Chem. Res.*, 2005, **44**, 2893–2902.

[6] M. Tiemann, Repeated templating, *Chem. Mater.*, 2008, **20**, 961–971.

[7] S. L. Suib, A review of recent developments of mesoporous materials, *Chem. Rec.*, 2017, 1–16.

[8] Y. Wan and D. Zhao, On the controllable soft–templating approach to mesoporous silicates, *Chem. Rev.*, 2007, **107**, 2821–2860.

[9] J.–K. Sun, M. Antonietti and J. Yuan, Nanoporous ionic organic networks: from synthesis to materials applications, *Chem. Soc. Rev.*, 2016, **45**, 6627–6656.

[10] Biolin Scientific, http://www.biolinscientific.com/attension/applications/?card=AA8

[11] R. J. Farn, *Chemistry and Technology of Surfactants*, Blackwell Publishing Ltd, 2007.

[12] Wiki Home, https://ibhumanbiochemistry.wikispaces.com/C.4.4

[13] B. Tan and S. E. Rankin, Study of the Effects of Progressive Changes in Alkoxysilane Structure on Sol – Gel Reactivity, 2006, 22353–22364.

[14] C. T. Kresge, M. E. Leonowicz, W. J. Roth, J. C. Vartuli and J. S. Beck, Ordered mesoporous molecular sieves synthesized by a liquid–crystal template mechanism, *Nature*, 1992, **359**, 710–712.

[15] J. S. Beck, J. C. Vartuli, W. J. Roth, M. E. Leonowicz, C. T. Kresge, K. D. Schmitt, C. T.–W. Chu, D. H. Olson, E. W. Sheppard, S. B. McCullen, J. B. Higgins and J. L. Schlenkert, A new family of mesoporous molecular sieves prepared with liquid crystal templates, *J. Am. Chem. Soc.*, 1992, **114**, 10834–10843.

[16] N. Pal and A. Bhaumik, Soft templating strategies for the synthesis of mesoporous materials: inorganic, organic–inorganic hybrid and purely organic solids, *Adv. Colloid Interface Sci.*, 2013, **189**–**190**, 21–41.

[17] Q. Huo, D. I. Margolese, U. Ciesla, P. Feng, T. E. Gier, P. Sieger, R. Leon, P. M. Petroff, F. Schüth and G. D. Stucky, Generalized synthesis of periodic surfactant/inorganic composite materials, *Nature*, 1994, **368**, 317–321.

[18] W. Li and D. Zhao, An overview of the synthesis of ordered mesoporous materials, *Chem. Commun.*, 2013, **49**, 943–946.

[19] J. R. Matos, L. P. Mercuri, M. Kruk and M. Jaroniec, Toward the synthesis of extra–large–pore MCM–41 analogues *Chem. Mater.*, 2001, **13**, 1726–1731.

[20] P. T. Tanev, M. Chibwe and T. J. Pinnavaia, Titanium–containing mesoporous molecular sieves for catalytic oxidation of aromatic compounds, *Nature*, 1994, **368**, 321–323.

[21] O. A. Anunziata, M. L. Martínez and A. R. Beltramone, Hydroxyapatite/MCM–41 and SBA–15 nano–composites: Preparation, characterization and applications, *Materials*, 2009, **2**, 1508–1519.

[22] X. Liu, B. Tian, C. Yu, F. Gao, S. Xie, B. Tu, R. Che, L. M. Peng and D. Zhao, Room–temperature synthesis in acidic media of large–pore three–dimensional bicontinuous mesoporous silica with *Ia3d* symmetry, *Angew. Chemie – Int. Ed.*, 2002, **41**, 3876–3878.

[23] A.–H. Lu, D. Zhao and Y. Wang, *Nanocasting: A Versatile Strategy for Creating Nanostructured Porous Materials*, The Royal Society of Chemistry, 2009.

[24] D. Zhao, Y. Wan and W. Zhou, *Ordered Mesoporous Materials*, Wiley–VCH Verlag GmbH & Co. KGaA, Weinheim, Germany, 2013.

[25] S. R. Chowdhury, R. Schmuhl, K. Keizer, J. E. Ten Elshof and D. H. A. Blank, Pore size and surface chemistry effects on the transport of hydrophobic and hydrophilic solvents through mesoporous γ–alumina and silica MCM–48, *J. Memb. Sci.*, 2003, **225**, 177–186.

[26] K. Schumacher, P. I. Ravikovitch, A. Du Chesne, A. V. Neimark, K. K. Unger, A. Du Chesne, A. V. Neimark and K. K. Unger, Characterization of MCM–48 materials, *Langmuir*, 2000, **16**, 4648–4654.

[27] F. Kleitz, S. H. Choi and R. Ryoo, Cubic Ia3d large mesoporous silica: synthesis and replication to platinum nanowires, carbon nanorods and carbon nanotubes, *Chem. Commun.*, 2003, 2136–2137.

[28] C. Jo, K. Kim and R. Ryoo, Syntheses of high quality KIT–6 and SBA–15 mesoporous silicas using low–cost water glass, through rapid quenching of silicate structure in acidic solution, *Microporous Mesoporous Mater.*, 2009, **124**, 45–51.

[29] A. Vinu, P. Srinivasu, D. P. Sawant, T. Mori, K. Ariga, J. S. Chang, S. H. Jhung, V. V. Balasubramanian and Y. K. Hwang, Three–dimensional cage type mesoporous CN–based hybrid material with very high surface area and pore volume, *Chem. Mater.*, 2007, **19**, 4367–4372.

[30] J. Fan, C. Yu, F. Gao, J. Lei, B. Tian, L. Wang, Q. Luo, B. Tu, W. Zhou and D. Zhao, Cubic mesoporous silica with large controllable entrance sizes and advanced adsorption properties, *Angew. Chemie – Int. Ed.*, 2003, **42**, 3146–3150.

[31] J. Fan, C. Yu, J. Lei, B. Tu, Q. Zhang, T. Li and W. Zhou, Low–temperature strategy to synthesize highly ordered mesoporous silicas with very large pores, *J. Am. Chem. Soc.*, 2005, **127**, 10794–10795.

[32] P. Du, P. Zheng, S. Song, X. Wang, M. Zhang and K. Chi, Synthesis of a novel micro/mesoporous composite material Beta–FDU–12 and its hydro–upgrading performance for FCC gasoline, *RSC Adv.*, 2015, **6**, 1018–1026.

[33] Monografias, http://www.monografias.com/trabajos–pdf5/tecnologia–industrial/tecnologia–industrial.shtml

[34] C. G. Goeltner and M. C. Weissenberger, Mesoporous organic polymers obtained by "twostep nanocasting", *Acta Polym.*, 1998, **49**, 704–709.

[35] K. Jiao, B. Zhang, B. Yue, Y. Ren, S. Liu, S. Yan, C. Dickinson, W. Zhou and H. He, Growth of porous single–crystal Cr2O3 in a 3–D mesopore system, *Chem. Commun.*, 2005, 5618.

[36] P. Mohanty, B. Kokoszka, C. Liu, M. Weinberger, M. Mandal, V. Stagno, Y. Fei and K. Landskron, Large–pore periodic mesoporous silicas with crystalline channel walls and exceptional hydrothermal stability synthesized by a general high–pressure nanocasting route, *Microporous Mesoporous Mater.*, 2012, **152**, 214–218.

[37] Z. A. Alothman, A review: fundamental aspects of silicate mesoporous materials, *Materials*, 2012, **5**, 2874–2902.

[38] Yu Ren, Zhen Ma and Peter G. Bruce, Ordered mesoporous metal oxides: synthesis and applications, *Chem. Soc. Rev.*, 2012, **41**, 4909–4927.

[39] R. Zhang and H. Olin, Porous gold films—a short review on recent progress, *Materials*, 2014, **7**, 3834–3854.

[40] P. Innocenzi and L. Malfatti, Mesoporous thin films: properties and applications, *Chem. Soc. Rev.*, 2013, **42**, 4198–216.

[41] F. Giordano, A. Abate, J. Pablo, C. Baena, M. Saliba, T. Matsui, S. H. Im, S. M. Zakeeruddin, M. K. Nazeeruddin, A. Hagfeldt and M. Graetzel, Enhanced electronic properties in mesoporous TiO_2 via lithium doping for high–efficiency perovskite solar cells, *Nat. Commun.*, 2016, **7**, 10379.

[42] J. C. Yu, X. Wang and X. Fu, Pore–wall chemistry and photocatalytic activity of mesoporous titania molecular sieve films, *Chem. Mater.*, 2004, **16**, 1523–1530.

[43] A. E. Danks, S. R. Hall and Z. Schnepp, The evolution of 'sol–gel' chemistry as a technique for materials synthesis, *Mater. Horizons*, 2016, **3**, 91–112.

[44] A. Carretero–Genevrier, G. L. Drisko, D. Grosso, C. Boissiere and C. Sanchez, Mesoscopically structured nanocrystalline metal oxide thin films, *Nanoscale*, 2014, **6**, 14025–14043.

[45] T. Ohya, M. Ito, K. Yamada, T. Ban, Y. Ohya and Y. Takahashi, Aqueous titanate sols from Ti alkoxide–α–hydroxycarboxylic acid system and preparation of titania films from the sols, *J. Sol–Gel Sci. Technol.*, 2004, **30**, 71–81.

[46] E. Scolan and C. Sanchez, Synthesis and characterization of surface–protected nanocrystalline titania particles, *Chem. Mater.*, 1998, **10**, 3217–3223.

[47] D. Brandhuber, V. Torma, C. Raab, H. Peterlik, A. Kulak and N. Hüsing, Glycol–modified silanes in the synthesis of mesoscopically organized silica monoliths with hierarchical porosity, *Chem. Mater.*, 2005, **17**, 4262–4271.

[48] C. J. Brinker, Y. Lu, A. Sellinger and H. Fan, Evaporation–induced self–assembly: nanostructures made easy, *Adv. Mater.*, 1999, **11**, 579–585.

[49] L. Nicole, C. Boissière, D. Grosso, A. Quach and C. Sanchez, Mesostructured hybrid organic–inorganic thin films, *J. Mater. Chem.*, 2005, **15**, 3598–3627.

[50] J. P. Hill, W. Jin, A. Kosaka, T. Fukushima, H. Ichihara, T. Shimomura, K. Ito, T. Hashizume, N. Ishii and T. Aida, Hexa–peri–hexabenzocoronene graphitic nanotube, *Science*, 2004, **304**, 1481–1483.

[51] Y. Yamamoto, T. Fukushima, Y. Suna, N. Ishii, A. Saeki, S. Seki, S. Tagawa, M. Taniguchi, T. Kawai and T. Aida, Photoconductive coaxial nanotubes of molecularly connected electron donor and acceptor layers, *Science*, 2006, **314**, 1761–1764.

[52] L. Chen, B. Yao, Y. Cao and K. Fan, Synthesis of well–ordered mesoporous titania with tunable phase content and high photoactivity, *J. Phys. Chem. C*, 2007, **111**, 11849–11853.

[53] M. C. Orilall and U. Wiesner, Block copolymer based composition and morphology control in nanostructured hybrid materials for energy conversion and storage: solar cells, batteries, and fuel cells, *Chem. Soc. Rev.*, 2011, **40**, 520–535.

[54] L. Mahoney and R. T. Koodali, Versatility of evaporation–induced self–assembly (EISA) method for preparation of mesoporous TiO_2 for energy and environmental applications, *Materials (Basel)*, 2014, **7**, 2697–2746.

[55] I. W. Fu, C. B. Markegard and H. D. Nguyen, Solvent effects on kinetic mechanisms of self–assembly by peptide amphiphiles via molecular dynamics simulations, *Langmuir*, 2015, **31**, 315–324.

[56] E. L. Crepaldi, G. Soler–Illia, D. Grosso, F. Cagnol, F. Ribot and C. Sanchez, Controlled formation of highly organized mesoporous titania thin films: From mesostructured hybrids to mesoporous nanoantase TiO_2, *J. Am. Chem. Soc.*, 2003, **125**, 9770.

[57] J.–Y. Kim, S. H. Kang, H. S. Kim and Y.–E. Sung, Preparation of highly ordered mesoporous Al_2O_3/TiO_2 and its application in dye–sensitized solar cells, *Langmuir*, 2010, **26**, 2864–2870.

[58] T. Brezesinski, D. F. Rohlfing, S. Sallard, M. Antonietti and B. M. Smarsly, Highly crystalline WO_3 thin films with ordered3D mesoporosity and improved electrochromic performance, *Small*, 2006, **2**, 1203–1211.

[59] K. Lazarova, B. Georgieva, M. Spasova and T. Babeva, Preparation and characterization of mesoporous Nb_2O_5 films for sensing applications, *J. Phys. Conf. Ser.*, 2014, **558**, 12042.

[60] G. J. A. A. Soler–Illia, P. C. Angelomé, M. C. Fuertes, A. Calvo, A. Wolosiuk, A. Zelcer, M. G. Bellino and E. D. Martínez, Mesoporous hybrid and nanocomposite thin films. A sol–gel toolbox to create nanoconfined systems with localized chemical properties, *J. Sol–Gel Sci. Technol.*, 2011, **57**, 299–312.

[61] F. Cagnol, D. Grosso, G. J. de A. A. Soler–Illia, E. L. Crepaldi, F. Babonneau, H. Amenitsch and C. Sanchez, Humidity–controlled mesostructuration in CTAB–templated silica thin film processing. The existence of a modulable steady state, *J. Mater. Chem.*, 2003, **13**, 61–66.

[62] C. H. Lee, Y. Lu and A. Q. Shen, Evaporation induced self assembly and rheology change during sol–gel coating, *Phys. Fluids*, 2006, **18**, 052105.

[63] C. Henrist, J. Dewalque, F. Mathis and R. Cloots, Control of the porosity of anatase thin films prepared by EISA: Influence of thickness and heat treatment, *Microporous Mesoporous Mater.*, 2009, **117**, 292–296.

[64] B. J. Melde, B. J. Johnson and P. T. Charles, Mesoporous silicate materials in sensing, *Sensors*, 2008, **8**, 5202–5228.

[65] Y. Xia, W. Huang, J. Zheng, Z. Niu and Z. Li, Nonenzymatic amperometric response of glucose on a nanoporous gold film electrode fabricated by a rapid and simple electrochemical method, *Biosens. Bioelectron.*, 2011, **26**, 3555–3561.

[66] L. Kashefi–Kheyrabadi and M. A. Mehrgardi, Aptamer–based electrochemical biosensor for detection of adenosine triphosphate using a nanoporous gold platform, *Bioelectrochemistry*, 2013, **94**, 47–52.

[67] C. Renault, V. Balland, E. Martinez–Ferrero, L. Nicole, C. Sanchez and B. Limoges, Highly ordered transparent mesoporous TiO_2 thin films: an attractive matrix for efficient immobilization and spectroelectrochemical characterization of cytochrome c, *Chem. Commun.*, 2009, 7494–7496.

[68] K. A. Kilian, T. Böcking and J. J. Gooding, The importance of surface chemistry in mesoporous materials: lessons from porous silicon biosensors, *Chem. Commun.*, 2009, 630–640.

[69] J. Du, J. Cipot–Wechsler, J. M. Lobez, H. P. Loock and C. M. Crudden, Periodic mesoporous organosilica films: Key components of fiber–optic–based heavy–metal sensors, *Small*, 2010, **6**, 1168–1172.

[70] H. J. Lee, K. K. Park, M. Kupnik, N. A. Melosh and B. T. Khuri–Yakub, Mesoporous thin–film on highly–sensitive resonant chemical sensor for relative humidity and CO_2 detection, *Anal. Chem.*, 2012, **84**, 3063–3066.

[71] A. Bearzotti, J. M. Bertolo, P. Innocenzi, P. Falcaro and E. Traversa, Humidity sensors based on mesoporous silica thin films synthesised by block copolymers, *J. Eur. Ceram. Soc.*, 2004, **24**, 1969–1972.

[72] G. Wirnsberger, B. J. Scott and G. D. Stucky, pH Sensing with mesoporous thin films. *Chem. Commun.*, 2001, 119–120.

[73] B. J. Melde and B. J. Johnson, Mesoporous materials in sensing: Morphology and functionality at the meso–interface, *Anal. Bioanal. Chem.*, 2010, **398**, 1565–1573.

[74] Z. Xiong, J. Ma, W. J. Ng, T. D. Waite and X. S. Zhao, Silver–modified mesoporous TiO_2 photocatalyst for water purification, *Water Res.*, 2011, **45**, 2095–2103.

[75] E. Allain, S. Besson, C. Durand, M. Moreau, T. Gacoin and J. P. Boilot, Transparent mesoporous nanocomposite films for self–cleaning applications, *Adv. Funct. Mater.*, 2007, **17**, 549–554.

[76] J. K. Kim, J. H. Moon, T.–W. Lee and J. H. Park, Inverse opal tungsten trioxide films with mesoporous skeletons: synthesis and photoelectrochemical responses, *Chem. Commun.*, 2012, **48**, 11939–11941.

[77] Y. Sakatani, D. Grosso, L. Nicole, C. Boissière, G. J. de A. A. Soler–Illia and C. Sanchez, Optimised photocatalytic activity of grid–like mesoporous TiO_2 films: effect of crystallinity, pore size distribution, and pore accessibility, *J. Mater. Chem.*, 2006, **16**, 77–82.

[78] A. A. Ismail and D. W. Bahnemann, Mesoporous titania photocatalysts: preparation, characterization and reaction mechanisms, *J. Mater. Chem.*, 2011, **21**, 11686.

[79] E. Martínez–Ferrero, Y. Sakatani, C. Boissière, D. Grosso, A. Fuertes, J. Fraxedas and C. Sanchez, Nanostructured titanium oxynitride porous thin films as efficient visible–active photocatalysts, *Adv. Funct. Mater.*, 2007, **17**, 3348–3354.

[80] N. Tasić, Z. Stanojević, Marinković, Z. Branković, U. Lačnjevac, V. Ribić, M. Žunić, T. Novaković, M. Podlogar and G. Branković, Mesoporous films prepared from synthesized TiO_2 nanoparticles and their application in dye–sensitized solar cells (DSSCs)**,** *Electrochim. Acta*, 2016, **210**, 606–614.

[81] Y. Li, J. Zhu, Y. Huang, F. Liu, M. Lv, S. H. Chen, L. H. Hu, J. W. Tang, J. X. Yao and S. Y. Dai, Mesoporous SnO_2 nanoparticle films as electron–transporting material in perovskite solar cells, *RSC Adv.*, 2015, **5**, 28424–28429.

[82] N. Linares, A. M. Silvestre–Albero, E. Serrano, J. Silvestre–Albero and J. García–Martínez, Mesoporous materials for clean energy technologies, *Chem. Soc. Rev.*, 2014, **43**, 7681–7717.

[83] A. Kojima, K. Teshima, Y. Shirai and T. Miyasaka, Organometal halide perovskites as visible–light sensitizers for photovoltaic cells, *J. Am. Chem. Soc.*, 2009, **131**, 6050–6051.

[84] W. S. Yang, J. H. Noh, N. J. Jeon, Y. C. Kim, S. Ryu, J. Seo and S. Il Seok, High–performance photovoltaic perovskite layers fabricated through intramolecular exchange, *Science,* 2015, **348**, 1234–1237.

[85] T. Maruo, S. Tanaka, H. W. Hillhouse, N. Nishiyama, Y. Egashira and K. Ueyama, Disordered mesoporous silica low–k thin films prepared by vapor deposition into a triblock copolymer template film, *Thin Solid Films*, 2008, **516**, 4771–4776.

[86] C. M. Yang, A. T. Cho, F. M. Pan, T. G. Tsai and K. J. Chao, Spin–on mesoporous silica films with ultralow dielectric constants, ordered pore structures, and hydrophobic surfaces, *Adv. Mater.*, 2001, **13**, 1099–1102.

[87] S. Tanaka, J. Kaihara, N. Nishiyama, Y. Oku, Y. Egashira and K. Ueyama, Incorporation of organic groups within the channel wall of spin–on mesostructured silica films by a vapor infiltration technique, *Langmuir*, 2004, **20**, 3780–3784.

[88] W. Volksen, R. D. Miller and G. Dubois, Low dielectric constant materials, *Chem. Rev.*, 2010, **110**, 56–110.

[89] G. A. Niklasson and C. G. Granqvist, Electrochromics for smart windows: thin films of tungsten oxide and nickel oxide, and devices based on these, *J. Mater. Chem.*, 2007, **17**, 127–156.

[90] D. Corr, U. Bach, D. Fay, M. Kinsella, C. McAtamney, F. O'Reilly, S. N. Rao and N. Stobie, Coloured electrochromic "paper–quality" displays based on modified mesoporous electrodes, *Solid State Ionics*, 2003, **165**, 315–321.

[91] C. Hilsum, Flat–panel electronic displays: a triumph of physics, chemistry and engineering, *Philos. Trans. R. Soc. A*, 2010, **368**, 1027–1082.

[92] R. S. Devan, R. A. Patil, J. H. Lin and Y. R. Ma, One–dimensional metal–oxide nanostructures: Recent developments in synthesis, characterization, and applications, *Adv. Funct. Mater.*, 2012, **22**, 3326–3370.

[93] D. S. Dalavi, R. S. Devan, R. a. Patil, R. S. Patil, Y.–R. Ma, S. B. Sadale, I. Kim, J.–H. Kim and P. S. Patil, Efficient electrochromic performance of nanoparticulate WO_3 thin films, *J. Mater. Chem. C*, 2013, **1**, 3722–3728.

[94] W. Cheng, E. Baudrin, B. Dunn and J. I. Zink, Synthesis and electrochromic properties of mesoporous tungsten oxide, *J. Mater. Chem.*, 2001, **11**, 92–97.

[95] S. H. Baeck, K. S. Choi, T. F. Jaramillo, G. D. Stucky and E. W. McFarland, Enhancement of photocatalytic and electrochromic properties of electrochemically fabricated mesoporous WO_3 thin films, *Adv. Mater.*, 2003, **15**, 1269–1273.

[96] C.–P. Li, F. Lin, R. M. Richards, C. Engtrakul, R. C. Tenent and C. a. Wolden, The influence of sol–gel processing on the electrochromic properties of mesoporous WO_3 films produced by ultrasonic spray deposition, *Sol. Energy Mater. Sol. Cells*, 2014, **121**, 163–170.

[97] S. Sallard, T. Brezesinski and B. M. Smarsly, Electrochromic stability of WO_3 thin films with nanometer–scale periodicity and varying degrees of crystallinity, *J. Phys. Chem. C*, 2007, **111**, 7200–7206.

[98] Y. Ohko, T. Tatsuma, T. Fujii, K. Naoi, C. Niwa, Y. Kubota and A. Fujishima, Multicolour photochromism of TiO_2 films loaded with silver nanoparticles, *Nat. Mater.*, 2003, **2**, 29–31.

[99] N. Crespo–Monteiro, N. Destouches, L. Bois, F. Chassagneux, S. Reynaud and T. Fournel, Reversible and irreversible laser microinscription on silver–containing mesoporous titania films, *Adv. Mater.*, 2010, **22**, 3166–3170.

[100] L. Raboin, M. Matheron, J. Biteau, T. Gacoin and J.–P. Boilot, Photochromism of in mesoporous organosilica films, *J. Mater. Chem.*, 2008, **18**, 3242–3248.

[101] F. Krohm, J. Kind, R. Savka, M. Alcaraz Janßen, D. Herold, H. Plenio, C. M. Thiele and a. Andrieu–Brunsen, Photochromic spiropyran– and spirooxazine–homopolymers in mesoporous thin films by surface initiated ROMP, *J. Mater. Chem. C*, 2016, **4**, 4067–4076.

[102] L. Bois, F. Chassagneux, Y. Battiez, F. Bessueille, L. Mollet, S. Parola, N. Destouches, N. Toulhoat and N. Moncoffre, Chemical growth and photochromism of silver nanoparticles into a mesoporous titania template, *Langmuir*, 2010, **26**, 1199–1206.

[103] O. Madelung, *Semiconductors–Basic Data*, 2nd ed.; Springer–Verlag: Berlin, 1996.

[104] A. M. Ganose and D. O. Scanlon, Band gap and work function tailoring of SnO_2 for improved transparent conducting ability in photovoltaics, *J. Mater. Chem. C*, 2016, **4**, 1467–1475.

[105] A. F. Khan, M. Mehmood, A. M. Rana and M. T. Bhatti, Effect of annealing on electrical resistivity of rf–magnetron sputtered nanostructured SnO_2 thin films, *Appl. Surf. Sci.*, 2009, **255**, 8562–8565.

[106] D. Tsokkou, A. Othonos and M. Zervos, Carrier dynamics and conductivity of SnO_2 nanowires investigated by time–resolved terahertz spectroscopy, *Appl. Phys. Lett.*, 2012, **100**, 133101.

[107] S. Das and V. Jayaraman, SnO_2: A comprehensive review on structures and gas sensors, *Prog. Mater. Sci.*, 2014, **66**, 112–255.

[108] C. Liu, Q. Kuang, Z. Xie and L. Zheng, The effect of noble metal (Au, Pd and Pt) nanoparticles on the gas sensing performance of SnO_2 –based sensors: a case study on the {221} high–index faceted SnO_2 octahedra, *CrystEngComm*, 2015, **17**, 6308–6313.

[109] J. Rebholz, P. Bonanati, C. Jaeschke, M. Hübner, L. Mädler, U. Weimar and N. Barsan, Conduction mechanism in undoped and antimony doped SnO_2 based FSP gas sensors, *Sensors Actuators, B Chem.*, 2013, **188**, 631–636.

[110] C. Han, S. Han and S. P. Khatkar, Enhancement of H_2–sensing properties of F–doped SnO_2 sensor by surface modification with SiO_2, *Sensors*, 2006, **6**, 492–502.

[111] T. Brezesinski, A. Fischer, K. I. Iimura, C. Sanchez, D. Grosso, M. Antonietti and B. M. Smarsly, Generation of self–assembled 3D mesostructured SnO_2 thin films with highly crystalline frameworks, *Adv. Funct. Mater.*, 2006, **16**, 1433–1440.

[112] W. Zeng, Y. Li, B. Miao, L. Lin and Z. Wang, Recognition of carbon monoxide with SnO_2/Ti thick–film sensor and its gas–sensing mechanism, *Sensors Actuators, B Chem.*, 2014, **191**, 1–8.

[113] V. K. Tomer and S. Duhan, A facile nanocasting synthesis of mesoporous Ag–doped SnO_2 nanostructures with enhanced humidity sensing performance, *Sensors Actuators, B Chem.*, 2016, **223**, 750–760.

[114] L. Li, H. Lin and F. Qu, Synthesis of mesoporous SnO_2 nanomaterials with selective gas–sensing properties, *J. Sol–Gel Sci. Technol.*, 2013, 545–555.

[115] H. Zhang, L. Wang, Z. Tan, Z. Li, G. Ding, Z. Jiao and P. Gu, Preparation of SnO_2 nanoparticles by hard template method for high selectivity gas sensors, *J. Nanosci. Nanotechnol.*, 2011, **11**, 11023–11027.

[116] J. K. Shon, S. S. Kong, Y. S. Kim, J. H. Lee, W. K. Park, S. C. Park and J. M. Kim, Solvent–free infiltration method for mesoporous SnO_2 using mesoporous silica templates, *Microporous Mesoporous Mater.*, 2009, **120**, 441–446.

[117] T. Aqeel, H. F. Greer, W. Z. Zhou, D. W. Bruce and A. Bumajdad, Novel direct synthesis of mesoporous tin dioxide network intact up to 500 °C, *J. Nano Res.*, 2016, **40**, 79–89.

[118] P. Yang, D. Zhao, D. I. Margolese, B. F. Chmelka and G. D. Stucky, Block copolymer templating syntheses of mesoporous metal oxides with large ordering lengths and semicrystalline framework, *Chem. Mater.*, 1999, **11**, 2813–2826.

[119] V. N. Urade and H. W. Hillhouse, Synthesis of thermally stable highly ordered nanoporous tin oxide thin films with a 3D face–centered orthorhombic nanostructure, *J. Phys. Chem. B*, 2005, **109**, 10538–10541.

[120] J. H. Pan, S. Y. Chai, C. Lee, S. Park and W. I. Lee, Controlled formation of highly crystallized cubic and hexagonal mesoporous SnO_2 thin films, *J. Phys. Chem. C*, 2007, **111**, 5582–5587.

[121] D. I. Fried, A. Ivanova, V. Müller, J. Rathousky, B. M. Smarsly and D. Fattakhova–Rohlfing, A facile synthesis of mesoporous crystalline tin oxide films involving a base–triggered formation of sol–gel building blocks., *Nanoscale*, 2011, **3**, 1234–1239.

[122] M. Dimitrov, T. Tsoncheva, S. Shao and R. Köhn, Novel preparation of nanosized mesoporous SnO_2 powders: Physicochemical and catalytic properties, *Appl. Catal. B Environ.*, 2010, **94**, 158–165.

52

[123] H. S. Oh, H. N. Nong and P. Strasser, Preparation of mesoporous Sb–, F–, and in–doped SnO_2 bulk powder with high surface area for use as catalyst supports in electrolytic cells, *Adv. Funct. Mater.*, 2015, **25**, 1074–1081.

[124] S. Yang, W. Yue, J. Zhu, Y. Ren and X. Yang, Graphene–based mesoporous SnO_2 with enhanced electrochemical performance for lithium–ion batteries, *Adv. Funct. Mater.*, 2013, **23**, 3570–3576.

[125] D. Wang, P. Hu, J. Xu, X. Dong and Q. Pan, Fast response chlorine gas sensor based on mesoporous SnO_2, *Sensors Actuators, B Chem.*, 2009, **140**, 383–389.

[126] X. Wang, S. Qiu, J. Liu, C. He, G. Lu and W. Liu, Synthesis of mesoporous SnO_2 spheres and application in gas sensors, *Eur. J. Inorg. Chem.*, 2014, 863–869.

[127] Y. Wang, T. Brezesinski, M. Antonietti and B. Smarsly, Ordered mesoporous Sb–, Nb–, and Ta–doped SnO_2 thin films with adjustable doping levels and high electrical conductivity, *ACS Nano*, 2009, **3**, 1373–1378.

[128] J. T. Park, S. H. Ahn, D. K. Roh, C. S. Lee and J. H. Kim, Multifunctional organized mesoporous tin oxide films templated by graft copolymers for dye–sensitized solar cells, *ChemSusChem*, 2014, **7**, 2037–2047.

[129] S. Shao, H. Wu, S. Wang, Q. Hong, R. Koehn, T. Wu and W.–F. Rao, Highly crystalline and ordered nanoporous SnO_2 thin films with enhanced acetone sensing property at room temperature, *J. Mater. Chem. C*, 2015, **3**, 10819–10829.

[130] H. Long, A. Harley–Trochimczyk, T. He, T. Pham, Z. Tang, T. Shi, A. Zettl, W. Mickelson, C. Carraro and R. Maboudian, In Situ Localized Growth of Porous Tin Oxide Films on Low Power Microheater Platform for Low Temperature CO Detection, *ACS Sensors*, 2016, **1**, 339–343.

[131] K. H. J. Buschow and F. R. De Boer, *Physics of Magnetism and Magnetic Materials*, Kluwer Academic Publishers, 2003.

[132] D. Askeland, P. Fulay and W. Wright, *The Science and engineering of materials*, Cengage Learning, 2010.

[133] R. Jackson, John Tyndall and the early history of diamagnetism, *Ann Sci*, 2015, **72**, 435–489.

[134] L. B. Kong, Z. W. Li, G. Q. Lin and Y. B. Gan, Magneto–dielectric properties of Mg–Cu–Co ferrite ceramics: II. electrical, dielectric, and magnetic properties, *J. Am. Ceram. Soc.*, 2007, **90**, 2104–2112.

[135] R. Zhang and R. F. Willis, Thickness–dependent curie temperatures of ultrathin magnetic films: Effect of the range of spin–spin interactions, *Phys. Rev. Lett.*, 2001, **86**, 2665–2668.

[136] L. He, C. Chen, N. Wang, W. Zhou and L. Guo, Finite size effect on Néel temperature with Co_3O_4 nanoparticles, *J. Appl. Phys.*, 2007, **102**, 103911.

[137] S. A. Wolf, D. D. Awschalom, R. A. Buhrman, J. M. Daughton, S. von Molnár, M. L. Roukes, A. Y. Chtchelkanova and D. M. Treger, Spintronics: A Spin–Based Electronics Vision for the Future, *Science*, 2001, **294**, 1488–1495.

[138] M. N. Baibich, J. M. Broto, A. Fert, F. N. Van Dau, F. Petroff, P. Eitenne, G. Creuzet, A. Friederich and J. Chazelas, Giant magnetoresistance of (001)Fe/(001)Cr magnetic superlattices, *Phys. Rev. Lett.*, 1988, **61**, 2472–2475.

[139] G. Binasch, P. Grünberg, F. Saurenbach and W. Zinn, Enhanced magnetoresistance in layered magnetic structures with antiferromagnetic interlayer exchange, *Phys. Rev. B*, 1989, **39**, 4828–4830.

[140] B. Dieny, V. S. Speriosu, S. S. P. Parkin, B. A. Gurney, D. R. Wilhoit and D. Mauri, Giant magnetoresistive in soft ferromagnetic multilayers, *Phys. Rev. B*, 1991, **43**, 1297–1300.

[141] D. D. Awschalom and M. E. Flatté, Challenges for semiconductor spintronics, *Nat. Phys.*, 2007, **3**, 153–159.

[142] Application of GMR, University of Nebraska–Lincoln, http://unlcms.unl.edu/cas/physics/tsymbal/reference/giant_magnetoresistance/application_%20of_gmr.shtml

[143] C. Zener, Interaction between the d shells in the transition metals, *Phys. Rev.*, 1951, **81**, 440–444.

[144] T. Dietl, A. Haury and Y. Merle d'Aubigné, Free carrier–induced ferromagnetism in structures of diluted magnetic semiconductors, *Phys. Rev. B*, 1997, **55**, R3347–R3350.

[145] T. Dietl, A ten–year perspective on dilute magnetic semiconductors and oxides, *Nat. Mater.*, 2010, **9**, 965–974.

[146] Y. Fukuma, H. Asada, S. Miyawaki, T. Koyanagi, S. Senba, K. Goto and H. Sato, Carrier–induced ferromagnetism in $Ge_{0.92}Mn_{0.08}Te$ epilayers with a Curie temperature up to 190 K, *Appl. Phys. Lett.*, 2008, **93**, 252502.

[147] L. Chen, S. Yan, P. F. Xu, J. Lu, W. Z. Wang, J. J. Deng, X. Qian, Y. Ji and J. H. Zhao, Low–temperature magnetotransport behaviors of heavily Mn–doped (Ga,Mn)As films with high ferromagnetic transition temperature, *Appl. Phys. Lett.*, 2009, **95**, 182505.

[148] K. Zhao, B. Chen, G. Zhao, Z. Yuan, Q. Liu, Z. Deng, J. Zhu and C. Jin, Ferromagnetism at 230 K in $(Ba_{0.7}K_{0.3})(Zn_{0.85}Mn_{0.15})_2As_2$ diluted magnetic semiconductor, *Chinese Sci. Bull.*, 2014, **59**, 2524–2527.

[149] B. Gu and S. Maekawa, Diluted magnetic semiconductors with narrow band gaps, *Phys. Rev. B*, 2016, **94**, 155202.

[150] R. Singh, Unexpected magnetism in nanomaterials, *J. Magn. Magn. Mater.*, 2013, **346**, 58–73.

[151] Y. Matsumoto, M. Murakami, T. Shono, T. Hasegawa, T. Fukumura, M. Kawasaki, P. Ahmet, T. Chikyow, S. Koshihara and H. Koinuma, Room–temperature ferromagnetism in transparent transition metal–doped titanium dioxide, *Science*, 2001, **291**, 854–857.

[152] J. Philip, A. Punnoose, B. I. Kim, K. M. Reddy, S. Layne, J. O. Holmes, B. Satpati, P. R. Leclair, T. S. Santos and J. S. Moodera, Carrier–controlled ferromagnetism in transparent oxide semiconductors, *Nat. Mater.*, 2006, **5**, 298–304.

[153] C. Song, X. J. Liu, K. W. Geng, F. Zeng, F. Pan, B. He and S. Q. Wei, Transition from diluted magnetic insulator to semiconductor in Co–doped ZnO transparent oxide, *J. Appl. Phys.*, 2007, **101**, 103903.

154 T. Dietl, Zener model description of ferromagnetism in zinc–blende magnetic semiconductors, *Science*, 2000, **287**, 1019–1022.

155 J. M. D. Coey, Dilute magnetic oxides, *Curr. Opin. Solid State Mater. Sci.*, 2006, **10**, 83–92.

156 X. Yang, Y. Li, C. Shen, B. Si, Y. Sun, Q. Tao, G. Cao, Z. Xu and F. Zhang, Sr and Mn co–doped LaCuSO: A wide band gap oxide diluted magnetic semiconductor with T_C around 200 K, *Appl. Phys. Lett.*, 2013, **103**, 022410.

157 S. B. Ogale, R. J. Choudhary, J. P. Buban, S. E. Lofland, S. R. Shinde, S. N. Kale, V. N. Kulkarni, J. Higgins, C. Lanci, J. R. Simpson, N. D. Browning, S. Das Sarma, H. D. Drew, R. L. Greene and T. Venkatesan, High temperature ferromagnetism with a giant magnetic moment in transparent Co–doped $SnO_{2-\delta}$, *Phys. Rev. Lett.*, 2003, **91**, 77205.

158 H. Saadaoui, X. Luo, Z. Salman, X. Y. Cui, N. N. Bao, P. Bao, R. K. Zheng, L. T. Tseng, Y. H. Du, T. Prokscha, A. Suter, T. Liu, Y. R. Wang, S. Li, J. Ding, S. P. Ringer, E. Morenzoni and J. B. Yi, Intrinsic ferromagnetism in the diluted magnetic semiconductor $Co:TiO_2$, *Phys. Rev. Lett.*, 2016, **117**, 227202.

159 B. Prajapati, S. Kumar, M. Kumar, S. Chatterjee and A. K. Ghosh, Investigation of the physical properties of $Fe:TiO_2$–diluted magnetic semiconductor nanoparticles, *J. Mater. Chem. C*, 2017, **5**, 4257–4267.

160 H. Akai, Ferromagnetism and its stability in the diluted magnetic semiconductor (In, Mn) As, *Phys. Rev. Lett.*, 1998, **81**, 3002–3005.

161 K. Sato, P. H. Dederichs, H. Katayama–Yoshida and J. Kudrnovský, Exchange interactions in diluted magnetic semiconductors, *J. Phys. Condens. Matter*, 2004, **16**, S5491–S5497.

162 K. Sato, L. Bergqvist, J. Kudrnovský, P. H. Dederichs, O. Eriksson, I. Turek, B. Sanyal, G. Bouzerar, H. Katayama–Yoshida, V. A. Dinh, T. Fukushima, H. Kizaki and R. Zeller, First–principles theory of dilute magnetic semiconductors, *Rev. Mod. Phys.*, 2010, **82**, 1633–1690.

163 A. Walsh, J. L. F. Da Silva and S.–H. Wei, Theoretical description of carrier mediated magnetism in cobalt doped ZnO. *Phys. Rev. Lett.*, 2008, **102**, 256401.

164 J. M. Coey, M. Venkatesan and C. B. Fitzgerald, Donor impurity band exchange in dilute ferromagnetic oxides, *Nat Mater*, 2005, **4**, 173–179.

165 J. E. Jaffe, T. C. Droubay and S. A. Chambers, Oxygen vacancies and ferromagnetism in $Co_xTi_{1-x}O_{2-x-y}$, *J. Appl. Phys.*, 2005, **97**, 73908.

166 V. K. Sharma and G. D. Varma, Oxygen vacancies induced room temperature ferromagnetism in hydrogenated Mn–doped ZnO, *J. Appl. Phys.*, 2007, **102**, 056105.

167 Y. An, Y. Ren, D. Yang, Z. Wu and J. Liu, Oxygen vacancy–induced room temperature ferromagnetism and magnetoresistance in Fe–doped In_2O_3 films, *J. Phys. Chem. C*, 2015, **119**, 4414–4421.

168 J. M. D. Coey, K. Wongsaprom, J. Alaria and M. Venkatesan, Charge–transfer ferromagnetism in oxide nanoparticles, *J. Phys. D. Appl. Phys.*, 2008, **41**, 134012.

169 J. Gu, L. Liu, Y. Qi, Q. Xu, H. Zhang and H. Sun, Magnetic characterization of diluted magnetic semiconductor thin films, *J. Appl. Phys.*, 2011, **109**, 23902.

[170] S. A. Aravindh, U. Schwingenschloegl and I. S. Roqan, Ferromagnetism in Gd doped ZnO nanowires: A first principles study, *J. Appl. Phys.*, 2014, **116**, 233906.

[171] W. Wan, J. Huang, L. Zhu, L. Hu, Z. Wen, L. Sun and Z. Ye, Defects induced ferromagnetism in ZnO nanowire arrays doped with copper, *CrystEngComm*, 2013, **15**, 7887.

[172] B. Choudhury and A. Choudhury, Room temperature ferromagnetism in defective TiO_2 nanoparticles: Role of surface and grain boundary oxygen vacancies, *J. Appl. Phys.*, 2013, **114**, 203906.

[173] N. Deng, J. Li, B. Hong, D. Jin, X. Peng, X. Wang, H. Ge and H. Jin, Nanocasting synthesis of co–doped In_2O_3: a 3D diluted magnetic semiconductor composed of nanospheres, *J. Nanoparticle Res.*, 2015, **17**, 191.

[174] E. Pellicer, M. Cabo, E. Rossinyol, P. Solsona, S. Suriñach, M. D. Baró and J. Sort, Nanocasting of mesoporous In–TM (TM = Co, Fe, Mn) oxides: Towards 3D diluted–oxide magnetic semiconductor architectures, *Adv. Funct. Mater.*, 2013, **23**, 900–911.

[175] E. Pellicer, E. Menéndez, J. Fornell, J. Nogués, A. Vantomme, K. Temst and J. Sort, Mesoporous oxide–diluted magnetic semiconductors prepared by Co implantation in nanocast 3D–ordered In_2O_{3-y} materials, *J. Phys. Chem. C*, 2013, **117**, 17084–17091.

2. Experimental section

This chapter aims to introduce the fundamentals and working conditions of the main routes and instruments for the synthesis and characterization, respectively, of the samples.

2.1 Synthesis details

2.1.1 Nanocasting synthesis of undoped, Cu– and Ni–doped mesoporous SnO$_2$ powders

- **Synthesis of KIT–6 silica template**

KIT–6 silica was chosen as the hard template to prepare mesoporous undoped, Cu– and Ni–doped SnO$_2$ powders. P–123 (6 g) was dissolved in a mixture of deionized water (220 g) acidified with 37 wt.% HCl (12 g) by vigorous stirring (300 rpm/min) at 35 ºC for 4 h. Then, 1–butanol (6 g) was added into the solution whilst stirring for another hour. Thereafter, 12.49 g of tetraethyl orthosilicate (TEOS) as the silicon source was added drop by drop into the solution and stirred for 24 h at the same temperature. The reaction vessel (sealed) was introduced in an oven at 80 ºC for 24 h under static conditions. After the hydrothermal treatment, the resulting suspension was filtered and washed with deionized water several times. Finally, the collected powder was calcined in a tubular furnace at 550 ºC under air flowing for 4 h.

- **Synthesis of undoped, Cu– and Ni–doped mesoporous SnO$_2$ replicas**

SnCl$_2$·2H$_2$O (stannous chloride dihydrate, Sigma–Aldrich 99.99%) was used as SnO$_2$ precursor and NiCl$_2$ (nickel chloride, Sigma–Aldrich 98.0%) and CuCl$_2$·2H$_2$O (99.0%) as TM dopants.

KIT–6 silica (0.4 g), SnCl$_2$·2H$_2$O (0.6 g) and varying amounts of NiCl$_2$ or CuCl$_2$·2H$_2$O (at molar ratios of TM versus Sn(IV) of 0:100, 5:95, 15:85 and 20:80) were finely ground in an agate mortar and pestle. The resulting mixture was placed in a crucible and heated up to 85 ºC inside a vacuum furnace (pressure < 10^{-4} mbar) to promote the infiltration of tin and nickel or copper precursors within the KIT–6 silica host. After 24 h, the samples were taken out and transferred into a tubular furnace for high temperature solid state reaction under air atmosphere. The temperature and heat treatment time were set at 700 ºC and 2 h, respectively. Following the conversion of tin and nickel/copper precursors, the silica template was selectively etched away using 1 M NaOH aqueous solution at 70 ºC. Finally, the resulting powders were cleaned with deionized water and absolute ethanol and dried in an oven.

2.1.2 Preparation of Ni–doped mesoporous SnO$_2$ films by EISA

P–123 (0.12 g) was dissolved in absolute ethanol (6 mL) by vigorous stirring (300 rpm/min) at room temperature. Next, SnCl$_4$ (0.55 g) and deionized water (0.4 mL) were added to the previous solution. The resulting mixture led to pure SnO$_2$ film, which was taken as a

reference. For the Ni–doped SnO$_2$ films, precursor solutions containing [Ni(II)]/[Sn(IV)] molar ratios of 5:95, 10:90, 15:85 and 20:80 were targeted. To this end, different amounts of NiCl$_2$ (0.0144 g, 0.0304 g, 0.0483 g, 0.0684 g, respectively) were added to the Sn(IV) solution. The SnCl$_4$ concentration was kept constant in each synthesis. The resulting solutions were sealed and aged for 12 h at room temperature before deposition. Prior to deposition, Si substrates were cleaned with acetone and Milli–Q water in an ultrasonic bath for 5 min each, and then rinsed with absolute ethanol. The mesoporous films were prepared in an automatic dip coater (see below).

2.2 Dip–coating

2.2.1 Origin and fundamentals of the technique

Among the different thin film deposition techniques, dip–coating is one of the oldest wet chemical coating process. The first patent on SiO$_2$ sol–gel thin films was developed by W. Geffcken and E. Berger in 1939.[1] To date, dip–coating is applied in a wide range of applications such as dielectrics, catalysis, membranes, sensors, superconducting layers, etc. [2,3,4] Essentially, the dip–coating process comprises four stages (Fig. 2.1): (1) immersion of the substrate into the solution; (2) withdrawal of the substrate at an appropriate speed; (3) deposition of a thin layer of the precursor solution and (4) solvent evaporation.
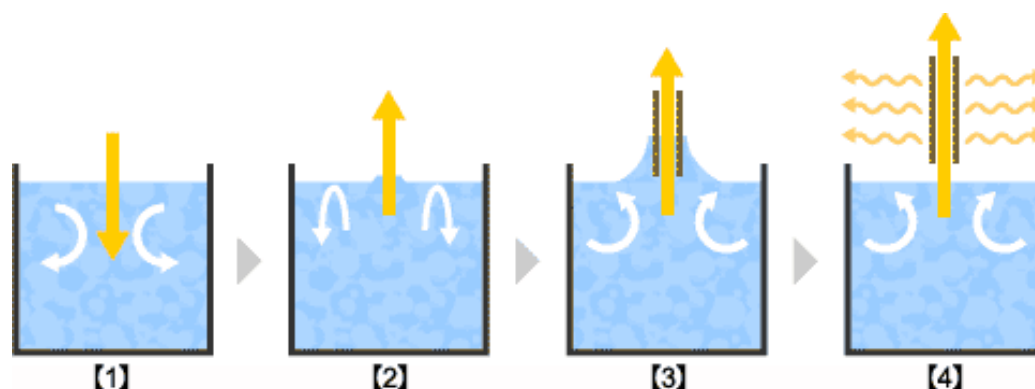
Fig. 2.1 Schematic illustration of dip–coating processes.[5]

2.2.2 Working conditions

An automatic dip coater (Fig. 2.2), from the Gnm^3 group, was used in the dip–coating process for the preparation of mesoporous SnO$_2$ films. The precursor sol–gel solution was coated onto single–crystal Si (111) substrates. The withdrawal speed and relative humidity were kept at 5 mm·s^{-1} and around 20%, respectively. After deposition, the resulting coatings were dried under ambient atmosphere for 30 min and then put into the furnace to be calcined under air at 100 ℃ for 12 h (heating ramp 1 ℃/min). Subsequently, the

temperature was increased to 200 °C for 2 h (heating ramp 3 °C/min) to consolidate the microstructure. Finally, the furnace was heated to 600 °C for 1h (heating ramp 3 °C/min) to eliminate all the remaining organic residues.
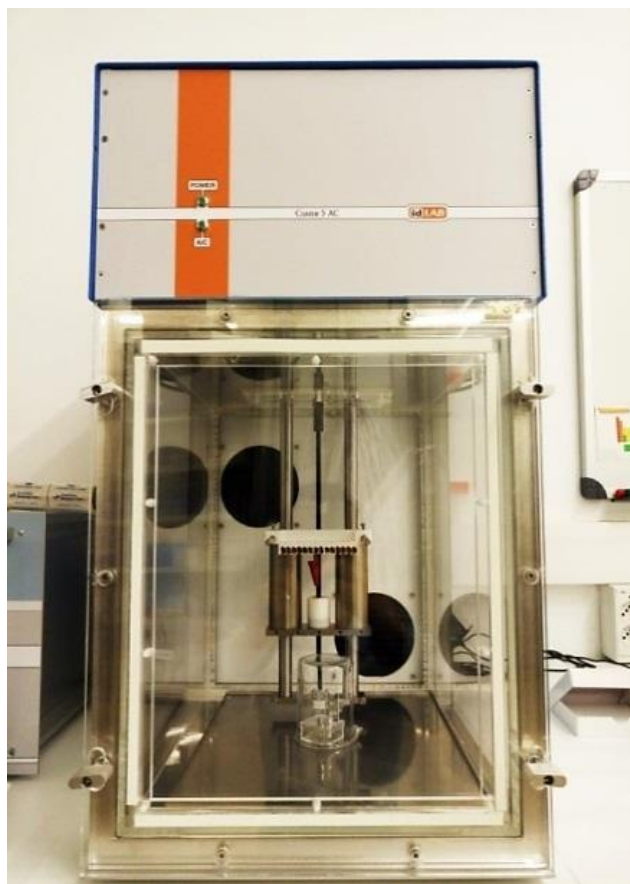
Fig. 2.2 Picture of the dip coater 5 AC (ID LAB).

2.3 Scanning electron microscopy

2.3.1 Origin and fundamentals of the technique

In 1838, M. Knoll proved theoretically that it was possible to build a scanning electron microscope (SEM). [6] The first prototype was built in 1938 by M. Von Ardenne. [7,8] In 1965, the Cambridge Instruments Company began to manufacture SEMs in industrial series. Since then, it has become an essential tool in many fields of scientific research ranging from biology to materials science. [9]

The main feature of a SEM, compared with conventional optical microscopes, is the use of electrons instead of light and of magnetic lenses instead of optical lenses. Under certain assumptions, electrons can be considered as waves, with wavelengths much smaller than the visible light. Therefore, the SEM enables the observation of very small structures that are not observable using optical microscopes due to diffraction effects.

2.3.2 Interaction between the electron beam and the sample

When an electron beam is bombarding the surface of a sample, different signals are produced. The penetration depth of electrons directly depends on the incidence angle of the beam, the magnitude of its current, the accelerating voltage, and the average atomic number (Z) of the sample. In the specimen interaction volume, several interactions between the electron beam and the atoms of the sample take place and, as a result, different types of signals can be studied (Fig. 2.3):
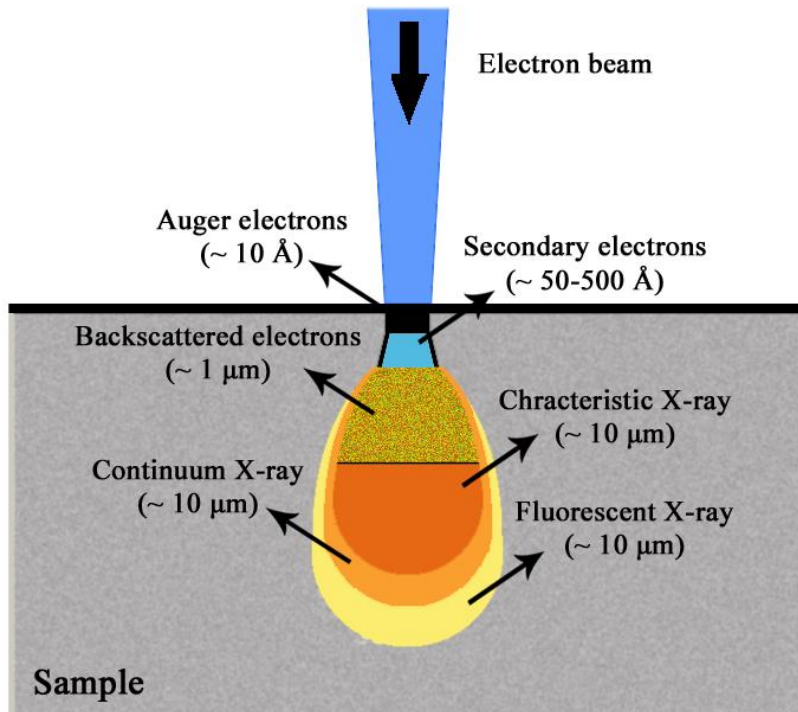
Fig. 2.3 Schematic illustration for various electron–specimen interactions.

Auger electrons: When a core state electron is expelled, an electron from a higher energy level may move to the inner–shell to cover this gap, resulting in a release of energy that can be transferred to an outer–shell electron. With enough energy, the outmost electron is ejected from the atom, the so–called Auger electron. These electrons typically have low values of energy, and therefore the depth range is between 0.5 and 2 nm. The energy of such electrons is characteristic of the emitting atom and the chemical environment in which the atom was located, and thus these electrons provide information about the composition of small regions of sample surface.

Secondary electrons: Secondary electrons are produced when an incident electron beam excites electrons of atoms near the surface and loses some of its energy in the process. The excited electron moves towards the surface of the sample undergoing elastic and inelastic collisions until it reaches the surface. From here it can escape if its energy exceeds the

surface work function (E_w), which is the amount of energy needed to remove electrons from the surface of a material. Secondary electrons are characterized by energies between 0 and 50 eV. They provide information on the topography of the surface. However, all information obtained from secondary electrons is restricted to a penetration of 10 nm.

Backscattered Electrons: Backscattered electrons are scattered out of the sample when the electron beam interacts elastically with the nuclei of sample atoms. The intensity of this effect varies proportionally with the mean atomic number of the sample. It is therefore used to obtain maps with information about the composition of the sample surface. Specifically, heavy elements (high Z) backscatter electrons more strongly than light elements (low Z), and thus appear brighter in the image.

Characteristic X–rays: When an incident electron collides with an atom in the sample, inducing the emission of another electron, the corresponding "hole" is immediately occupied by an electron from an outer, higher–energy shell. The difference in energy between the higher–energy shell and the lower–energy shell may be released in the form of an X–ray. The wavelengths of X–rays emitted are characteristic of the atoms in the sample. The resulting spectrum is used to study the elemental composition of the sample surface, the so–called energy dispersive X–ray spectroscopy (EDX) pattern.

2.3.3 Working conditions

The surface morphological observations and EDX analyses were performed on the Merlin Zeiss SEM located in the Microscopy Service of the *Universitat Autònoma de Barcelona.* For proper observation of the powders, these were dispersed in ethanol and then a small volume of the suspensions was dropped on the surface of carbon conductive tapes. Meanwhile, observation of the mesoporous thin films did not require any preparation. Due to the insulating or semiconductor nature of the samples under observation (i.e., silica and transition metal oxides), a low accelerating voltage was applied (typically around 3 kV for the powders and 0.8 kV for the films).

2.4 Transmission electron microscopy

2.4.1 Origin and fundamentals of the technique

The first transmission electron microscope (TEM) was developed between 1931 and 1933 by Ernst Ruska and Max Knoll.[10,11] Siemens produced the first commercial TEM in 1993. The basics of the first TEM remain today and the changes introduced in the modern microscopes consist of adding more lenses to reduce aberrations and fittings to offer greater versatility to the research teams.

The TEM emits an electron beam that is driven toward the object under observation by a system of magnetic lenses and it is based on the detection and visualization of electrons passing through the specimen. The objective lens collects the transmitted beam and forms the image display. The objective and selected area aperture are used to choose the elastically scattered electrons that will form the image. Finally, the beam goes to the magnifying system that controls the magnification of the image and the projector lens. The formed image is shown on a monitor. The operation of TEM requires an ultra–high vacuum and a high voltage. Moreover, the specimens must be thin enough ($\approx$ 200 nm) to be transparent to electrons.

We can distinguish two main types of microscopes, namely the low voltage and the high voltage (High–Resolution, HR) TEM. In the former the energy of electrons does not exceed 120 keV, while in the latter is of 200–300 keV.

2.4.2 Working conditions

TEM observations were made on a JEOL JEM–2011 microscope (200 keV), equipped with an EDX detector from Oxford Instruments, located at the Microscopy Service of the *Universitat Autònoma de Barcelona*. HR–TEM observations were performed on a Tecnai F20 HR–TEM/STEM microscope, located at *Institut Català de Nanociència i Nanotechnologia* (ICN2). For TEM/HR–TEM observations the powders were dispersed in ethanol and then one or two drops were placed dropwise onto holey or lacey carbon supported grids.

2.5 Electron energy loss spectroscopy

2.5.1 Origin and fundamentals of the technique

Electron energy loss spectroscopy (EELS) technique was developed by J. Hillier and R. F. Baker in 1944 but was not widely used over the next 50 years, [12,13] only becoming more widespread in research in the 1990s due to advances both in microscope instrumentation and vacuum technology. Usually, EELS instrumentation is incorporated to TEM or scanning transmission electron microscope (STEM). The collecting of EELS signal is based on the energy distribution of initially monoenergetic electrons after they pass through a thin sample (Fig. 2.4). [13]

When the electrons pass the sample, some of the electrons undergo inelastic scattering. Thus, these electrons lose some energy and then their paths are slightly and randomly deflected. Among all the inelastic interactions, the inner–shell ionization is used to detect the elemental components of a sample and create images with unique contrast effects.

Nowadays, EELS has become a powerful technique for obtaining the composition and chemical information from a small region (sub–nanometer diameter) in the sample.[14] In some cases, the resolution can even reach to single atoms.[15],[16]
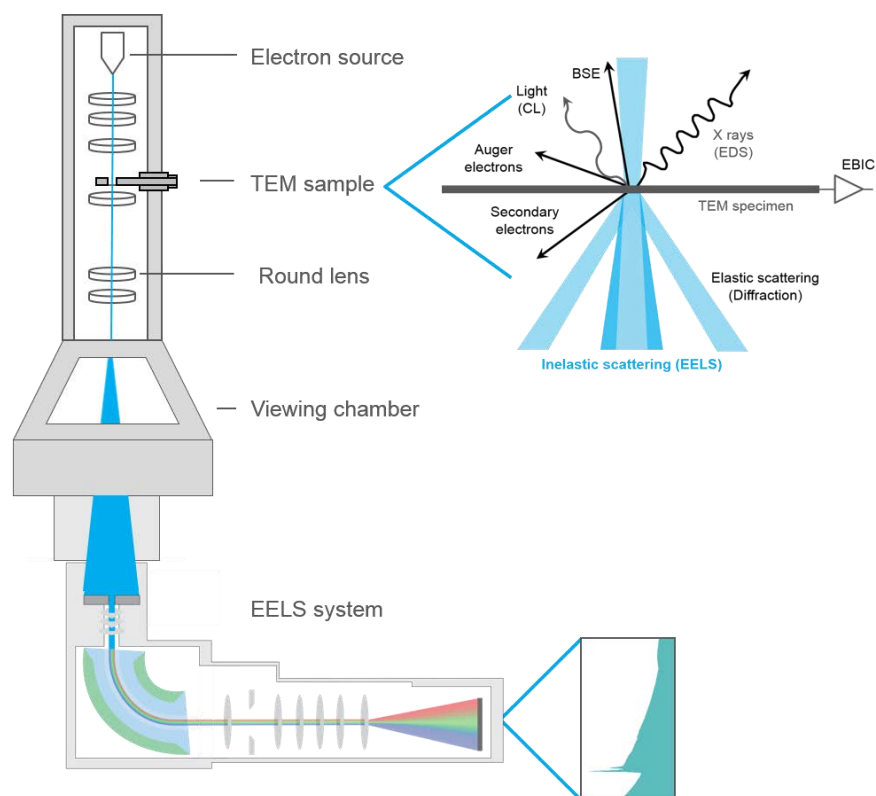
Fig. 2.4 Schematic illustration of the generation of electron energy loss spectrum.[17]

2.5.2 Working conditions

EELS analyses were performed on a Tecnai F20 HR–TEM/STEM microscope, located at *Institut Català de Nanociència i Nanotechnologia* (ICN2). The EELS signal was recorded in STEM mode at 200 kV using a Gatan Quantum SE 963 Imaging Filter (GIF).

2.6 X–ray diffraction

2.6.1 Origin and fundamentals of the technique

Max von Laue conducted the first X–ray diffraction experiment in 1912, demonstrating that X–rays had a wavelength comparable to atomic spacing crystals, so that they could undergo diffraction. This phenomenon was later on confirmed by Paul Knipping and Walter Friedrich.[18]

Starting from the assumption that the incident X–ray beam is monochromatic (a single wavelength) and is perfectly collimated, when the beam is focused onto the sample with an incident angle θ with respect to the reticular planes of the crystal, the following condition is satisfied:

$$n\lambda = 2d \sin \theta \qquad \text{[Eq. 2.1]}$$

where n is the order of reflection and d is the interplanar distance of a family of crystallographic planes. When this relationship is satisfied, X–rays are in phase and form a constructive interference. This condition is known as Bragg's law and can be used to determine the angular position of peaks in a particular family of diffracted planes. [19,20]

Bragg's law assumes that the crystal is perfect (i.e., it is free from structural defects) and that the incident beam, as mentioned before, is perfectly monochromatic and collimated. The size of the crystals (average coherently diffracting domain) and the microdeformations eventually present in the sample contribute to the width of diffracted peaks. [21] The procedure used to evaluate the crystallite size is based on the consideration that the peaks can be adjusted to a pseudo–Voigt function, which is a linear combination of Gaussian and Lorentzian (Cauchy) functions. [22] Using this approximation, the crystal size can be determined from the Lorentzian as the integral of the peak width, β_C^f:

$$d_{hkl} = \frac{\lambda}{\beta_C^f * \cos(\theta)} \qquad \text{[Eq. 2.2]}$$

Where θ is the angular position of the peak (in degree) and λ is the wavelength (in Armstrong). This equation is known as the Scherrer formula. [23] Similarly, the microdeformations can be determined from the Gaussian contribution upon integrating the peak width, β_G^f:

$$microdeformation = < e > = \frac{\beta_G^f}{4 \tan(\theta)} \qquad \text{[Eq. 2.3]}$$

2.6.2 Working conditions

The XRD patterns of mesoporous powders were acquired on a Philips X'Pert equipment located at the Diffraction Service of the *Universitat Autònoma de Barcelona*. Cu–Kα radiation (λ = 1.54060 Å) was used as the incident beam, at a voltage of 45 kV and a current of 40 mA. The powders were mounted on a single crystal silicon support. The 2θ angular range was ranged from 20° to 80° with step time of 0.78 s and step size of 0.026°.

Meanwhile, the XRD patterns of the mesoporous films were measured on a PANalytical X'pert PRO MRD (Materials Research Diffractometer), by grazing incidence X–ray diffraction at an incidence angle of 1.18°. The diffraction patterns were acquired in the 2θ angular range varying from 20° to 80° with step time of 0.8 s and step size of 0.03°.

In addition, the small angle XRD measurements were performed on a PANalytical X'pert PRO MOD (Multi–Purpose Diffractometer) with an X'Celerator linear detector. The 2θ angular range was varied from 0.5° to 3° with step time of 56.05 s and step size of 0.033°.

The identification of phases was carried out from the comparison of XRD spectra obtained with the JCPDS database. The values of crystallite size, microstrains and lattice parameters as a function of dopant content were extracted by Materials Analysis Using Diffraction (MAUD), a general diffraction/reflectivity analysis program based on the Rietveld method.[24]

2.7 X–ray photoelectron spectroscopy (XPS)

2.7.1 Origin and fundamentals of the technique

Though the photoelectric effect was already discovered by Heinrich Hertz in 1887 and well explained by Albert Einstein in 1905, the capabilities of X–ray photoelectron spectroscopy as a characterization technique were not fully exploited until Siegbahn made several significant improvements in the equipment.[25] Later, in 1969, the first commercial monochromatic XPS instrument was fabricated by Hewlett–Packard Company.[26] Since then, XPS, as a surface–sensitive quantitative spectroscopic technique, has been widely used for the detection of the elemental composition, chemical state and electronic state of the specimens. A typical schematic illustration the basic components of an XPS apparatus is shown in Fig. 2.5.

XPS spectra are obtained by irradiating the sample with X–ray beam while simultaneously an energy analyzer measures the kinetic energy and number of electrons which are excited from the surface and near surface region (0–10 nm) of the material. In practice, using laboratory–scale X–ray sources, this technique can detect all elements except hydrogen and helium. Generally, an ultra–high vacuum is required during the whole procedure and ion beam etching is often used before the measurement to clean off the surface contamination.
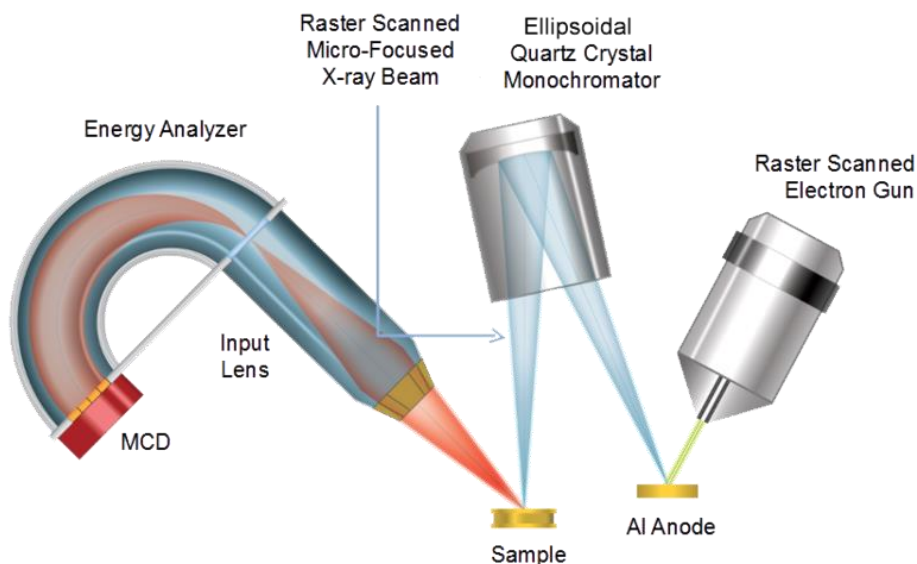
Fig. 2.5 Schematic illustration of the basic components of an XPS instrument.[27]

2.7.2 Working conditions

XPS analyses were carried out on a spectrometer (PHI 5500 Multi–technique System) equipped with a monochromatic X–ray source (Al–Kα line of 1486.6 eV energy and 350 W), which was placed perpendicular to the analyzer axis and calibrated using the $3d_{5/2}$ line of Ag with a full width at half maximum (FWHM) of 0.8 eV. During the measurements, the chamber pressure was kept in the range from 5×10^{-9} to 2×10^{-8} Torr. The analyzed area of each sample was a circular spot of 0.8 mm in diameter. Ar^+ ion etching with the energy of 3 keV was applied in some cases (Ni–doped SnO_2 powder and films). All binding energies were corrected according to the position of adventitious C 1s (284.50 eV).[28,29]

2.8 Superconducting quantum interference device

2.8.1 Origin and fundamentals of the technique

Superconducting quantum interference device (SQUID) is a characterization technique that detects very tiny magnetic fields that can be wound up to a magnetic flux quanta, with noise levels less than 3 fT/sqrt(Hz).[30] Generally, the SQUID equipment can be divided into two main types: direct current (DC) and radio frequency (RF). The DC SQUID and RF SQUID were invented in 1964 and 1965, respectively, after the Josephson junction was made in 1963 by P. W. Anderson and J. M. Rowell.[31,32] The operating principle of the SQUID is thus based on the development of the Josephson junction (Fig. 2.6) in 1963.[33,34]
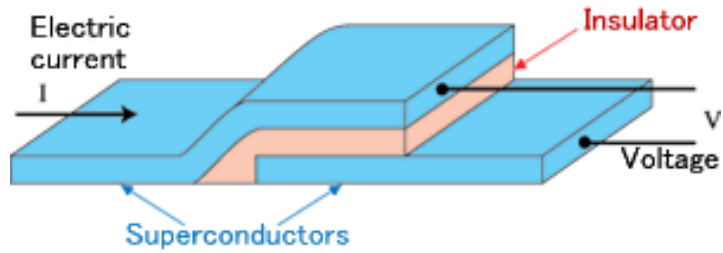
Fig. 2.6 Schematic drawing of the Josephson junction.

The base electrode of the SQUID is made of a thin layer of pure lead (usually in the form of an alloy with 10% gold or indium to improve the mechanical properties), or niobium prepared by deposition. The tunnel barrier is formed by oxidation on the surface of niobium. The upper electrode is a lead alloy layer deposited on the other two, in a sandwiched position. The Josephson junction is very sensitive to changes of current during a few picoseconds, which is suitable for direct observation of quantum electrodynamic effects.

2.8.2 Working conditions

Hysteresis loops were recorded on a Quantum Design MPMS–XL, located at the *Institut de Ciència de Materials de Barcelona* (ICMAB). A superconducting longitudinal solenoid (Fig. 2.7) was used to generate magnetic fields. Theoretically, the maximum magnetic field can reach up to 7 T and the temperature at the sample space can be precisely controlled from 2 K to 400 K.
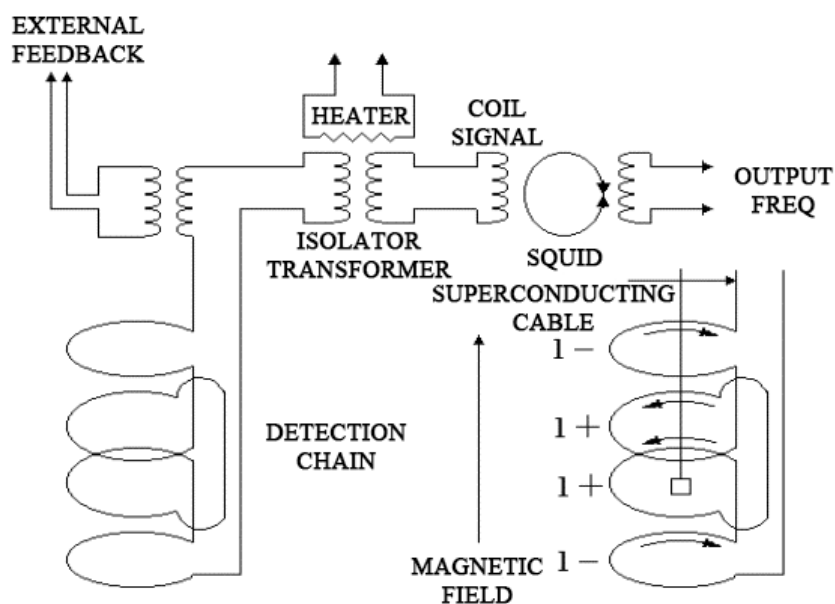
Fig. 2.7 The longitudinal structure of the SQUID system.

For the Ni/Cu–doped mesoporous SnO_2 powders, gelatin capsules were filled with the samples. Magnetic hysteresis loops were acquired at cryogenic and room temperatures while the magnetic field was ranged from –5 T to 5 T.

2.9 Vibrating sample magnetometer

2.9.1 Origin and fundamentals of the technique

The vibrating sample magnetometer (VSM) was invented in 1955 by Simon Foner at Lincoln Laboratory and his work was published shortly afterwards in 1959.[35] The principle of this magnetometer (Fig. 2.8) is to measure the electromotive force induced by a ferromagnetic sample when it is vibrating sinusoidally (typically using a piezoelectric material), under the presence of a static and uniform magnetic field (H). According to the Faraday's law, the electromotive force induced in a coil, V_{fem}, is proportional to the temporal variation of the magnetic flux passing through it:

$$V_{fem} = -\frac{d\emptyset}{dt} \qquad \text{[Eq. 2.4]}$$

where ϕ is the magnetic flux and t is the time. [36]

VSM use linear attenuators of some form and historically the development of these systems was done using modified audio speakers, though this approached was dropped due to the interference through the in–phase magnetic noise produced, as the magnetic flux through a nearby pickup coil varies sinusoidally.

Considering a solenoid consisting of N turns of constant cross section A, the magnetic induction inside the coil, B, can be written as follows:

$$B = \frac{\emptyset}{A} N \qquad \text{[Eq. 2.5]}$$

Therefore,

$$V_{fem} = -NA\frac{dB}{dt} \qquad \text{[Eq. 2.6]}$$

Since the sample is vibrating, the magnetic moment can be represented as $m(t)=m_0 \cdot \sin(ft)$, where m_0 is the moment amplitude and f is the frequency. Since $B = \mu_0(H + M)$, $M = m/V$ (being B the magnetic induction, M the magnetization and V the volume of the sample) and the fact that H is constant, dB/dt can be acquired from the following equation:

$$\frac{dB}{dt} = \left(\frac{\mu_0 m_0 f}{V}\right)\cos(ft)$$ [Eq. 2.7]

Hence, the amplitude induced voltage in the pickup coil is proportional to the sample's magnetic moment, but does not depend on the strength of the applied magnetic field:

$$V_{fem} \propto fm_0 G(z)$$ [Eq. 2.8]

where $G(z)$ is a function that defines the dependence of V_{fem} with respect to the sample position in the holder relative to the coils and, therefore, it depends on the design of the coils. Essentially, the VSM measures the difference of magnetic induction between one region of space with the sample and another without the sample, thus allowing calculation of the magnetic moment (m), and obtain the hysteresis loops of a certain material.
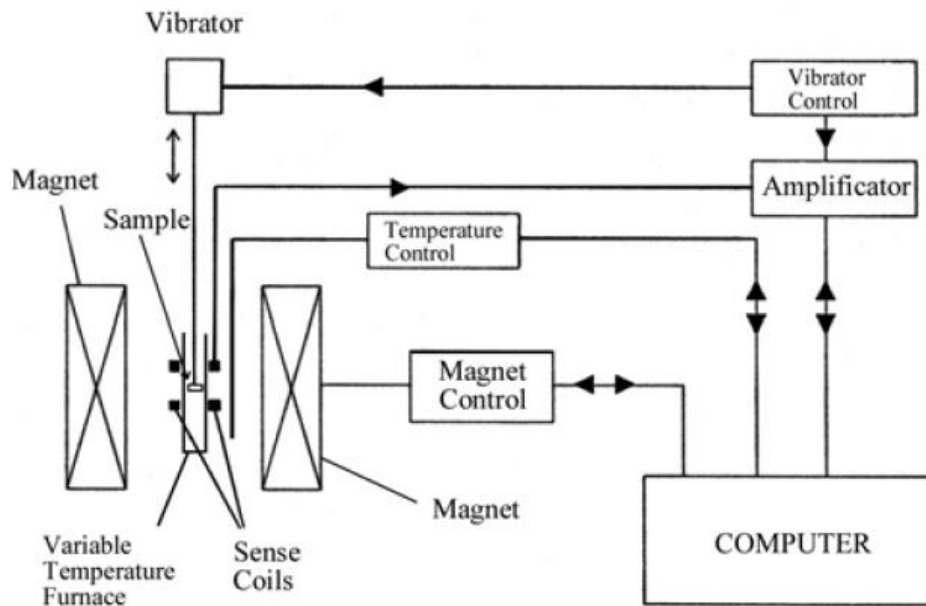
Fig. 2.8 Schematic diagram of the different components of the VSM.

2.9.2 Working conditions

Measurements were done on a Micro–Sense (LOT–Quantum Design) VSM (Fig. 2.9), located at the Gnm^3 group, with a maximum applied magnetic field of 2 T, which is generated by an electromagnet. The working temperature can be adjusted and controlled from 100 K to 1000 K. The sample is located at the end of a rigid holder which is oscillated in the vertical direction, perpendicular to the magnetic field.

The oscillation amplitude and frequency were of 1.5 mm and 67 Hz, respectively. To get optimum signal, the samples were previously centered in angle and height and, then, demagnetized using a sequence of alternating decreasing fields.
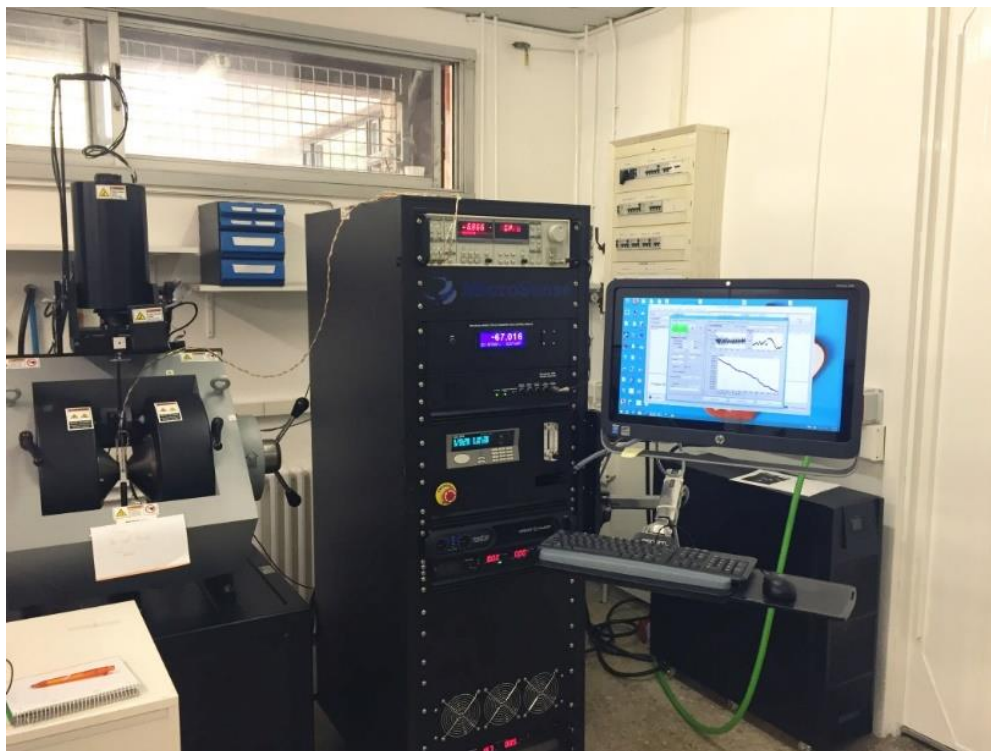
Fig. 2.9 Image of the Micro–Sense (LOT–Quantum Design) VSM.

2.9.3 The differences between VSM and SQUID

Briefly, VSM is a classical static magnetometry technique. The voltage signal of VSM measurement is induced in a pick–up loop by Faraday's law of induction between with and without the specimen. Because the sample is vibrated in its vicinity, the measurement can be performed relatively faster. In contrast, in a conventional SQUID magnetometer, the sample will be repeatedly transported across a superconducting pick–up loop and then the SQUID output the corresponding voltage as the response. Consequently, the testing time of SQUID will be longer. For comparison, SQUID can use higher magnetic fields, while higher temperatures can be reached in VSM. In addition, the sensitivity of SQUID is usually higher than that offered by VSM.

2.10 X–ray magnetic circular dichroism

2.10.1 Origin and fundamentals of the technique

X–ray magnetic circular dichroism (XMCD) is a difference spectrum of two X–ray absorption spectra (XAS), namely left and right circularly polarized light, both taken at a given magnetic field. By comparing the observed differences in the XMCD spectrum,

information like spin and orbital magnetic moments of a specific atom can be obtained (Fig. 2.10). This phenomenon was firstly predicted by J. L. Erskine & E. A. Stern in 1975.[37] Later, in 1987 Schütz *et. al* carried out their pioneering works in Fe atoms and thereby confirmed the theoretical prediction. This gave an enormous boost to both industrial applications and research to study magnetic properties.[38] Compared with other magnetic characterization techniques, XMCD possesses the advantage of elemental specificity. Due to the simple sum rules, XMCD can provide quantitative information about the electron spin distribution and orbital angular momenta. In addition, XMCD has the capacity to determine spin orientation, infer spin states and separate magnetic and non–magnetic components in heterogeneous samples.[39]
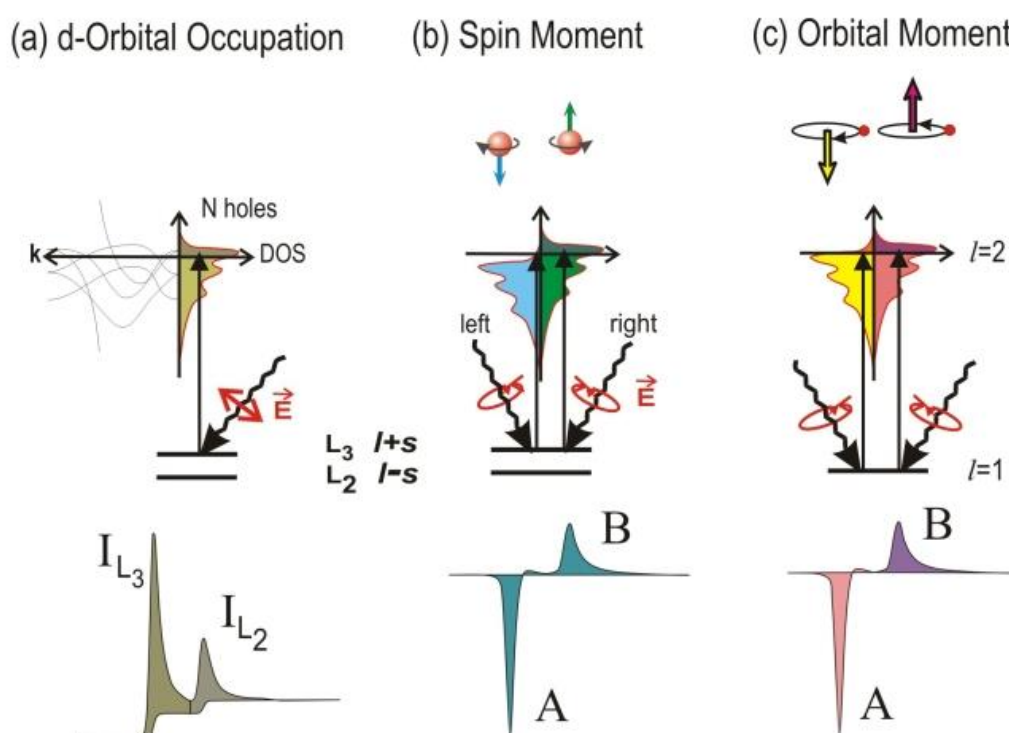
Fig. 2.10 Schematic illustration about the operating principle of XMCD. (a) Electronic transitions in conventional L–edge X–ray absorption, (b) XMCD spectrum caused by spin moment, (c) XMCD caused by orbital moment. Peaks A and B are the dichroic difference intensities according to a certain sum rule.[40]

2.10.2 Working conditions

All the measurements were taken at BESSY–II UE46_PGM–1 beamline (Helmholtz Zentrum, Berlin). For the powder samples, a bit of the sample was dispersed in ethanol and afterwards several drops were put on a gold film to form a thin layer. For the film samples,

a small piece of the film was cut off by diamond knife. X–ray absorption spectra (XAS) of Ni $L_{3,2}$ and Cu $L_{3,2}$ edge at right–handed (μ^+) and left–handed (μ^-) circularly polarized X–ray beam were recorded. The entire experimental procedure was operated under high vacuum condition. The signals of XAS were obtained at cryogenic (5 K) and room temperature (300 K) with an applied magnetic field of 5 T.

References

[1] Geffcken W, Berger E, Verfahren zur änderung des reflexionsvermögens optischer gläser. deutsches reichspatent, assigned to jenaer glaswerk schott & gen., Jena 1939, **736**, 411

[2] S. Siau, A. Vervaet, S. Degrande, E. Schacht and A. Van Calster, Dip coating of dielectric and solder mask epoxy polymer layers for build–up purposes, *Appl. Surf. Sci.*, 2005, **245**, 353–368.

[3] H. R. Barzegar, F. Nitze, T. Sharifi, M. Ramstedt, C. W. Tai, A. Malolepszy, L. Stobinski and T. Wågberg, Simple dip–coating process for the synthesis of small diameter single–walled carbon nanotubes–effect of catalyst composition and catalyst particle size on chirality and diameter, *J. Phys. Chem. C*, 2012, **116**, 12232–12239.

[4] S. Gong, W. Schwalb, Y. Wang, Y. Chen, Y. Tang, J. Si, B. Shirinzadeh and W. Cheng, A wearable and highly sensitive pressure sensor with ultrathin gold nanowires, *Nat. Commun.*, 2014, **5**, 3132.

[5] Asumi Giken, Limited. http://www.dip–coater.com/english/about_dip_coating.html

[6] Knoll M., Aufladepotentiel und sekundäremission elektronenbestrahlter körper, *Z. Tech. Phys.* 1935, **16**, 467–475

[7] Von Ardenne M., Das Elektronen–rastermikroskop. theoretische grundlagen., *Z. Tehc. Phys.* 1938, **109**, 553–572

[8] Von Ardenne M., Das Elektronen–rastermikroskop. praktische ausführung., *Z. Tehc. Phys.* 1938, **19**, 407–416

[9] J. I. Goldstein, D. E. Newbury, P. Echlin, D. C. Joy, C. E. Lyman, E. Lifshin, L. Sawyer and J. R. Michael, *Scanning Electron Microscopy And X–Ray Microanalysis*, New York: Springer US, 3rd edn., 2003.

[10] P. W. Hawkes, Ernst ruska, *Phys. Today*, 1990, **43**, 84–85.

[11] T. Palucka, Overview of electron microscopy, http://authors.library.caltech.edu/5456/1/hrst.mit.edu/hrs/materials/public/ElectronMicroscope/EM_HistOverview.htm

[12] J. Hillier and R. F. Baker, Microanalysis by means of electrons, *J. Appl. Phys.*, 1944, **15**, 663–675.

[13] R. F. Egerton, *Electron Energy–Loss Spectroscopy in the Electron Microscope*, Springer Dordrecht Heidelberg London New York, Third Edit., 2011.

[14] R. F. Egerton, Electron energy–loss spectroscopy in the TEM, *Reports Prog. Phys.*, 2009, **72**, 16502.

[15] H. Tan, S. Turner, E. Yücelen, J. Verbeeck and G. Van Tendeloo, 2D atomic mapping of oxidation states in transition metal oxides by scanning transmission electron microscopy and electron energy–loss spectroscopy, *Phys. Rev. Lett.*, 2011, **107**, 107602.

[16] Q. M. Ramasse, C. R. Seabourne, D.–M. Kepaptsoglou, R. Zan, U. Bangert and A. J. Scott, Proving the bonding and electronic structure of single atom dopants in graphene with electron energy loss spectroscopy, *Nano Lett.*, 2013, **13**, 4989–4995.

[17] What is EELS? http://www.eels.info/about/overview

[18] W. Friedrich, P. Knipping, M, von Laue, *Ann. Phys.* 1912, **41**, 971–988.

[19] W.L. Bragg, The diffraction of short electromagnetic waves by a crystal, *Proc. Camb. Phil. Soc.* 1912, **17** 43–57.

[20] C. Giannini, M. Ladisa, D. Altamura, D. Siliqi, T. Sibillano and L. De Caro, X–ray diffraction: A powerful technique for the multiple–length–scale structural analysis of nanomaterials, *Crystals*, 2016, **6**, 1–22.

[21] B.D. Cullity and S.R. Stock, *Elements of X–ray diffraction*, Pearson, 3rd edn., 2001.

[22] T. H. de Keijser, J. I. Langford, E. J. Mittemeijer and A. B. P. Vogels, Use of the Voigt function in a single–line method for the analysis of X–ray diffraction line broadening. *J. Appl. Crystallogr.*, 1982, **15**, 308–314.

[23] A. L. Patterson, The Scherrer formula for X–ray particle size determination, *Phys. Rev.*, 1939, **56**, 978–982.

[24] L. Lutterotti, S. Matthies and H.–R. Wenk, MAUD: a friendly Java program for material analysis using diffraction, *IUCr Newsl. CPD*, 1999, **21**, 14–15.

[25] Paul van der Heide, *X–Ray Photoelectron Spectroscopy; An Introduction to Principles and Practices*, John Wiley & Sons, Inc., 2012.

[26] S. Hofmann, *Auger– and X–Ray Photoelectron Spectroscopy in Materials Science: A User–Oriented Guide*, Springer Dordrecht Heidelberg London New York, 2013.

[27] Physical Electronics, https://www.phi.com/surface–analysis–techniques/xps–esca.html.

[28] H. Gabasch, E. Kleimenov, D. Teschner, S. Zafeiratos, A. Knop–gericke, D. Zemlyanov, B. Aszalos–kiss and K. Hayek, Carbon incorporation during ethene oxidation on Pd (111) studied by in situ X–ray photoelectron spectroscopy at 2×10^{-3} mbar, *J. Catal.*, 2006, **242**, 340–348.

[29] J. F. Moulder, W. F. Stickle, P. E. Sobol and K. D. Bomben, *Handbook of X–ray Photoelectron Spectroscopy*, Perkin–Elmer Corporation, Physical Electronics Division, 1992.

[30] D. Drung, C. Aßmann, J. Beyer, A. Kirste, M. Peters, F. Ruede and T. Schurig, Highly sensitive and easy–to–use SQUID sensors, *IEEE Trans. Appl. Supercond.*, 2007, **17**, 699–704.

[31] R. C. Jaklevic, J. Lambe, A. H. Silver and J. E. Mercereau, Quantum interference effects in Josephson tunneling, *Phys. Rev. Lett.*, 1964, **12**, 159–160.

[32] P. W. Anderson and J. M. Rowell, Probable observation of the Josephson superconducting tunneling effect, *Phys. Rev. Lett.*, 1963, **10**, 230–232.

[33] B. D. Josephson, The discovery of tunnelling supercurrents, *Rev. Mod. Phys.*, 1974, **46**, 251–254.

[34] A. Barone and G. Paterno, *Physics and Applications of the Josephson Effect*, John Wiley & Sons, 1982.

[35] S. Foner, *Rev. Sci. Instrum.*, Versatile and sensitive vibration–sample magnetometer, 1959, **30**, 548–557.

[36] J. R. Reitz, F. J. Milford and Robert W. Christy, *Foundations of electromagnetic theory*, Addison–Wesley Publishing Company, 2009.

[37] J. L. Erskine and E. A. Stern, Calculation of the M_{23} magneto–optical absorption spectrum of ferromagnetic nickel *Phys. Rev. B*, 1975, **12**, 5016–5024.

[38] G. Schütz, W. Wagner, W. Wilhelm, P. Kienle, R. Zeller, R. Frahm and G. Materlik, Absorption of circularly polarized x rays in iron, *Phys. Rev. Lett.*, 1987, **58**, 737–740.

[39] T. Funk, A. Deb, S. J. George, H. Wang, S. P. Cramer, Coord. Chem. Rev. 2005, **249**, 3–30.

[40] Magnetic dichroism spectroscopy and microscopy, Stanford, https://www–ssrl.slac.stanford.edu/stohr/xmcd.htm
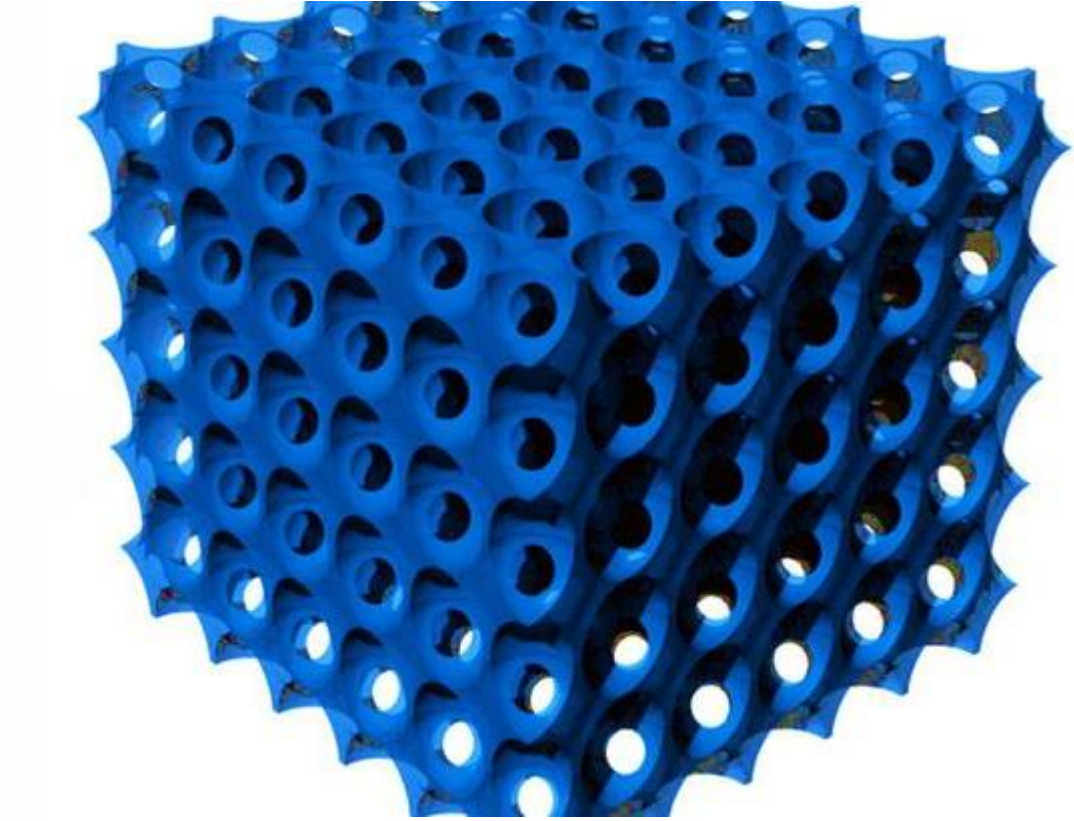
3. Results and discussion

This chapter gathers the results and discussion stemming from the synthesis and magnetic characterization of transition metal–doped SnO_2 powders and films.

3.1 Nanocasting synthesis of mesoporous SnO$_2$ with a tunable ferromagnetic response through Ni loading

In this section, the preparation of magnetically active mesoporous Ni–doped SnO$_2$ powders by means of nanocasting from KIT–6 silica is presented. Notably, only Ag and Pd have been used as dopants in mesoporous SnO$_2$, and, as aforementioned, mostly for the purpose to improve its gas–sensing capabilities. Here, the magnetic properties of the synthesized mesopowders are investigated at 10 K and 300 K by SQUID magnetometry.

3.1.1 Morphology and crystallographic structure

Prior to the synthesis of the SnO$_2$–based replicas, the morphology of KIT–6 silica template was examined. A representative TEM image of the bicontinuous cubic SiO$_2$ matrix is shown in Fig. 3.1.1. The quality of the template was judged as acceptable and pore size was estimated to be around 10 nm. The morphology of the derived SnO$_2$–based powders is depicted in Fig. 3.1.2. Both SEM (Fig. 3.1.2 (a)–(d)) and TEM (Fig. 3.1.2 (e)–(h)) images indicated that the powders exhibit an ordered arrangement of mesopores irrespective of the Ni doping. Indeed, the level of doping did not seemingly have a deleterious impact on the mesostructure of the SnO$_2$ replica. Relatively large ordered mesoporous domains were visible at the surface of the mesoporous particles by SEM.
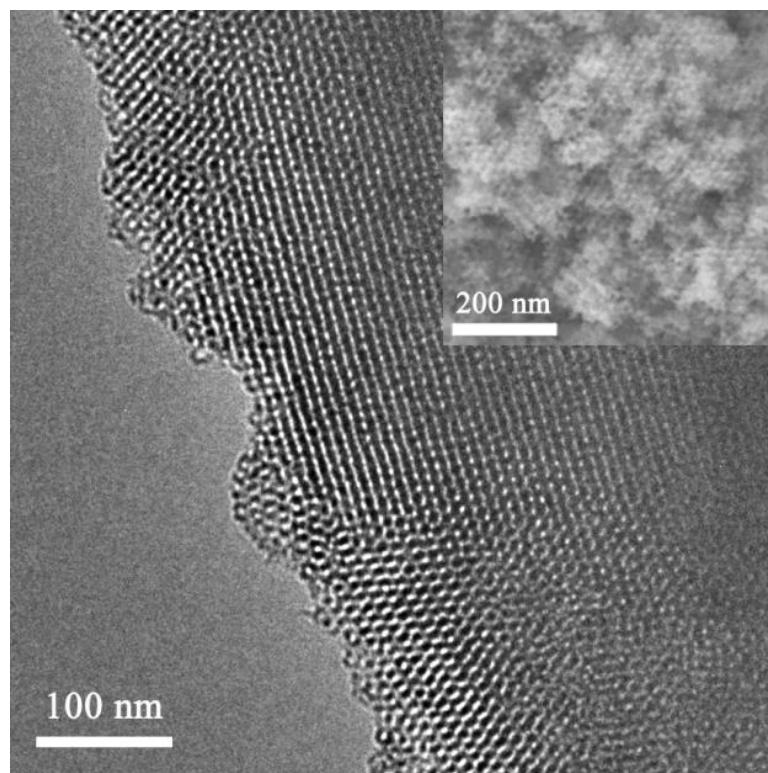
Fig. 3.1.1 TEM image of KIT–6 silica template. The inset shows an SEM image.
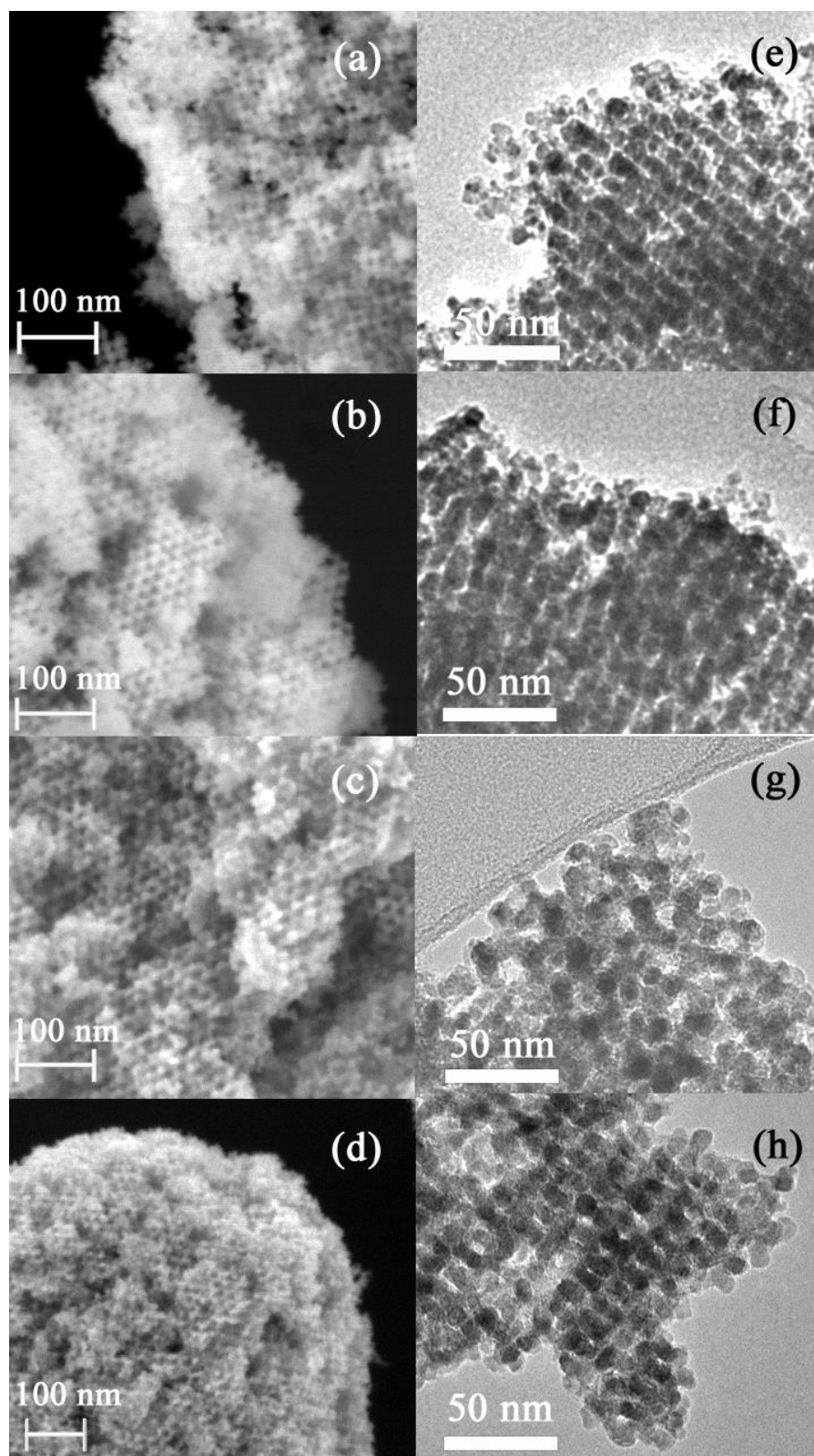
Fig. 3.1.2 Morphology of undoped and Ni–doped SnO$_2$ after KIT–6 silica template removal, (a) and (e), (b) and (f), (c) and (g), and (d) and (h) are the SEM and TEM images, respectively, of the powders obtained from different [Ni(II)]/[Sn(II)] molar ratios (0:100, 5:95, 15:85 and 20:80, respectively).

Representative EDX patterns are shown for undoped and Ni–doped SnO_2 in Fig. 3.1.3 (a) and (b), respectively. The amounts of Ni and Si for all samples are listed in Table 3.1.1. For the doped powders, it was clear that Ni was successfully doped into the SnO_2 matrix. The highest deviation (ca. 2 at.%) between the nominal and actual Ni percentage was found for the sample with the highest dopant amount. Nevertheless, considering that the error in EDX measurements is about 1 at.%, this is not a significant difference. Residual silicon content was kept below 4 at.% in all cases. Probably the formation of strong Si–O–Sn bonds precludes a complete removal of the silica host, compared to other transition metal oxides. Si and Sn belong to IV–group elements; they possess the same number of outermost electrons and, in turn, similar chemical properties. In fact, SnO_2/SiO_2 composites can be simply obtained by solid–vapour reaction of mesoporous silica with tin vapour at 700 ºC.[1] In this work, authors detected Sn^{4+} bonded to the silica wall by bridged oxygen atoms.
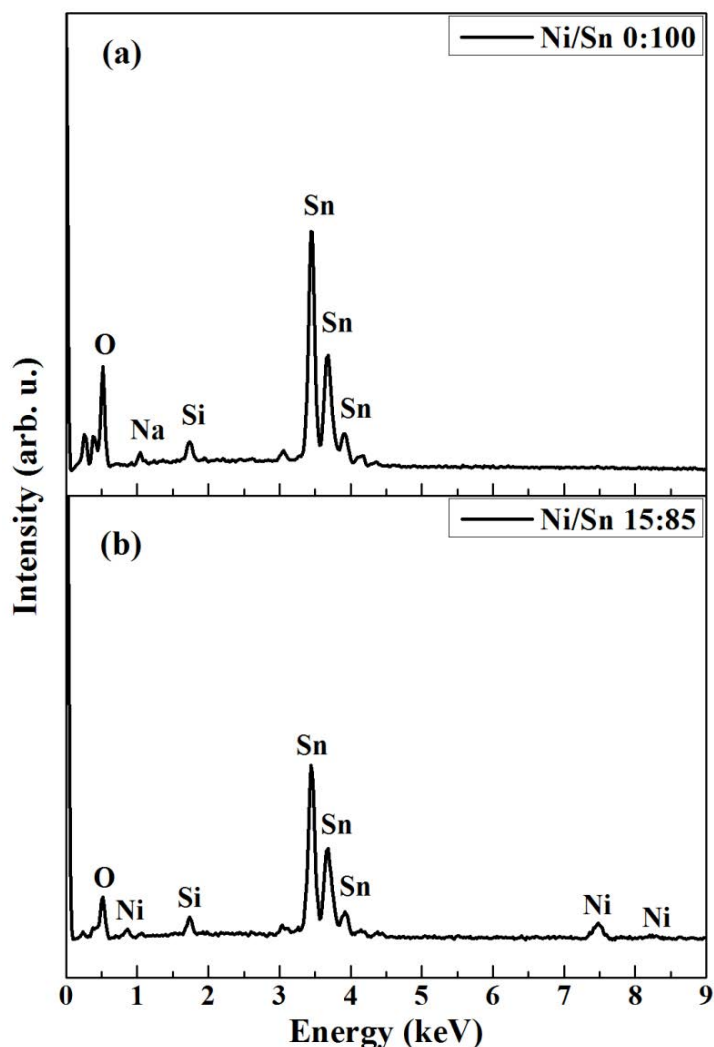
Fig. 3.1.3 EDX patterns of (a) undoped and (b) Ni–doped mesoporous SnO_2 obtained from [Ni(II)]/[Sn(II)] molar ratio of 15:85.

[Ni(II)]/[Sn(II)]	Ni nominal content (at.%)	Ni determined by EDX (at.%)	Si determined by EDX (at.%)	Crystallite size SnO_2 phase (nm) (± 0.5)	Microstrains of SnO_2 phase ($\pm 1\cdot 10^{-5}$)	a (Å) of SnO_2 phase ($\pm 1\cdot 10^{-4}$)	c (Å) of SnO_2 phase ($\pm 1\cdot 10^{-4}$)
0:100	0	0	2	8.5	$1.8\cdot 10^{-4}$	4.7385	3.1885
5:95	2	1	4	8.1	$3.5\cdot 10^{-3}$	4.7397	3.1875
15:85	5	6	3	9.2	$3.4\cdot 10^{-3}$	4.7428	3.1854
20:80	7	9	3	10.6	$3.7\cdot 10^{-3}$	4.7416	3.1846

Table 3.1.1 [Ni(II)]/[Sn(II)] molar ratio used in the synthesis, nominal Ni content in the resulting powers, corresponding actual percentages of Ni and Si detected by EDX, and crystallite size, microstrains and cell parameters of the SnO_2 phase.

Nevertheless, the residual silicon amounts can be regarded as fairly low. This was possible through two consecutive cleaning steps of the $SiO_2@SnO_2$ composites with large volumes of NaOH solution to etch the silica template. Besides the formation of Si–O–Sn bonds, the presence of numerous nanochannels in the interior of the mesoporous particles likely hampers the effective dissolution of the silica host as the etching solution has to reach their inner space. Complementary XPS analyses indicated that although Si was present in all samples, its content was much lower than that determined by EDX. According to XPS analyses, the highest Si amount detected in the powders was 0.7 at.%. Since XPS is a surface–sensitive technique, the detection of a larger amount of Si by EDX indeed suggests that the residual silicon is mainly concentrated in the inner cavities of the SnO_2 particles.

As shown in Fig. 3.1.4, all the samples are nanocrystalline. The main peak positions of the undoped and Ni–doped SnO_2 samples correspond to the rutile type tetragonal structure (JCPDS card No. 88–0287). No extra peaks are observed except for the sample produced from [Ni(II)]/[Sn(II)] of 20:80. In this case, additional diffraction peaks attributed to NiO are observed, which match those of JCPDS card No. 47–1049. Notice that these peaks are much narrower since a few big NiO particles had grown outside the mesoporous SnO_2 particles, as observed by TEM (not shown). Chaudhary and co–workers detected the formation of NiO in nanocrystalline thick SnO_2 films with Ni contents beyond 5 at.%,[2] which is in agreement with our findings. The crystallite size of the SnO_2 phase, together with the microstrains and cell parameters, were calculated using MAUD. The calculated values are listed in Table 3.1.1.
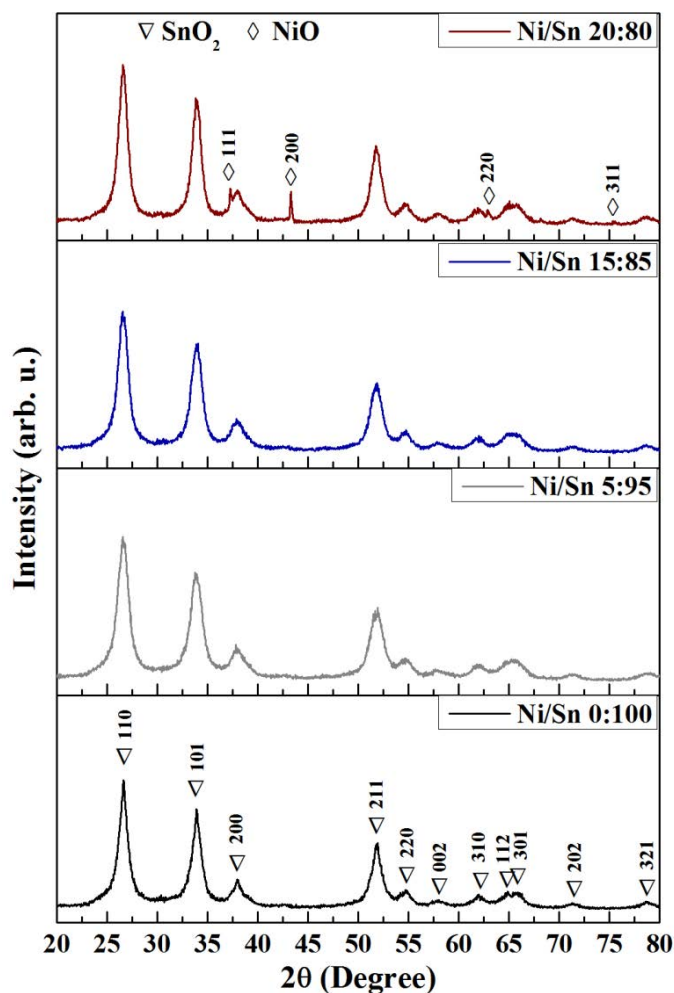
Fig. 3.1.4 XRD patterns of undoped and Ni–doped mesoporous SnO_2 obtained from varying [Ni(II)]/[Sn(II)] molar ratios.

In broader strokes, both crystallite size and microstrains increased with the Ni doping although not in a monotonous manner. Crystallite size slightly decreased for the sample with the lowest Ni amount but increased thereafter. The level of microstrains rose significantly when SnO_2 was doped with 6 at.% and then remained fairly constant for higher doping amount. The 'a' and 'c' lattice parameters increased and decreased, respectively, with the Ni doping level, in agreement with other works.[3] Fig. 3.1.5 (a) is a HR–TEM image of the 6 at.%–doped SnO_2 powder. The SnO_2 skeleton consists of nanocrystals of about 5 nm in diameter, in agreement with XRD and other works in the literature.[4] The fast Fourier transform (FFT) of selected regions in the image shows spots whose interplanar distance matches tetragonal SnO_2. Selected area electron diffraction (SAED) analyses of the sample doped with higher Ni amount (9 at.%) showed spots attributed to the NiO phase (Fig. 3.1.5(b)). In such a case, only the electron diffraction coming out from mesoporous particles was captured, avoiding the response of any big NiO crystal nearby.
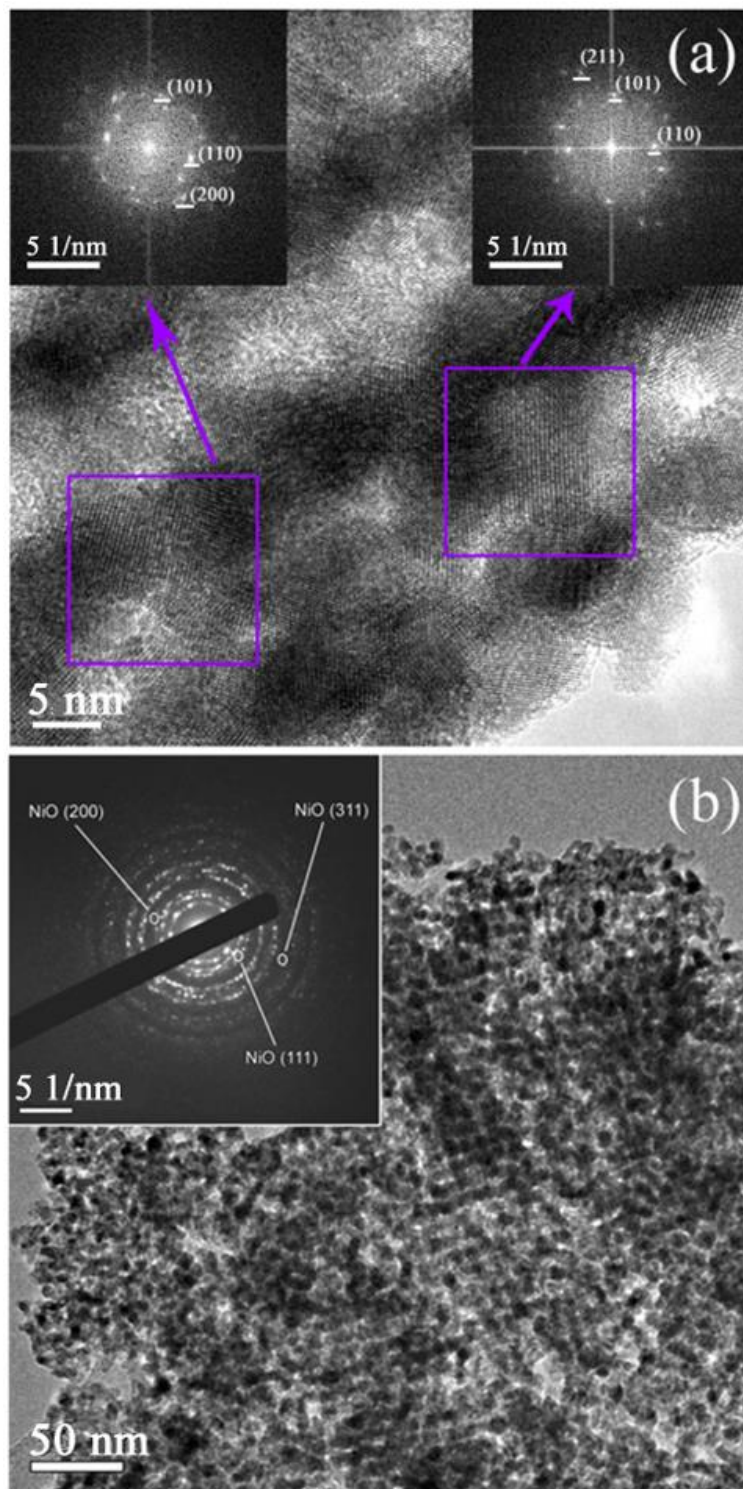
Fig. 3.1.5 (a) HR–TEM image of the Ni–doped mesoporous SnO_2 powder synthesized from [Ni(II)]/[Sn(II)] molar ratio of 15:85. The insets show the FFT of the regions enclosed in the purple boxes. Underlined in white, some spots of the rutile–type tetragonal SnO_2 are indicated, along with the Miller indices of the corresponding crystallographic planes. (b) TEM image of the powder synthesized from [Ni(II)]/[Sn(II)] molar ratio of 20:80. The selected area electron diffraction pattern is shown in the inset. Circled spots can be unambiguously assigned to NiO phase.

In order to confirm the mesoporous long–range order of the samples, low–angle XRD analysis was carried out. Fig. 3.1.6 shows representative patterns of mesoporous KIT–6 silica, undoped SnO_2 and 6 at.% Ni–doped SnO_2. The KIT–6 silica shows two well–resolved reflections attributable to (211) and (220) reflections. However, different from previous works,[5,6] the intensity of (211) peak is weaker than (220). After replication, the peaks become inconspicuous, suggesting a partial loss of the long–range mesoporous order and concomitant decrease of the size of the ordered domains.
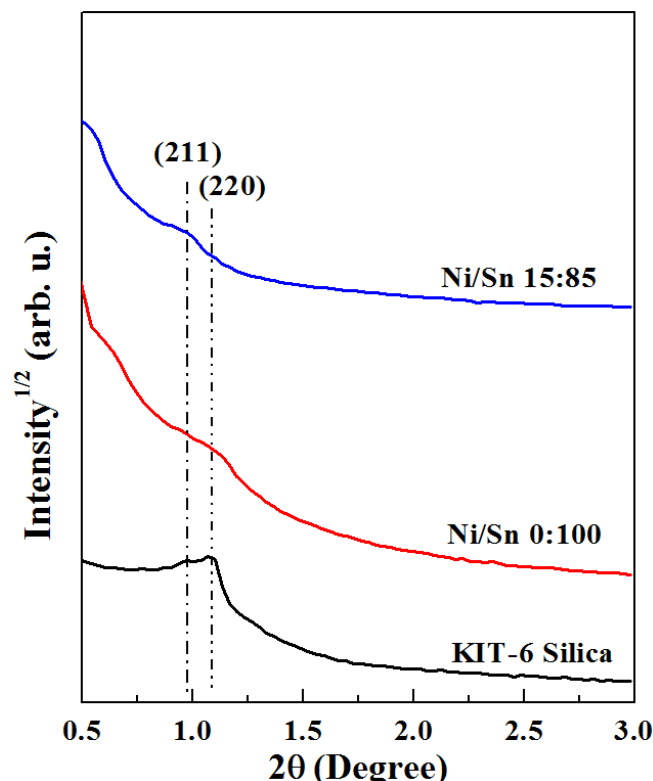
Fig. 3.1.6 Low–angle XRD patterns corresponding to KIT–6 silica template and mesoporous replicas obtained from [Ni(II)]/[Sn(II)] molar ratio 0:100 and 15:85.

3.1.2 XPS analysis

The samples with 6 and 9 at.% Ni were subjected to XPS characterization to determine the oxidation state and the local chemical environment of the Ni element. At the same time, the effects induced by Ni to the SnO_2 matrix were investigated. Undoped SnO_2 was taken as the reference sample. Fig. 3.1.7 (a) shows the XPS survey spectrum of the sample with 6 at.% Ni. Sn 3d high–resolution XPS spectra are displayed in Fig. 3.1.7 (b). Upon Ni doping, Sn 3d peaks shift toward lower binding energy compared with undoped SnO_2. It is conjectured that a larger number of oxygen vacancies and dangling bonds arise in the SnO_2 skeleton due to the introduction of Ni.[7] Thus, the relative number of electrons in the external electronic shell of Sn increases, which in turn causes a decrease of the binding energy of Sn compared to the undoped case.
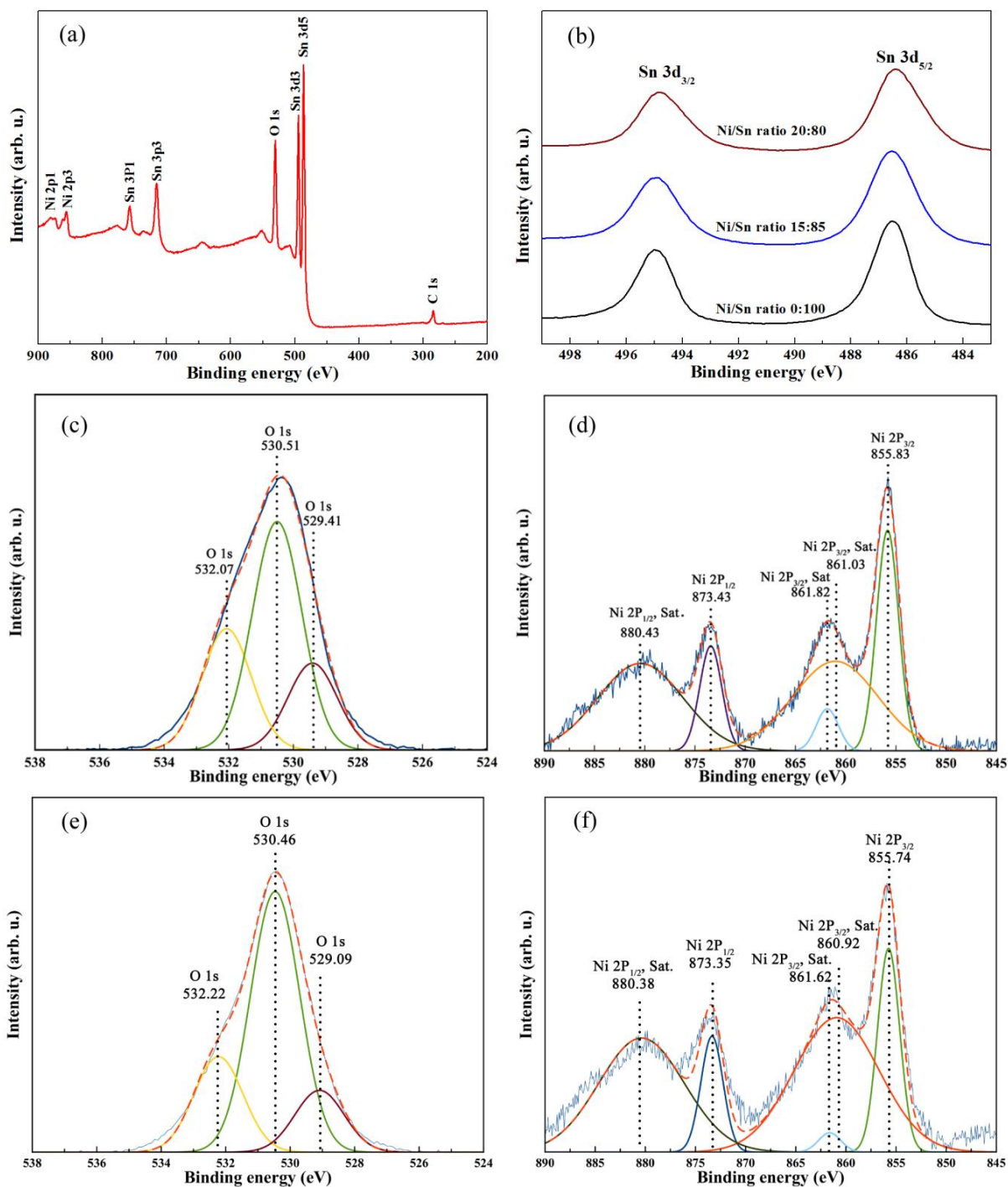
Fig. 3.1.7 (a) XPS survey spectrum of the powder obtained from [Ni(II)]/[Sn(II)] molar ratio of 15:85 (6 at.% Ni). High–resolution (b) Sn 3d for 15:85 (6 at.% Ni) and 20:80 (9 at.% Ni); (c) and (e) O 1s, and (d) and (f) Ni 2p for 15:85 (6 at.% Ni) and 20:80 (9 at.% Ni), respectively. In (b) the core–level Sn 3d spectrum of undoped SnO_2 is shown for comparison. 'Sat.' denotes satellite peaks.

The O 1s and Ni 2p XPS spectral windows of 6 at.% Ni–doped SnO_2 are shown in Fig. 3.1.7 (c) and (d), respectively. The O 1s spectrum can be deconvoluted into three main bands. The peaks at 530.51 eV and 529.41 eV correspond to the O 1s core level of the O^{2-}

anions in the SnO_2 and NiO, respectively.[8,9,10] The peak at 532.07 eV is possibly attributed to chemisorbed oxygen at the defect sites of oxide crystal or hydroxyl groups.[10,11]

In Fig. 3.1.7 (d), the separation distance between the peaks at 855.83 eV and 873.43 eV, which matches the binding energies expected for Ni $2p_{3/2}$ and Ni $2p_{1/2}$, is 17.60 eV. This difference is broader than the binding energy difference for metallic nickel, which is around 17.30 eV.[12] Furthermore, the position of the peaks exhibits some shift to higher binding energy compared with Ni^0.[13,14] This result excludes the occurrence of metallic Ni clusters in the 6 at.% Ni–doped SnO_2. Based on the analysis, Ni ions possess a chemical valence of 2+. Experimental binding energies for Sn and O also indicate that their valences are 4+ and 2–, respectively. The O 1s and Ni 2p spectra for the sample with 9 at.% Ni is very similar to that of 6 at.% Ni (Fig. 3.1.7(e) and (f)), so the same reasoning applies.

3.1.3 EELS characterization

Taking into account the results previously obtained, the powder with 6 at.% Ni (for which NiO phase was not detected in the XRD pattern but XPS data indicated it was definitely present) and that with 9 at.% Ni (for which NiO as a secondary phase was clearly detected by XRD) were selected for EELS characterization. The goal was to investigate the spatial distribution of Ni in order to get further insight into the structural and magnetic characteristics of these two opposed samples. Fig. 3.1.8 shows the STEM and corresponding EELS mapping of a selected region for both cases. For the sample with the lower Ni content, Ni is detected mostly near the pore edges forming a kind of nanocoating, although red colored pixels superimposed to the green background are also observed at the inner region of the pore walls. For the sample with 9 at.% Ni, a larger amount of Ni concentrated at the pore region was seemingly found. Orange coloured pixels result from the mixing of red (Ni) and green (O) colors. Nevertheless, the presence of big NiO particles outside the mesoporous particles should not be omitted in this case. When the amount of Ni largely exceeds the solubility limit, part of it can form the NiO skin around the pores but another fraction cannot be hosted and forms separate crystals outside. Although the coating surrounding the pores looks redder in the sample with 6 at.% Ni, this does not mean it is made of metallic Ni. The pixels are not 100% red and indeed the L_3/L_2 ratio calculated from the EELS spectra taken at this region gives a value of 2.8 (see Fig. 3.1.9), hence closer to NiO (for which the ratio is 3) than metallic Ni (for which the ratio is 1.5). This agrees with XPS analyses and, in fact, it makes sense considering that the conversion of precursors was carried out by heat–treatment in air.
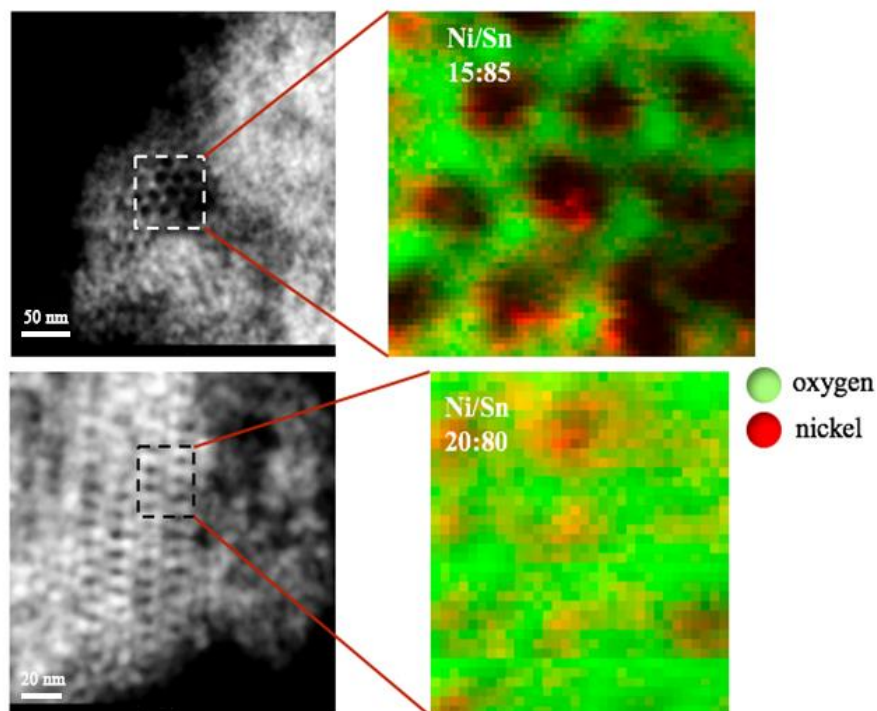
Fig. 3.1.8 STEM images and corresponding EELS mapping of the regions enclosed in the dashed squares for Ni–doped powders obtained from varying [Ni(II)]/[Sn(II)] molar ratios. Oxygen is in green while Ni is in red.
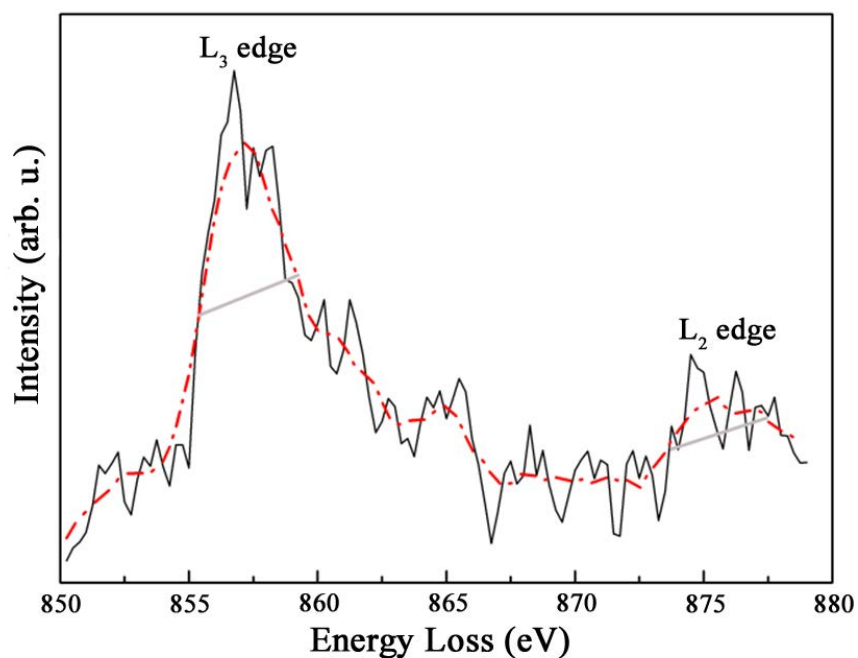
Fig. 3.1.9 Representative single Ni $L_{2,3}$ spectrum extracted from a spectrum image (raw data and splined fit) for the sample with 6 at.% Ni. Spectrum was taken on the coating surrounding the SnO_2 pores. The integrated intensity ratio of L_3 and L_2 ionization edges gives a value of 2.8.

90

In any case, the fact that NiO tends to accumulate at the pore/air interface makes the nanocasting route appealing toward ordered mesoporous nanocomposites. Actually, partial coating of mesoporous oxides has been reported in recent years by using successive impregnation and calcination procedures with different precursors. [15] Here, oxide semiconductor (SnO_2)/antiferromagnetic (NiO) nanocomposites are obtained in–situ in one–step nanocasting process.

3.1.4 Magnetic properties of Ni–doped SnO_2 powders

The magnetic properties of the samples with varying Ni concentration were studied by acquiring hysteresis loops at 10 K and 300 K. The undoped SnO_2 exhibits inconspicuous paramagnetic behaviour at 10 K and typical diamagnetic behaviour at 300 K (Fig. 3.1.10).
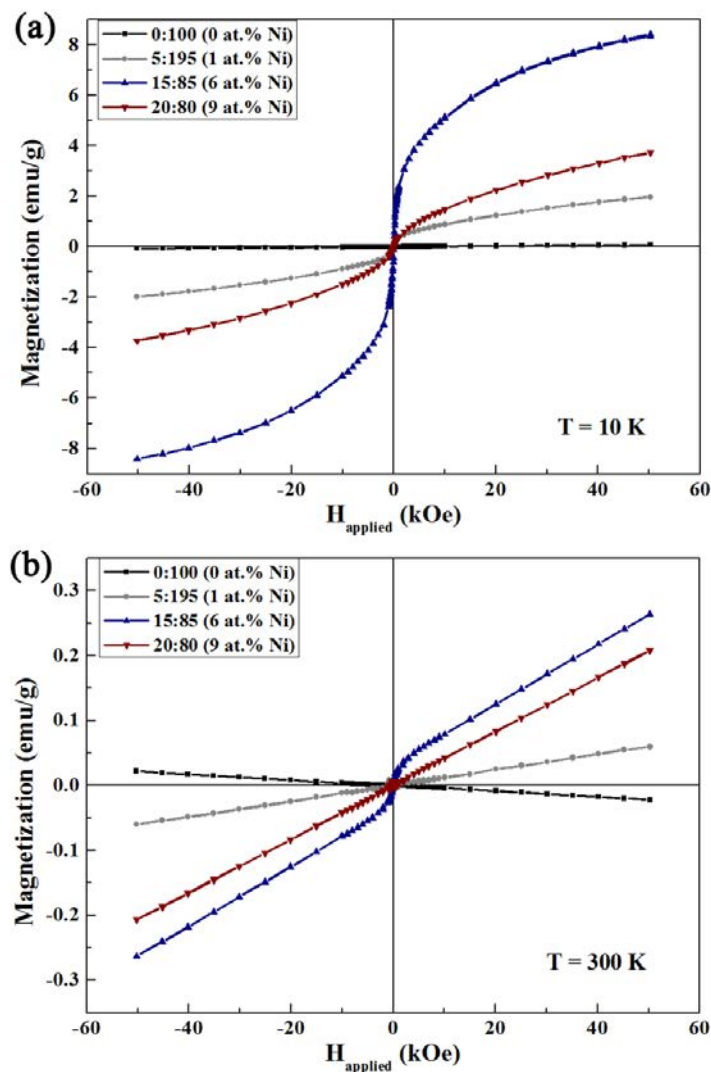
Fig. 3.1.10 Magnetic hysteresis loops of mesoporous undoped and Ni–doped SnO_2 powders obtained from varying [Ni(II)]/[Sn(II)] molar ratios (the corresponding experimental Ni percentages are in parentheses).

Meanwhile, the Ni–doped samples show a clear ferromagnetic signal at both temperatures although the saturation magnetization (M_s) does not scale with the Ni amount. The sample with 6 at.% Ni possesses the largest M_s both at 10 K (5.88 emu/g) and 300 K (0.05 emu/g). A reduction of the M_s values is observed for the sample with 9 at.% Ni. The ferromagnetic response observed in the Ni–containing powders is likely due to two contributions: (i) doping with the transition metal and concomitant formation of oxygen vacancies,[16] and (ii) uncompensated spins at the surface of the NiO nanocoating.[17,18] Notice that NiO is an antiferromagnet in bulk form, with a Néel temperature of 520 K.[19,20] However, it has been described that when the size of NiO decreases so that it falls well in the nanosize domain (e.g. nanoparticles), it might exhibit a ferromagnetic signal due to the presence of uncompensated spins at their surface. This would explain why M_s is higher in the sample with 6 at.% than for 9 at.% Ni. For the former, a larger amount of uncompensated spins is expected from the very thin layer surrounding the SnO_2 pores. Meanwhile, for the latter, as the size of the NiO nanoparticles/nanoclusters has increased, the number of uncompensated spins decreases and so does the corresponding M_s.

3.1.5 Chapter summary

To summarize, in this section it was shown that ordered mesoporous Ni–doped SnO_2 powders with tunable room–temperature ferromagnetic response can be synthesized by hard–templating. The optimum [Ni(II)]/[Sn(II)] molar ratio to guarantee the formation of a fully mesoporous product with the highest M_s is 15:85. This corresponds to a Ni content of 6 at.%. At larger [Ni(II)]/[Sn(II)] molar ratio, the growth of a few NiO crytals outside the mesoporous structure could not be avoided. XRD analyses revealed that all samples possess the SnO_2 rutile structure irrespective of the Ni amount. Meanwhile, 2+ was the oxidation state of Ni, according to XPS data. Although dissolution of Ni ions in the SnO_2 lattice was proved by XRD, EELS analyses indicated that part of the dopant ions tended to accumulate at the pore edges. Hence, the observed room–temperature ferromagnetic response is attributed to both the Ni doping and the concomitant formation of oxygen vacancies, and to the occurrence of uncompensated spins at the surface of the NiO nanocoating. Ordered mesoporous semiconductor/antiferromagnetic nanocomposites can thus be obtained through one–step nanocating process by carefully controlling the doping level.

3.2 Evaporation–induced self–assembly synthesis of Ni–doped mesoporous SnO₂ thin films with tunable room temperature magnetic properties

In this section, the preparation of magnetically active mesoporous Ni–doped SnO_2 thin films by means of dip–coating and EISA is presented. The aim was to prove whether Ni–doped SnO_2 could be fabricated not only as mesoporous powders, but also as high–quality mesoporous films following a bottom–up strategy. As for the powders, the amount of Ni incorporated in the film was controllably varied from the amount of salt precursors ($SnCl_4$ and $NiCl_2$) during the synthesis step. In particular, the [Ni(II)]/[Sn(IV)] molar ratio was varied as follows: 0:100, 5:95, 10:90, 15:85 and 20:80. The triblock copolymer P–123 was utilized as structure directing agent.

3.2.1 Morphological and structural characterization

The surface morphology of the Ni–doped SnO_2 films was investigated by SEM. Fig. 3.2.1 indicates that the films are not fully–dense but, instead, they exhibit a mesoporous morphology. Tiny pores are homogeneously distributed on the whole surface of the samples, irrespective of the [Ni(II)]/[Sn(IV)] molar ratio used in the synthesis.
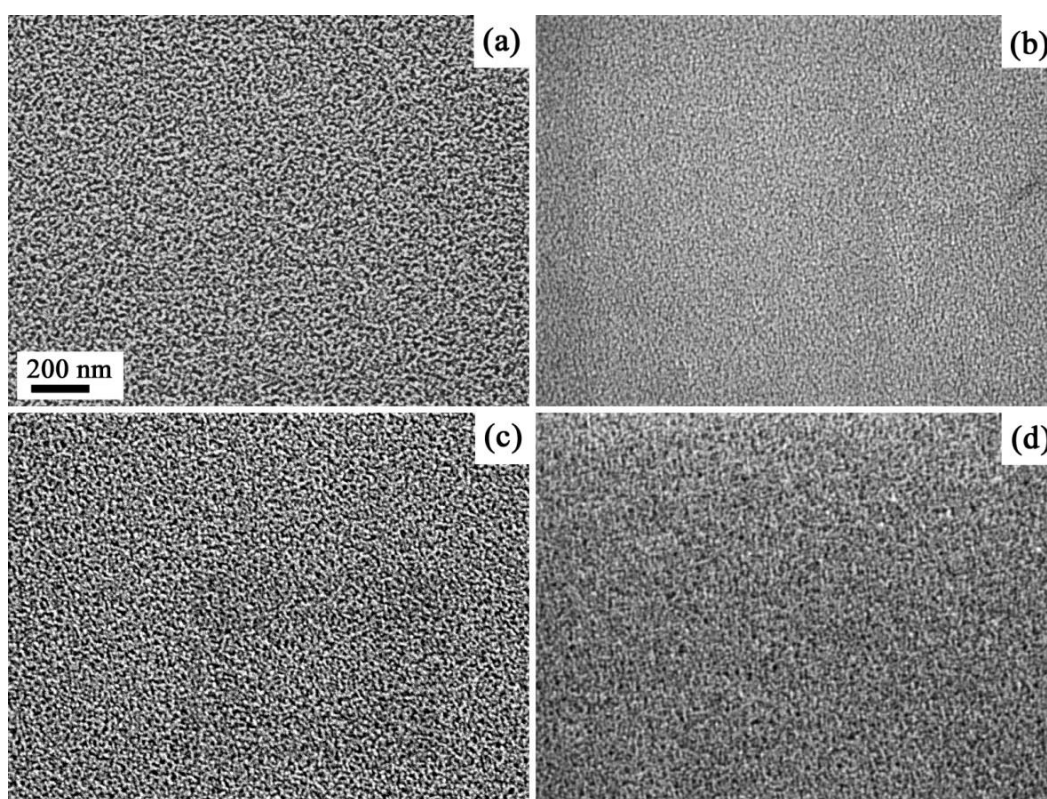
Fig. 3.2.1 On–top SEM images of Ni–doped SnO_2 mesoporous films synthesized from variable [Ni(II)]/[Sn(IV)] molar ratios: (a) 5:95, (b) 10:90, (c) 15:85 and (d) 20:80. The scale bar is the same for all images.

When compared with undoped SnO_2 films (Fig. 3.2.2), the incorporation of Ni does not seemingly cause any relevant morphological change. Namely, both undoped and Ni–doped films exhibit nanosized worm–like channels throughout the surface and, importantly, they are very flat and crack–free.
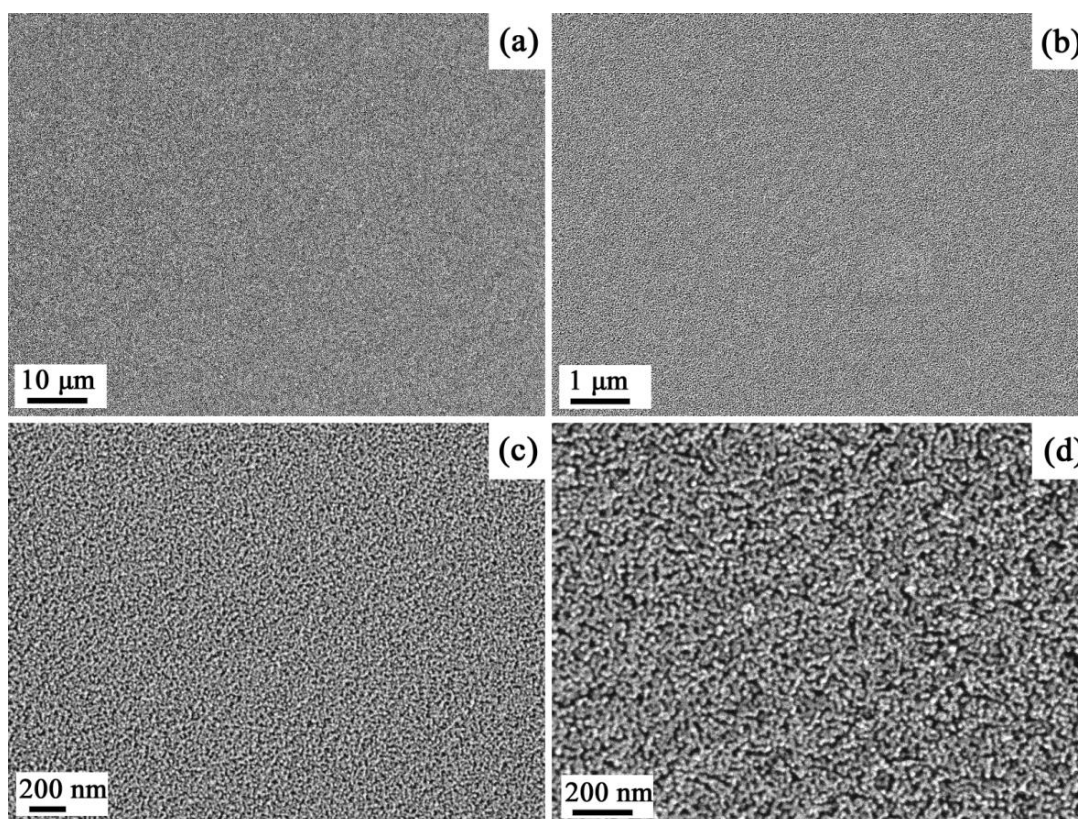
Fig. 3.2.2 SEM images of pure SnO_2 mesoporous films at different magnifications.

[Ni(II)]/[Sn(IV)]	Actual Ni content (from XPS) (at.%)	Crystallite size of SnO_2 phase (nm) (± 0.8)	Microstrains of SnO_2 phase (± $3 \cdot 10^{-5}$)	a (Å) of SnO_2 phase (± $2 \cdot 10^{-3}$)	c (Å) of SnO_2 phase (± $2 \cdot 10^{-3}$)
0:100	0.0	9.7	$1.1 \cdot 10^{-4}$	4.726	3.182
5:95	1.9	6.2	$2.6 \cdot 10^{-3}$	4.729	3.187
10:90	4.8	6.4	$5.1 \cdot 10^{-3}$	4.731	3.184
15:85	5.1	7.4	$5.3 \cdot 10^{-3}$	4.721	3.178
20:80	8.6	7.5	$4.5 \cdot 10^{-3}$	4.736	3.183

Table 3.2.1 Crystallite size, microstrains and cell parameters of the SnO_2 phase in the undoped and Ni–doped SnO_2 films as a function of the [Ni(II)]/[Sn(IV)] molar ration used the synthesis.

Low–magnification cross–section SEM images (Fig. 3.2.3) show that pores span the whole film thickness (which is in the range of 100–150 nm, as indicated in the figure). Table 3.2.1 lists the Ni content in the films as determined by XPS analyses. As expected, the amount of Ni increases with the [Ni(II)]/[Sn(IV)] ratio, from 0.0 to 8.6 at.%.
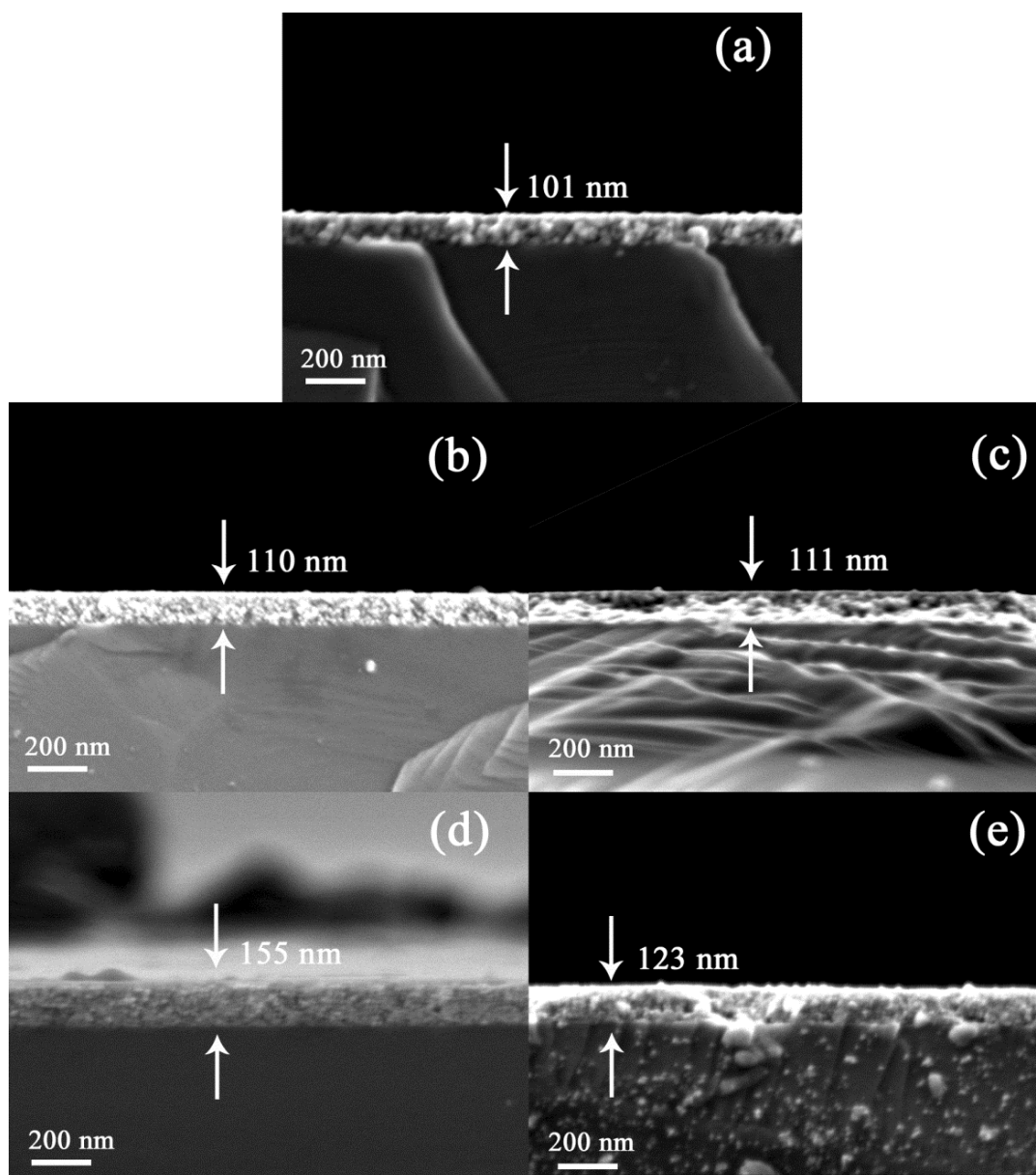
Fig. 3.2.3 Cross–section SEM images corresponding to undoped and Ni–doped SnO_2 films synthesized from variable [Ni(II)]/[Sn(IV)] molar ratios: (a) 0:100, (b) 5:95, (c) 10:90, (d) 15:85 and (e) 20:80.

Grazing incidence XRD patterns reveal that the pore walls are nanocrystalline (Fig. 3.2.4). The main peak positions of the undoped and Ni–doped SnO_2 samples correspond to the rutile–type tetragonal structure of SnO_2 (JCPDS card No. 88–0287). Additional diffraction

peaks indicated by arrows in Fig. 3.2.4 match the positions of SnO (JCPDS card No. 72–1012) and Sn_3O_4 (JCPDS card No. 16–0737).
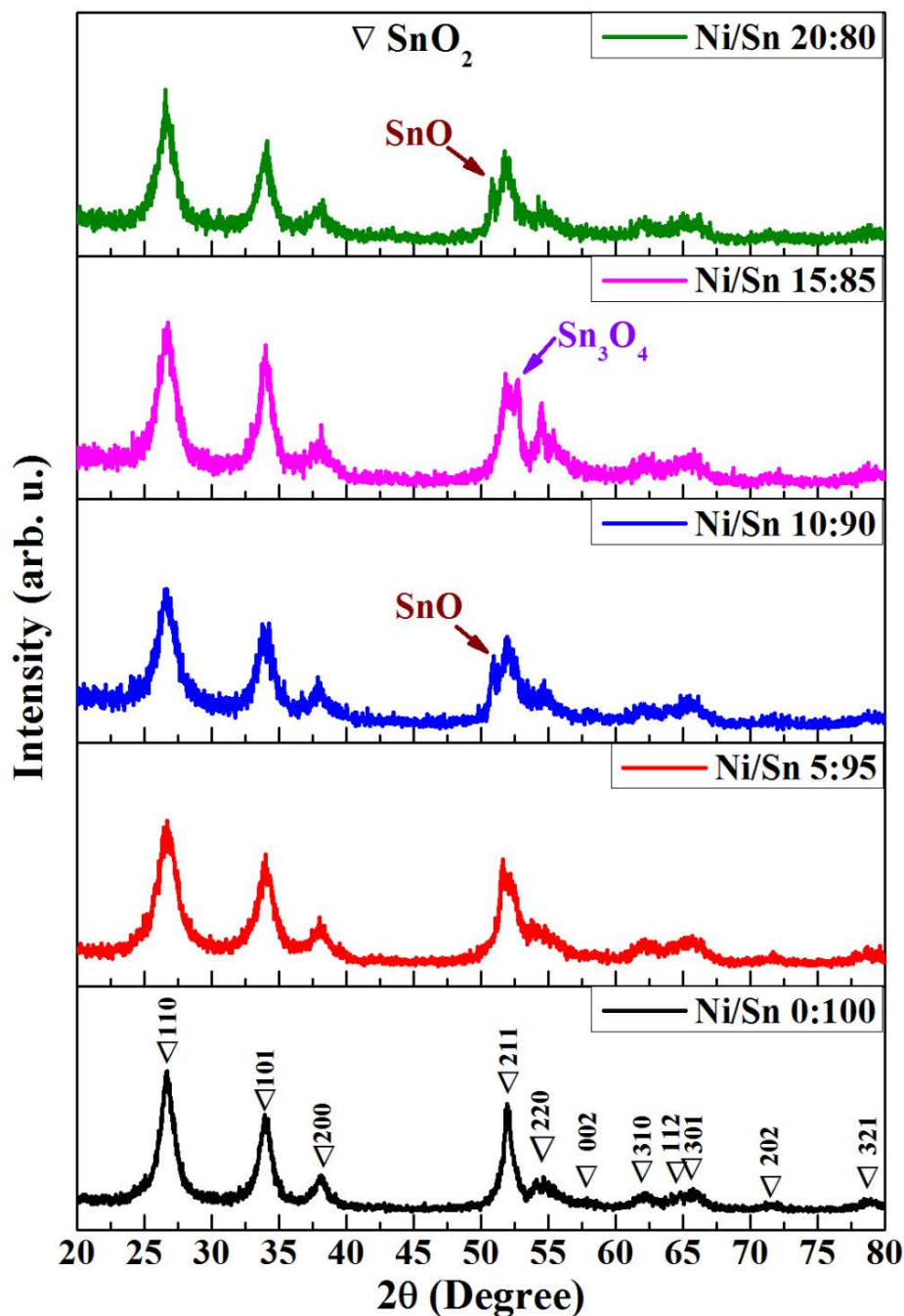
Fig. 3.2.4 Grazing incidence XRD patterns of mesoporous undoped and Ni–doped SnO_2 films synthesized from varying [Ni(II)]/[Sn(IV)] molar ratios.

It has been reported that the formation of SnO, SnO_2 and Sn_3O_4 is both oxygen– and temperature–dependent during heat treatment.[21] In our work, however, the temperature was held constant during heat–treatment of all films (600 ºC) and therefore, the occurrence of SnO and Sn_3O_4 cannot be attributed to differences in temperature. The same holds for the

atmosphere (i.e., all films were heat–treated in air). Close inspection of the diffractograms reveals that the SnO phase is present in all Ni–doped samples (see the peak ca. 51º), although the relative proportion is different, except for the film produced from [Ni(II)]/[Sn(IV)] 15:85 molar ratio. For this film, the Sn_3O_4 phase is clearly detected. Note that the amount of Ni^{2+} dissolved in the tin oxide lattice is the maximum for this film. Hence, it seems that the occurrence of SnO and Sn_3O_4 phases is linked to the introduction of Ni^{2+} in the material, although the relationship is somewhat complex.

No peaks related to either metallic Ni or NiO are present. This suggests that Ni has entered the SnO_2 lattice. However, the SnO_2 peaks in the diffractograms of the Ni–containing films are not shifted compared to the undoped sample. This can be explained considering the nearly equal ionic radius of Ni^{2+} (0.69 Å) and Sn^{4+} (0.69 Å).[22] The crystallite size of the SnO_2 phase, together with the microstrains and cell parameters, were calculated using the Rietveld method (Table 3.2.1). When compared to the undoped sample, the crystallite size decreases in the doped films, although not in a monotonous manner. In turn, the microstrains increase by one order of magnitude, indicating that the incorporation of Ni in the SnO_2 framework induces some strain. Although the lattice parameters '*a*' and '*c*' do not show pronounced variations upon Ni doping, '*a*' increases while '*c*' decreases with the introduction of Ni (except for the sample synthesized from the 15:85 [Ni(II)]/[Sn(IV)]).

In order to further investigate the overall crystallographic structure and the eventual occurrence of NiO in the films with the highest Ni content, TEM characterization was carried out. The cross–section images and corresponding SAED patterns of the films containing 5.1 and 8.6 at.% Ni are shown in Fig. 3.2.5 (a) and (b), respectively. Fig. 3.2.5 further confirms that the whole films are entirely porous. However, compared with Fig. 3.2.5 (a), the TEM image of Fig. 3.2.5 (b) shows some darker areas. The SAED patterns from the marked regions (white circles) are shown in the right panels of Fig. 3.2.5 (a) and (b). The two SAED patterns are similar, although a few spots corresponding to NiO phase are indeed detected for the sample synthesized from [Ni(II)]/[Sn(IV)] = 20:80 (with 8.6 at.% Ni). It is worth mentioning that whilst pure mesoporous SnO_2 thin films were already synthesized by EISA in the past, to the best of our knowledge there is only one work reporting on the synthesis of mesoporous NiO thin films using this approach.[23] In that work, poly(ethylene–co–butylene)–block–poly(ethylene oxide) (KLE) was employed as structure–directing agent. Here, both materials (SnO_2 and NiO) coexist in the same mesostructured skeleton.
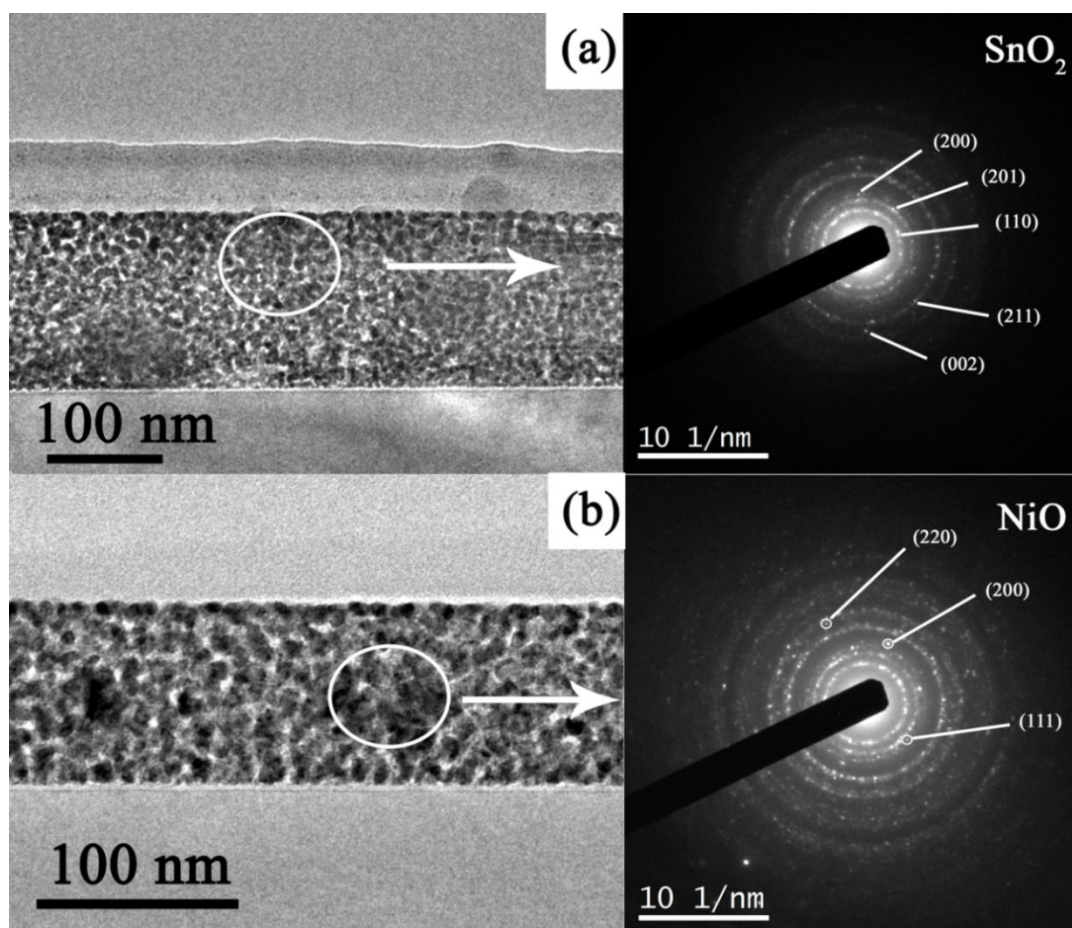
Fig. 3.2.5 TEM images (left) and SAED patterns (right) of the cross–sections of the mesoporous Ni–doped SnO$_2$ thin films with (a) 5.1 at.% Ni, and (b) 8.6 at.% Ni. The indicated planes in (a) correspond to the SnO$_2$ phase whereas only those corresponding to the NiO phase have been indicated in (b) for the sake of clarity.

Detailed HR–TEM images of the mesoporous film with 5.1 at.% Ni and 8.6 at.% Ni are shown in Fig. 3.2.6. The pore walls consist of tiny crystallites, whose interplanar distances match the SnO$_2$ tetragonal structure, in agreement with the XRD and SAED results. Sub–10 nm pores are also clearly visible (as indicated in the figure) and the width of the pore walls is in the 5–10 nm range. The size of the crystallites agrees with the results obtained from Rietveld refinement of the XRD patterns (Table 3.2.1). The occurrence of a few NiO clusters immersed in the Ni–doped SnO$_2$ mesoporous film is confirmed for the sample with 8.6 at.% Ni (see Fig. 3.2.6 (b) and (d)).
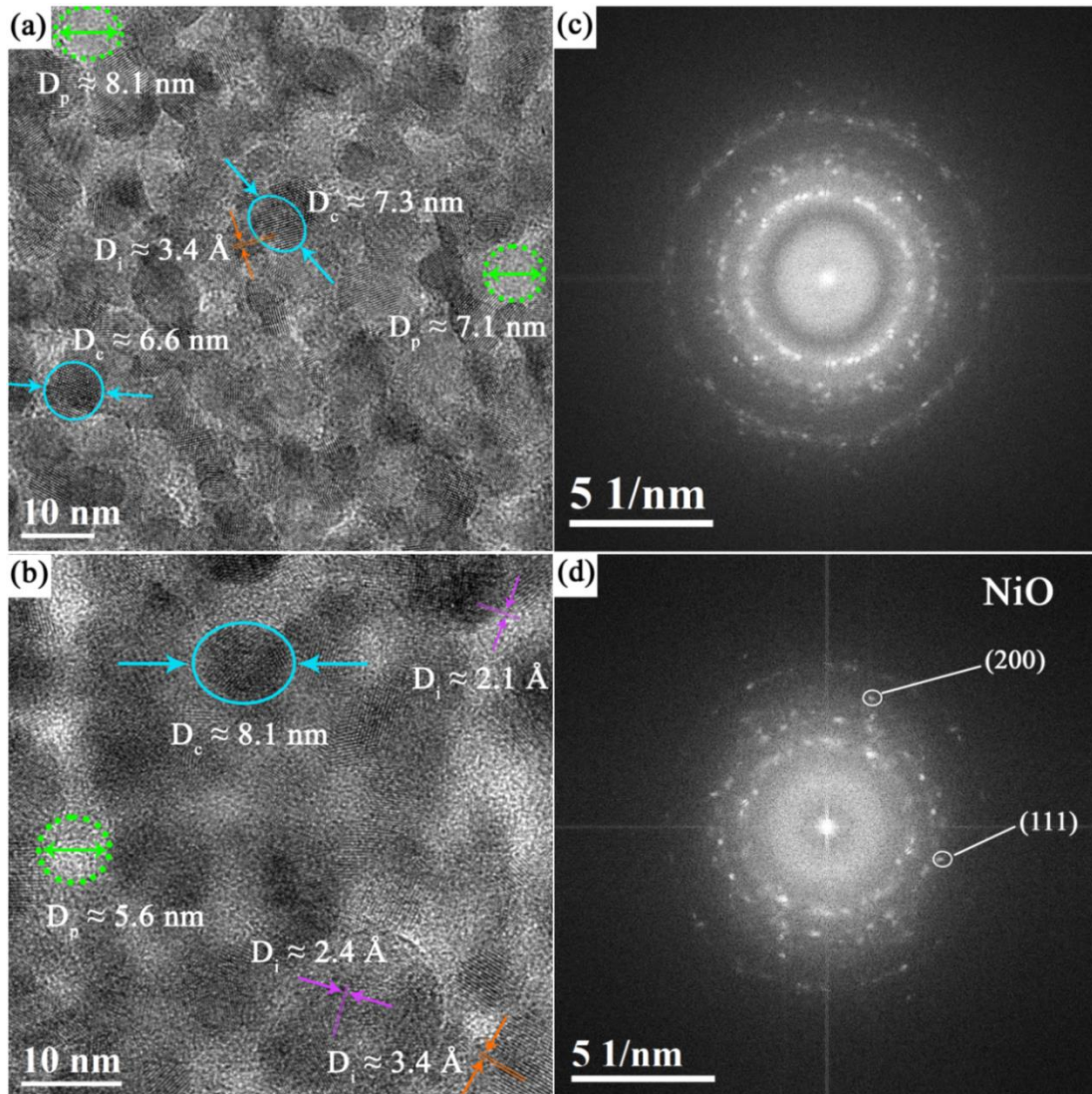
Fig. 3.2.6 HR–TEM image corresponding to the mesoporous films with [Ni(II)]/[Sn(IV)] equal to (a) 15:85 (with 5.1 at.% Ni) and (b) 20:80 (8.6 at.% Ni). D_c denotes the diameter of the crystallites in the pore wall (a couple of them are indicated with blue cyan circles) and D_p indicates the diameter of the pores (two of them indicated with green circles). Orange–coloured D_i represents the interplanar distance in one of the crystallites composing the pore walls ($D_i = 3.4$ Å matches the (110) planes of the tetragonal SnO_2 phase). Purple–coloured D_i corresponds to an interplanar distance of NiO clusters in sample (b). (c) and (d) are the corresponding Fast Fourier Transform (FFT) images of the HR–TEM images shown in (a) and (b), respectively. Some spots corresponding to NiO phase are indicated.

To precisely locate the NiO phase within the SnO_2 network, the films with 5.1 and 8.6 at.% Ni (NiO as a secondary phase was clearly detected by SAED in the latter) were selected for EDX mapping and EELS characterization. Fig. 3.2.7 shows the STEM and corresponding EDX mapping of a selected region for these samples.
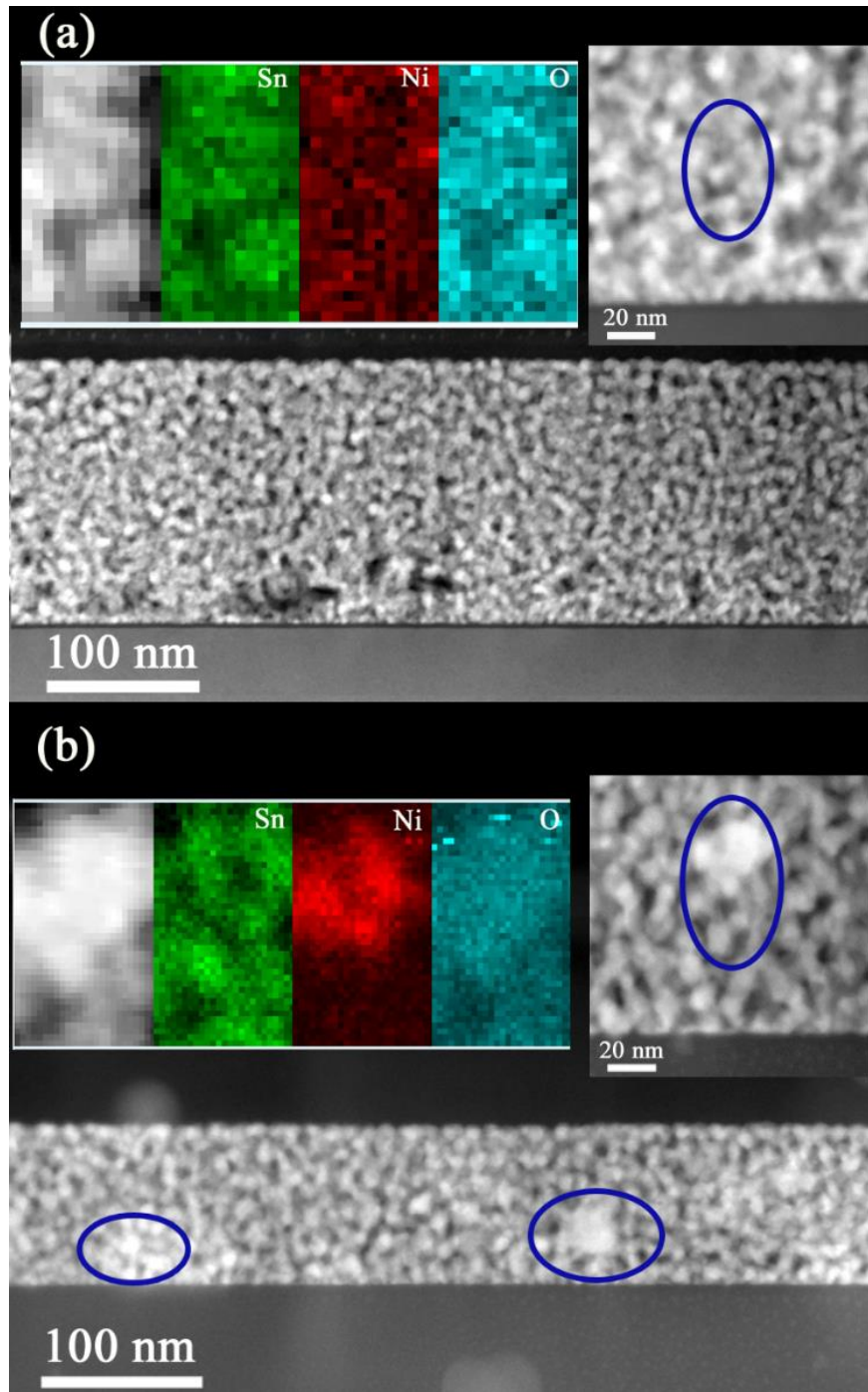
Fig. 3.2.7 Cross–section STEM images (bottom) and elemental EDX mappings (top) of the samples with (a) 5.1 and (b) 8.6 at.% Ni. The distribution of Sn, Ni and O elements correspond to the encircled area shown in the STEM image detail of the upper right panel.

Remarkably, for the mesoporous film with the highest Ni amount, several bright areas (notice that the contrast is the opposite in TEM images) were visible in the film cross–section. EDX mappings of a zoomed detail of the cross–sections were conducted to

determine the distribution of Sn, Ni and O elements (top panel of Fig. 3.2.7 (a) and (b)). In both cases, O and Sn elements are distributed rather homogeneously across the whole area. Ni is also evenly distributed in the film with 5.1 at.% Ni but not in the film with 8.6 at.% Ni. For this sample, Ni preferably accumulates in the brighter area. This result agrees with previous TEM and SAED analyses and suggests that, although no peaks from NiO can be detected by XRD (because their amounts are below the detection limit of the XRD technique), aggregates enriched in Ni of around 20 nm are indeed formed for sufficiently large Ni contents. Note that these aggregates do not apparently show a mesoporous structure (see Fig. 3.2.5 (b) and 3.2.7 (b)). The aggregates are denser, which is very clear from the cross–section STEM images. Hence, the formation of these aggregates partially disrupts the long–range order mesostructure of SnO_2. This is the reason why their size is larger than the pore wall thickness of SnO_2.

3.2.2 XPS analysis

To shed light on the valence state of Ni and the occurrence of oxygen vacancies in the Ni–doped mesoporous films, XPS characterization was carried out. Fig. 3.2.8 (a) shows the survey spectra of all samples including undoped SnO_2, taken as a reference sample. The corresponding core–level Sn 3d is displayed in Fig. 3.2.8 (b). The peaks belonging to Sn $3d_{5/2}$ and $3d_{3/2}$ located at ~486.1 eV and ~495.5 eV are assigned to SnO_2.[24,25] A slight shift toward higher binding energies is noted for the films with the highest Ni contents (5.1 and 8.6 at.%).

As shown in Fig. 3.2.8 (c) and (d), the O 1s spectrum for the samples containing 5.1 and 8.6 at.% Ni can be deconvoluted into three main bands centred at 529.58 eV, 530.25 eV and 531.66 eV. The peaks located at 529.58 eV and 530.25 eV are attributed to O^{2-} anions in the SnO_2 (and NiO) lattice,[8,9,26] whereas the peak at 531.66 eV is associated with O ion in oxygen deficient regions or oxygen vacancies in the lattice.[27] This peak might be also attributed to hydroxyl groups. Actually, assignation to both adsorbed oxygen (OH^- groups) on the surface or oxygen vacancies is stated by some authors.[28,29] However, when compared with undoped SnO_2 film, there is a clear shift of the O 1s peak toward higher binding energy, suggesting that the Ni incorporation into SnO_2 structure gradually generates oxygen vacancies up to 5.1 at.% Ni (see Fig. 3.2.9 (a)).
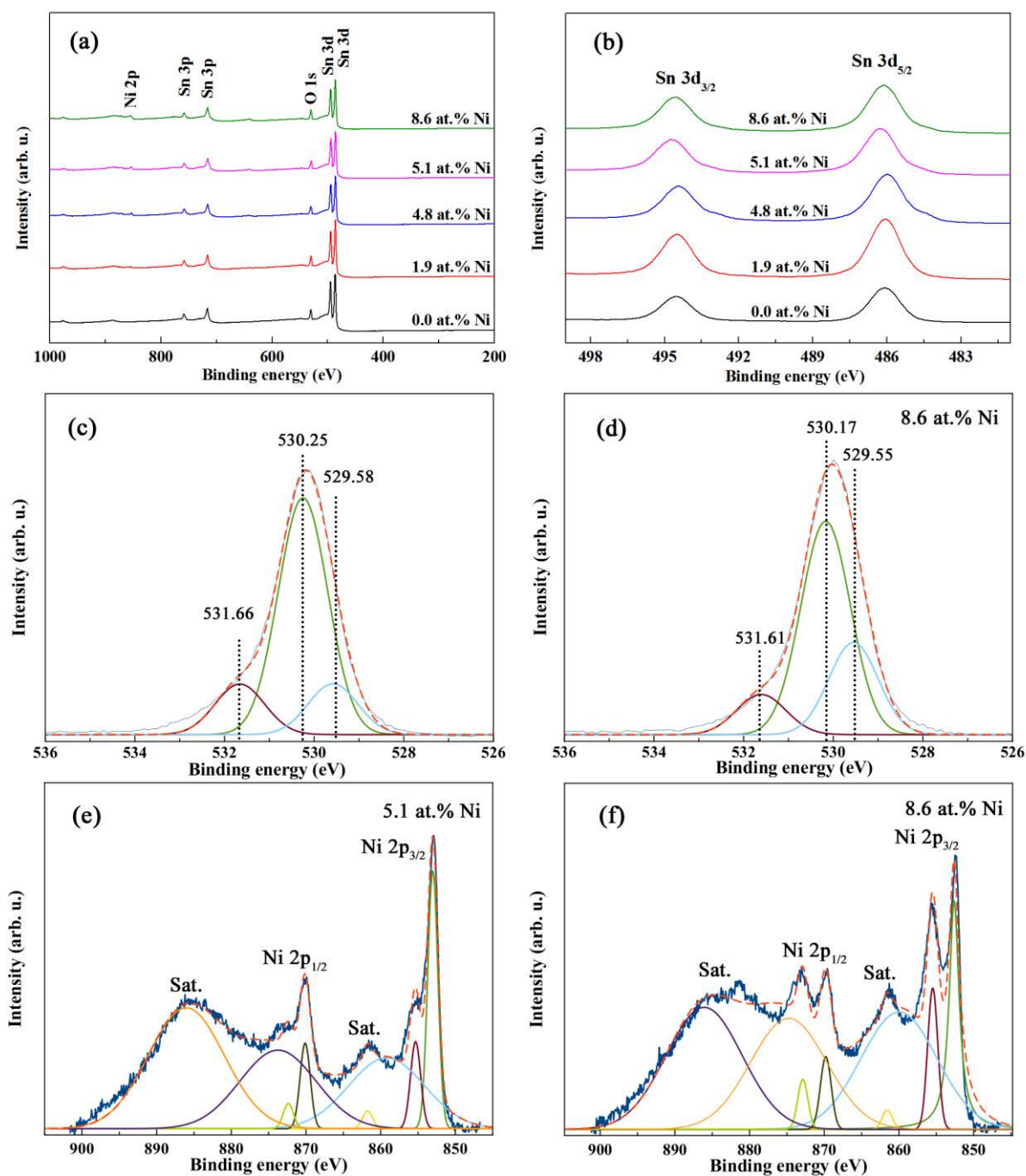
Fig. 3.2.8 (a) General XPS survey spectra of undoped and Ni–doped SnO$_2$ mesoporous films, (b) High–resolution XPS spectra of Sn 3d. The corresponding deconvolution of O 1s [(c) and (d)] and Ni 2p [(e) and (f)] is shown for the films with 5.1 and 8.6 at.% Ni, respectively. "Sat." denotes satellite peaks.

The corresponding Ni 2p core–level XPS spectra for the samples containing 5.1 and 8.6 at.% Ni are shown in Fig. 3.2.8 (e) and (f), respectively (see spectra for all samples in Fig. 3.2.9 (b)). In this case, the profiles show some remarkable differences. In particular, the peak contribution with a binding energy around 855.5 eV (Ni 2p$_{3/2}$) assigned to Ni^{2+} in NiO

102

notoriously increases in Fig. 3.2.8 (f) compared to Fig. 3.2.8 (e) (see also Table 3.2.2). This agrees with both the observed increase in the total amount of Ni incorporated into the film and the formation of relatively large NiO particles. Besides, the Ni $2p_{3/2}$ peak located at ~530.0 eV could be attributed to monovalent Ni species.[30,31] Therefore, Ni possesses a mixed valence state of 1+/2+.
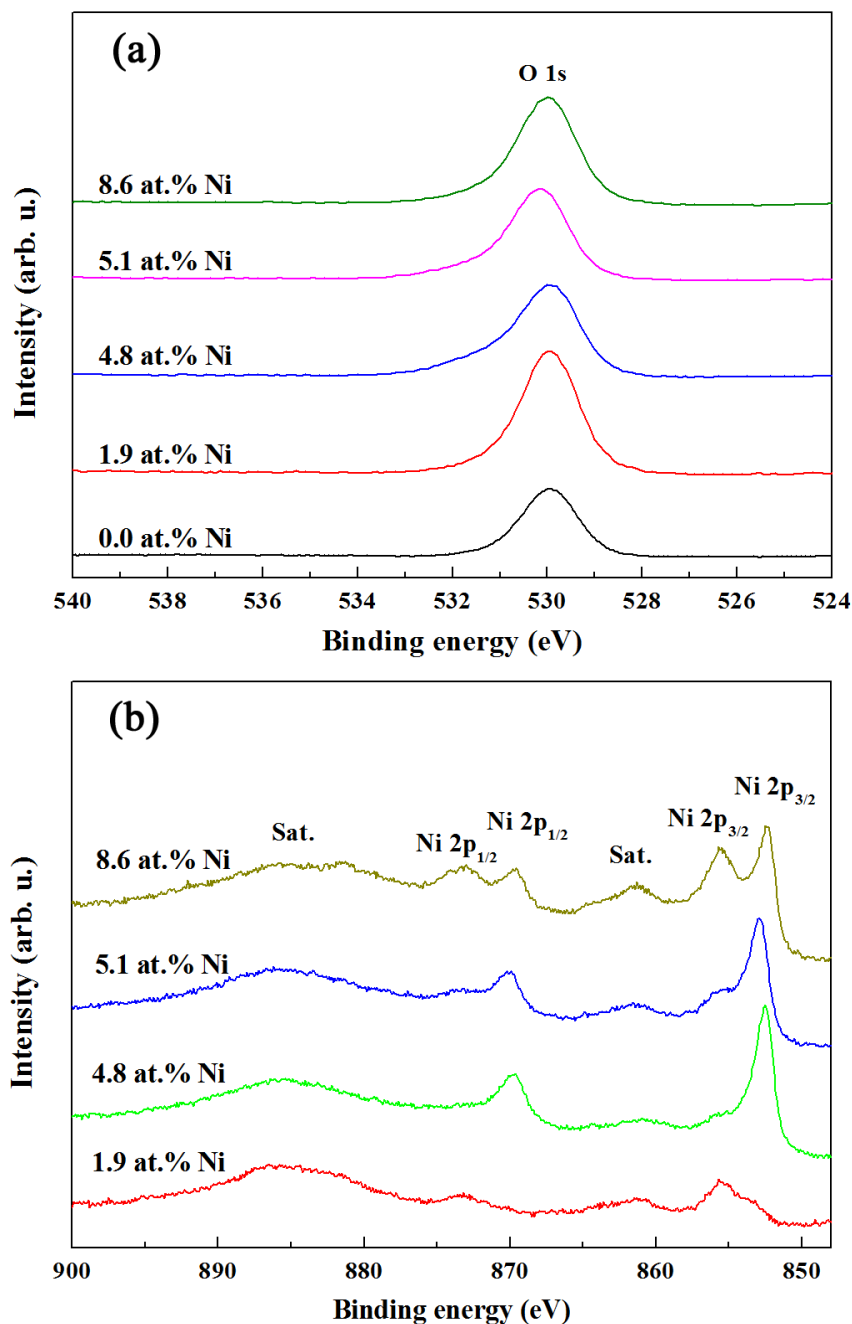
Fig. 3.2.9 High–resolution XPS spectra of (a) O 1s and (b) Ni 2p for all the investigated samples.

Actual Ni content (from XPS) (at.%)	Valence state	Binding energy (eV) 2p$_{3/2}$	Binding energy (eV) 2p$_{1/2}$
5.1	Ni^{1+}	852.9	870.1
	Ni^{2+}	855.3	872.4
8.6	Ni^{1+}	852.6	869.8
	Ni^{2+}	855.5	872.9

Table 3.2.2 Binding energy of the spectral fitting for Ni 2p$_{3/2}$ and Ni 2p$_{1/2}$.

3.2.3 Magnetic properties of Ni–doped SnO$_2$ films

The magnetic properties of the samples with varying Ni concentration were first studied by acquiring hysteresis loops at room temperature and subtracting the signal from the bare substrates. As shown in Fig. 3.2.10, the undoped SnO$_2$ film exhibits a diamagnetic behaviour (negative magnetization *vs.* field slope), in agreement with previous studies on this type of oxide semiconductors.[32] Conversely, a clear (positive) paramagnetic slope dominates the magnetic behaviour of the samples with the highest Ni amounts (5.1 and 8.6 at.% Ni). This positive slope can be attributed to the presence of NiO clusters, as evidenced by EDX and EELS analyses.
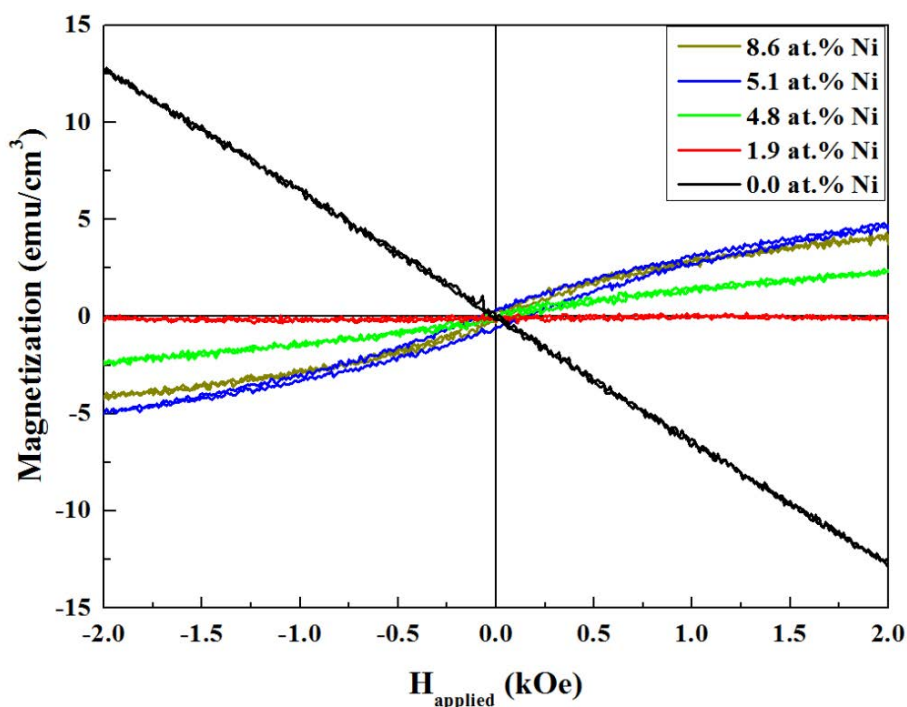
Fig. 3.2.10 Magnetic hysteresis loops of undoped and Ni–doped SnO$_2$ mesoporous films at room temperature. Long moment refers to in–plane magnetization.

Note that although bulk NiO is antiferromagnetic with a Néel temperature, T_N, of around 520 K, typically T_N is considerably reduced in nanoparticles compared to the bulk. Superimposed to this positive background, a small ferromagnetic signal is observed. The origin of ferromagnetism in oxide diluted semiconductors is, in fact, a topic of extensive research by many research groups. Contradictory results are easily found in the literature, depending on the material under investigation (bulk, thin films, nanoparticles) and the synthetic procedures, even when the same composition is maintained. In our case, the small ferromagnetic response cannot be attributed to the presence of metallic Ni clusters, since no evidence of their existence were obtained by TEM, XRD or XPS. Conversely, the small ferromagnetic response could be ascribed to the combined effect from the doping TM and the presence of oxygen vacancies, in agreement with previous works on undoped SnO_2 films,[32] TM–doped dense oxide semiconductor films[33],[34] and TM–doped In_2O_3[35,36] and SnO_2 mesoporous powders.[37] Actually, a mechanism based on ferromagnetic exchange interactions mediated by shallow donor electrons trapped in oxygen vacancies was proposed to account for room–temperature ferromagnetism in dilute ferromagnetic oxides and nitrides.[34] Ab–initio energy–band calculations showed later that the donor impurities mainly consisted of hybridized 3d–4s TM–cation electronic states.[38] This model was later confirmed by a number of works, both theoretical and experimental ones.[39,40,41,42] Nonetheless, because of size and surface effects, full understanding of the magnetic properties of the investigated material is not easy. Uncompensated spins from antiferromagnetic NiO aggregates could contribute to some extent to the observed hysteresis behaviour[43] although, as aforementioned, NiO is probably paramagnetic at room temperature. The films with intermediate Ni contents show a virtually zero and small positive magnetization versus applied field slope, respectively. This is due to the interplay between the diamagnetic response from SnO_2 and the paramagnetic background stemming from the secondary NiO phase. Finally, hysteresis loops corresponding to Ni–doped SnO_2 mesoporous films (with 5.1 and 8.6 at.% Ni) were also measured at 100 K, 200 K and 296 K. The results are shown in Fig. 3.2.11. There is a clear increase in the high–field slope in both samples as temperature is decreased. It is well known that in paramagnetic materials, the susceptibility decreases with temperature, following the Curie–Weiss law. That can explain the change in the slope of the hysteresis loops. It could also be that the NiO clusters become truly antiferromagnetic at low temperatures and that could also give rise to an increase of the high–field magnetization, compared to the high–temperature paramagnetic state. Remarkably, the coercivity of the ferromagnetic–like contribution does not show a pronounced temperature dependence. It remains around 40–60 Oe at the three measured temperatures. Hence, the magnetic response contains a soft–ferromagnetic contribution at all temperatures.
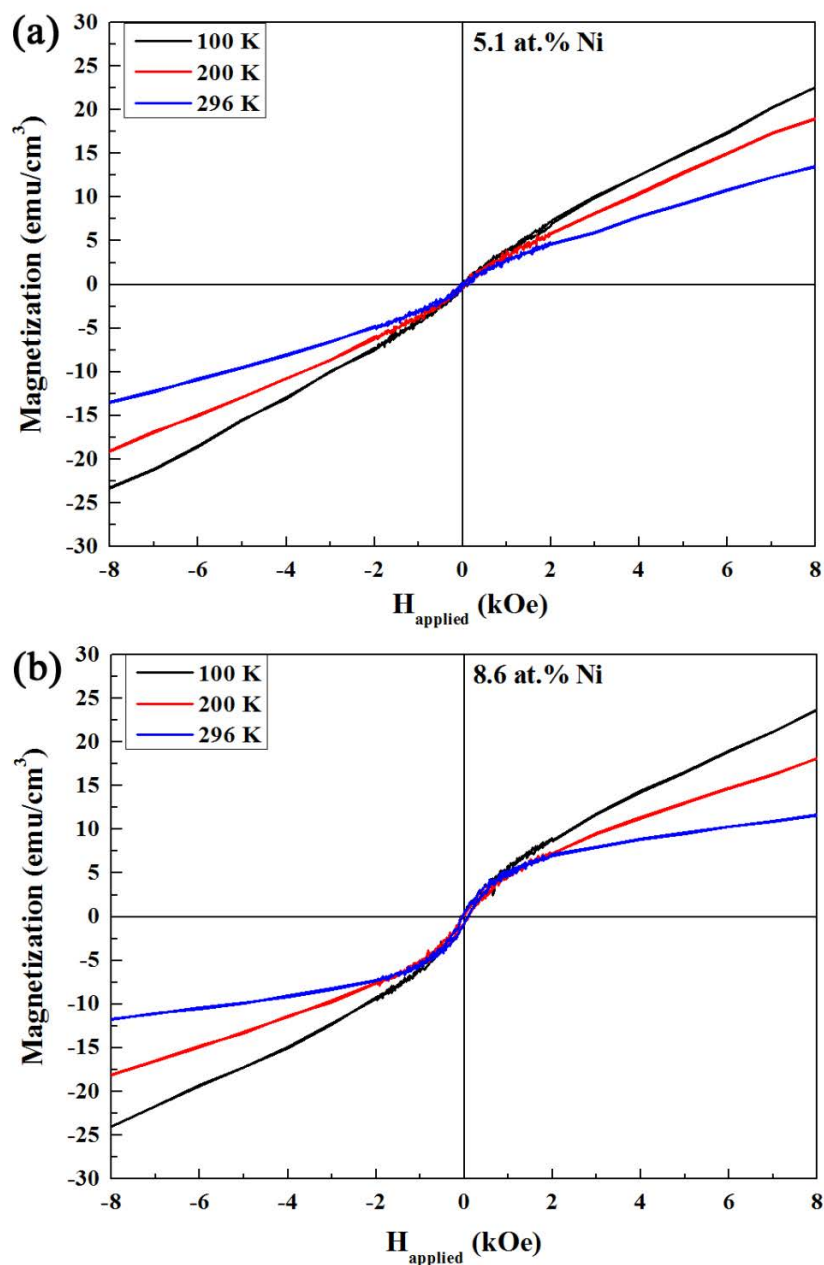
Fig. 3.2.11 Comparison of the hysteresis loops corresponding to Ni–doped SnO_2 mesoporous films (with (a) 5.1 at.% Ni and (b) 8.6 at.% Ni) measured at 100 K, 200 K and 296 K. Long moment refers to in–plane magnetization.

3.2.4 Chapter summary

To summarize, in this section it was shown that undoped and Ni–doped SnO_2 mesoporous films with tunable room–temperature ferromagnetic response can be synthesized by EISA using P–123 as structure directing agent. Truly 3–D nanoporous structures (100–150 nm in thickness), with pore size in the range 5–10 nm, were obtained in all cases. A deep structural characterization revealed that the mesoporous films mainly consist of the rutile–

type tetragonal structure of SnO_2, although NiO clusters also formed in samples with large Ni contents (e.g., 8.6 at.% Ni). X–ray photoelectron spectroscopy experiments indicated lack of metallic Ni and the occurrence of large amounts of oxygen vacancies. From a magnetic viewpoint, the incorporation of Ni drastically changed the magnetic response, from a purely diamagnetic one (undoped mesoporous SnO_2) to a mainly paramagnetic one with a small ferromagnetic contribution (in the samples containing Ni). This work opens up new prospects for the use of mesoporous oxide semiconductor thin films with magnetic characteristics in new types of memory and spintronics devices, which could eventually be controlled by various means (e.g., electrolyte gating).

3.3 Unraveling the origin of magnetism in mesoporous Cu–doped SnO$_2$ magnetic semiconductors

In this section, the nanocasting synthesis of mesoporous Cu–doped SnO$_2$ powders from KIT–6 silica template is demonstrated and the origin of their ferromagnetic behaviour at low and room temperatures investigated by SQUID and XMCD. Similar to Ni–doped powders, the amount of Cu was tuned by varying the [Cu(II)]/[Sn(II)] molar ratio from 0:100 to 20:80 during the infiltration of the silica host. The goal was to disclose to what extent the eventual existence of Fe–based impurities in the resulting powders could explain the magnetic properties of the material or if, otherwise, other effects (e.g. presence of antiferromagnetic CuO or oxygen vacancies) were playing a major role.

3.3.1 Morphological and structural characterization

The morphology of the Cu–doped SnO$_2$ powders was examined by scanning/transmission electron microscopies (SEM/TEM). Fig. 3.3.1 (a), (c), (e) and (g) show the SEM images of samples synthesized from 0:100, 5:95, 15:85 and 20:80 [Cu(II)]/[Sn(II)] molar ratios, respectively. In turn, Fig. 3.3.1 (b), (d), (f) and (h) display their corresponding TEM images.

In all cases, a highly ordered mesoporous arrangement of pores is preserved after the KIT–6 silica template removal. It is noteworthy that Cu–loading does not significantly affect the mesoporous structure of the SnO$_2$ replica. The copper amounts in at.%, determined by energy dispersive X–ray analysis (EDX), for the different samples, are listed in Table 3.3.1. As expected, the Cu contents become larger (from 0 to 7 at.%) when the [Cu(II)]/[Sn(II)] molar ratio increases from 0:100 to 20:80.

[Cu(II)]/[Sn(II)]	Cu content determined by EDX (at.%)	Crystallite size SnO$_2$ phase (nm) (± 1)	a (Å) SnO$_2$ phase (± 1×10^{-3})	c (Å) SnO$_2$ phase (± 1×10^{-3})
0:100	0	9	4.737	3.187
5:95	1	7	4.739	3.189
15:85	5	6	4.739	3.189
20:80	7	7	4.737	3.186

Table 3.3.1 Atomic percentages of Cu assessed by EDX, crystallite size and lattice cell parameters of the SnO$_2$ phase (determined by XRD) of the samples synthesized from [Cu(II)]/[Sn(II)] molar ratios of 0:100, 5:95, 15:85 and 20:80.
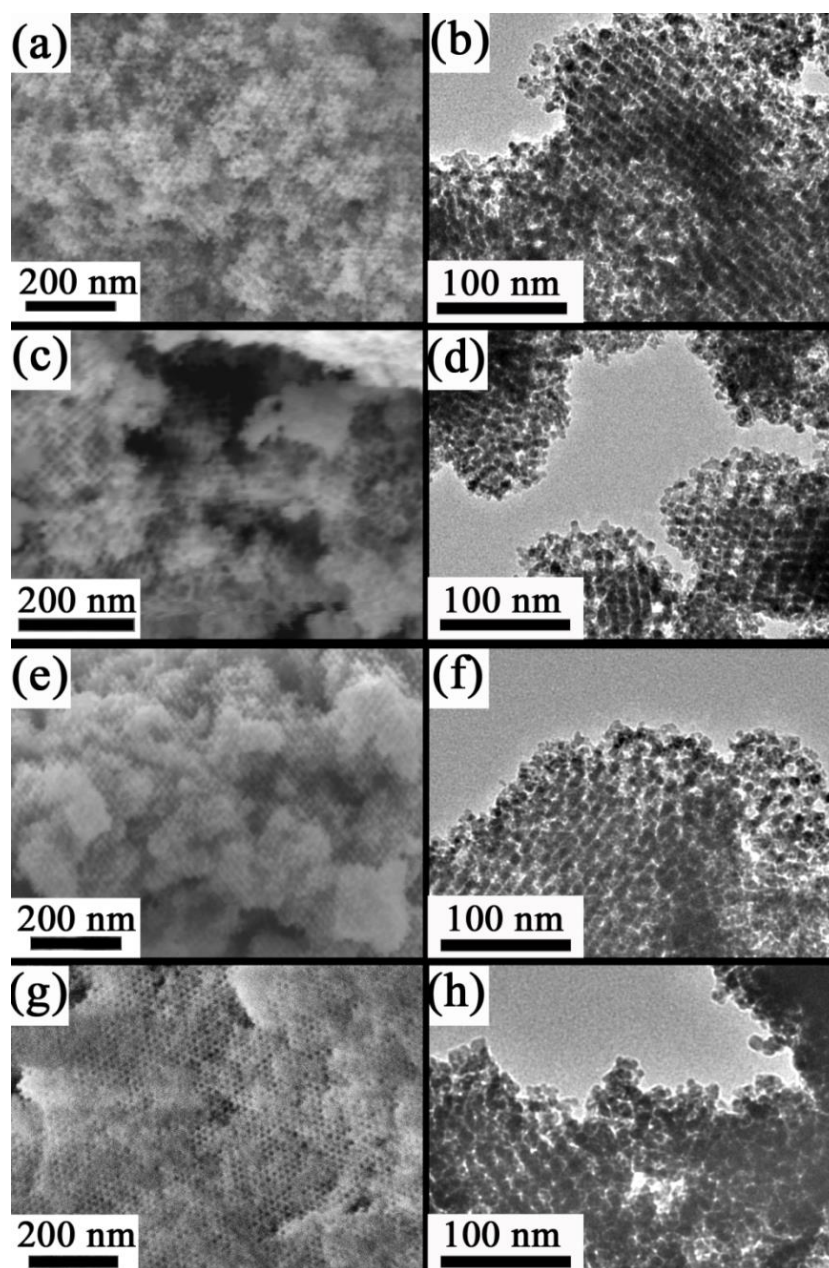
Fig. 3.3.1 Morphology of Cu–doped SnO_2 powders after KIT–6 silica removal. (a), (c), (e) and (g) are the SEM images of the powders obtained from different [Cu(II)]/[Sn(II)] molar ratios (0:100, 5:95, 15:85 and 20:80, respectively). (b), (d), (f) and (h) are their respective TEM images.

To further investigate the microstructure and the crystallographic phases of the samples, XRD analyses were performed. The main XRD peaks correspond to the SnO_2 rutile–type tetragonal phase (JCPDS n° 88–0287). Traces of CuO (JCPDS n° 01–1117) might be envisaged in the 1 at.% Cu doped SnO_2 sample and these XRD peaks become more defined and sharper with further Cu doping, suggesting a formation of a more stoichiometric CuO (Fig. 3.3.2). Information on the crystallite size (average coherently diffracting domain size) and lattice parameters ($a = b$ and c) for SnO_2 was obtained by Rietveld refinement of the

$\theta/2\theta$ XRD patterns (Table 3.3.1). The SnO_2 crystallite size of the samples evidences their nanoscale character, slightly decreasing after Cu doping, in agreement with the formation of a secondary CuO phase. Even though no significant differences are observed in the lattice cell parameters, Cu incorporation into the mesoporous SnO_2 lattice cannot be fully ruled out since the ionic radii of Cu^{2+} and Sn^{4+} are rather similar (0.73 and 0.69 Å, respectively). To further shed light into the structure, the samples were investigated by HR–TEM.
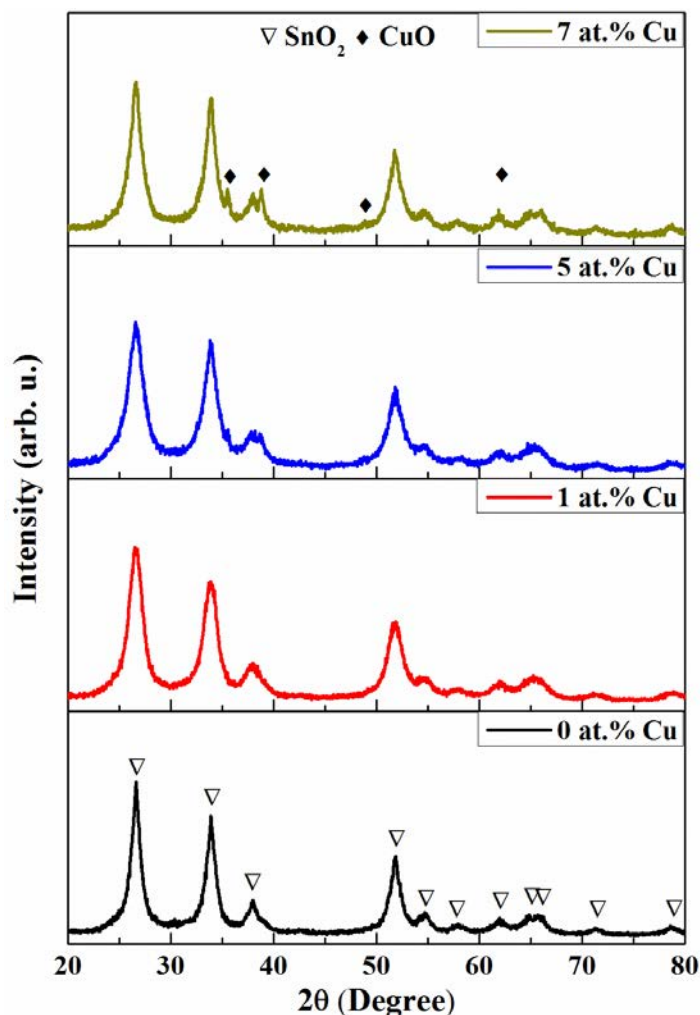
Fig. 3.3.2 XRD patterns of ordered mesoporous Cu–doped SnO_2 powders with 0, 1, 5 and 7 at.% Cu doping.

Fig. 3.3.3, Fig. 3.3.4 and Fig. 3.3.5 show HR–TEM images and the corresponding FFT patterns of the mesoporous SnO_2 samples with different Cu–content (i.e., 1, 5 and 7 at.% Cu). The samples contain highly crystalline SnO_2 nanoparticles of ca. 10 nm with typical interplanar distances of the tetragonal phase (d_{110} = 3.36 Å, d_{101} = 2.65 Å and d_{200} = 2.37 Å). Additionally, the FFT patterns reveal, beside SnO_2, some spots arising from CuO phase [i.e., (100) and (002)], as shown insets of Fig. 3.3.4 and Fig. 3.3.5, in concordance with the XRD results.

110
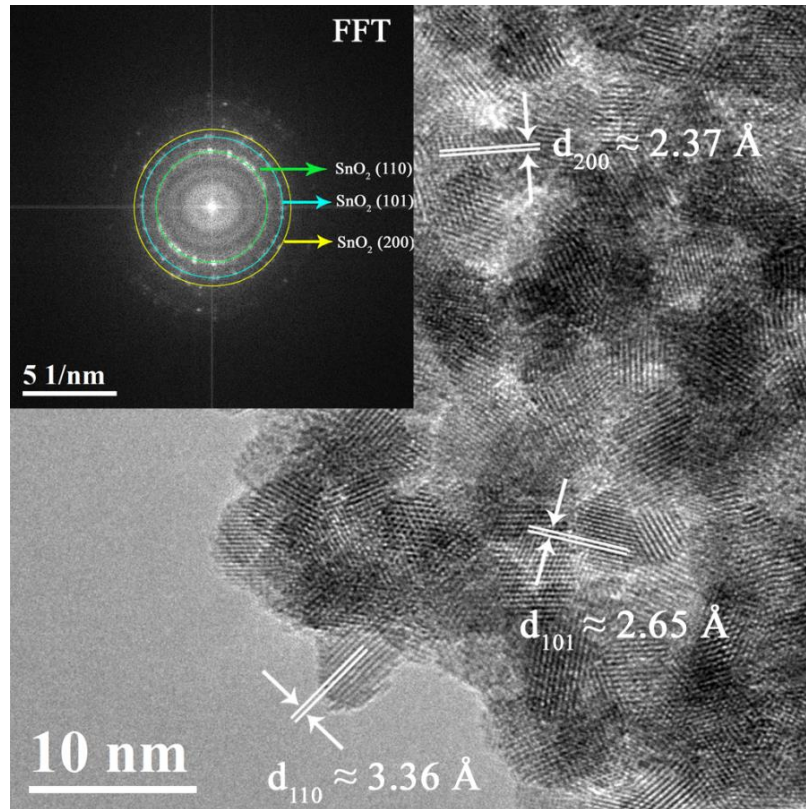
Fig. 3.3.3 HR–TEM image and corresponding FFT of the 1 at.% Cu–doped SnO$_2$ powders.
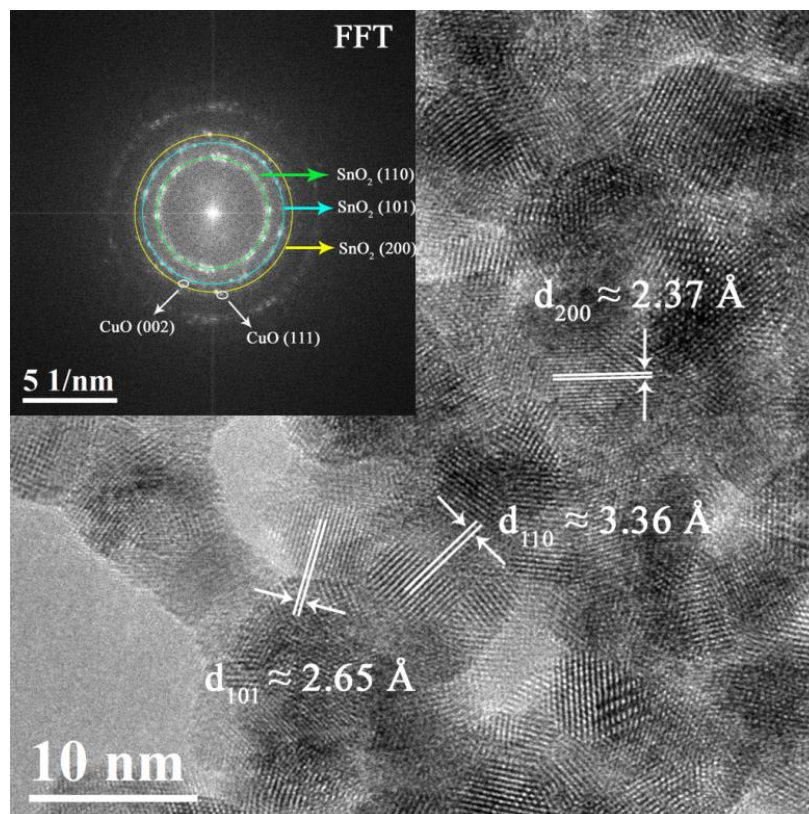
Fig. 3.3.4 HR–TEM image and corresponding FFT of the 5 at.% Cu–doped SnO$_2$ powders.
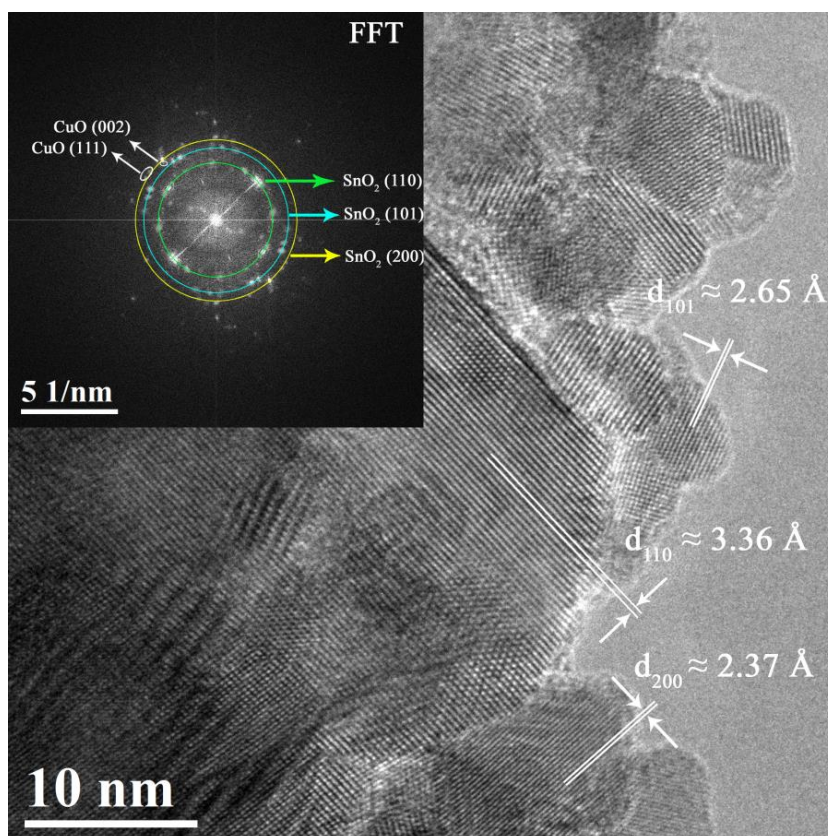
Fig. 3.3.5 HR–TEM image and corresponding FFT of 7 at.% Cu–doped SnO_2 powder.

XPS was used to investigate the valence states of Cu. Because ion bombardment may cause the reduction of CuO to the lower oxide compounds (i.e., Cu^{2+} to Cu^{1+}),[44] XPS was carried out without any pre–sputtering. The general XPS survey spectra are shown in Fig. 3.3.6 (a). Cu 2p peaks emerge and gradually increase with Cu doping. As can be seen in the high–resolution core–level spectra of Cu 2p (Fig. 3.3.6 (b)), Cu $2p_{3/2}$ and Cu $2p_{1/2}$ peaks slightly shift towards higher energies with the increase of doping amount. In addition, a satellite peak centred at around 942 eV appears, and its intensity is also enhanced with the increase of Cu content. Fig. 3.3.6 (c) and (d) show the high–resolution spectra of Cu 2p together with the peak deconvolution of the 1 and 7 at.% Cu samples, respectively. The sample with 7 at.% Cu exhibits a Cu $2p_{3/2}$ binding energy of around 933.6 eV which is consistent with CuO.[45,46] Conversely, for the sample with 1 at.% Cu, the binding energy of Cu $2p_{3/2}$ is 932.9 eV, a slightly lower value, which falls in an energy range characteristic of mixed Cu valence states (i.e., CuO and Cu_2O)[47,48] and, thus, representing a mixture of Cu_2O and CuO. Furthermore, partial non–stoichiometry is likely to be caused by oxygen vacancies associated with the synthesis method,[49,50] as also evidenced in mesoporous transition method–doped In_2O_3 and Ni–doped SnO_2.[35,37]
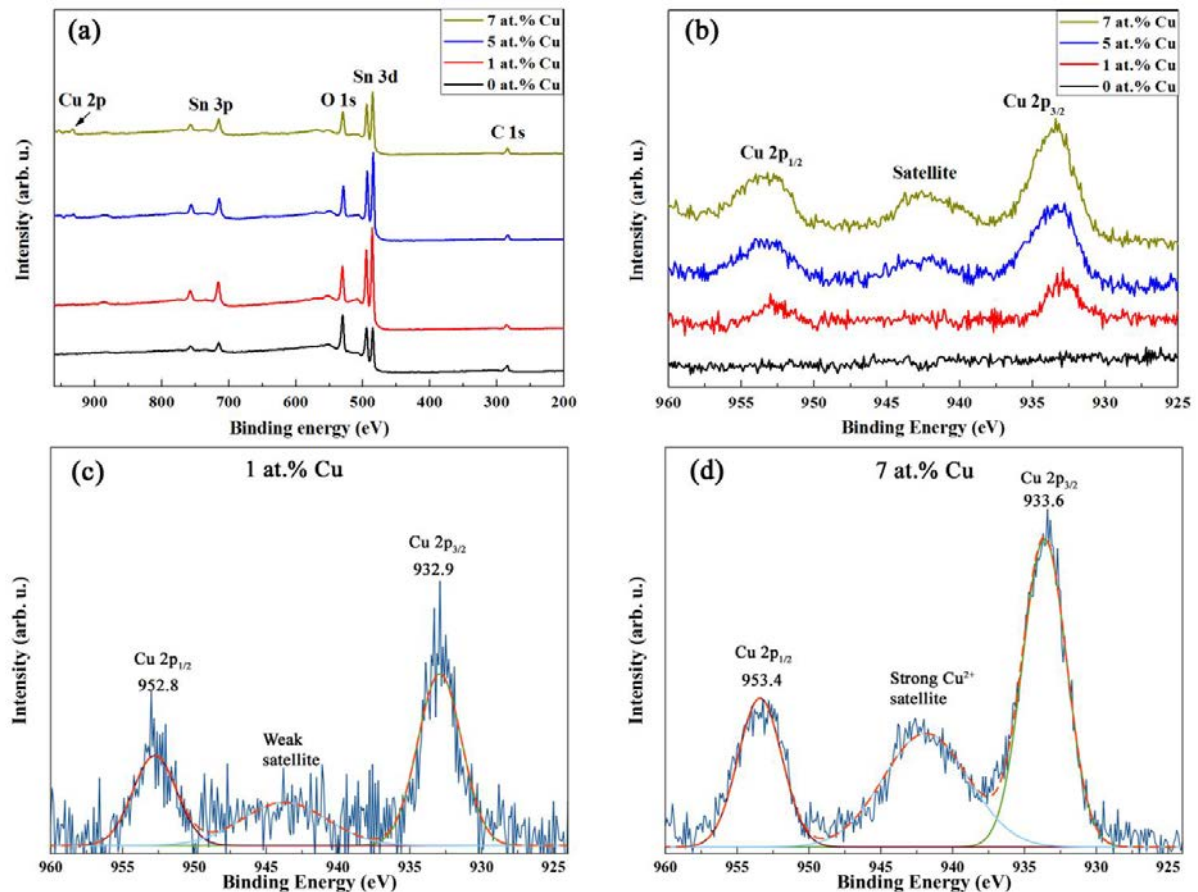
Fig. 3.3.6 (a) General XPS survey spectra of undoped and Cu–doped SnO_2 mesoporous powders, (b) high–resolution XPS spectra of Cu 2p, (c) and (d) are the corresponding deconvolution of Cu 2p in the sample with 1 and 7 at.% Cu, respectively.

3.3.2 Room and low temperature magnetic properties

Fig. 3.3.7 (a) shows the room temperature (RT) magnetization (*M*) vs. applied magnetic field ($H_{applied}$) raw curves recorded by SQUID magnetometry of the mesoporous SnO_2 powders containing 0 (undoped), 1, 5 and 7 at.% Cu. In contrast to the sample with 5 and 7 at.% Cu, the magnetization at high fields of the undoped and Cu–doped (1 at.%) SnO_2 samples decreases with the applied magnetic field, confirming the diamagnetic character of the SnO_2. However, the slope $M/H_{applied}$ of the sample doped with 1 at.% Cu is significantly larger than that of the undoped sample, evidencing a substantial Cu magnetic moment that reduces the total diamagnetic response compared to the pure SnO_2. This would be expected from paramagnetic CuO[51,52] as indicated by traces of CuO XRD peaks in Fig. 3.3.2 and a satellite peak corresponding to the presence of Cu^{2+} in the XPS measurements (Fig. 3.3.6 (c)). In the samples with higher doping levels of 5 and 7 at.% Cu, the diamagnetism of SnO_2 is even overcome resulting in an effective paramagnetic response (positive $M/H_{applied}$ slope at high fields) ascribed to a larger amount of paramagnetic phase (i.e., CuO). This is

in full agreement with the XRD (Fig. 3.3.2) and XPS (Fig. 3.3.6 (d)) results which show clear CuO XRD peaks and a well–defined Cu^{2+} peak, respectively, at the higher doping levels.
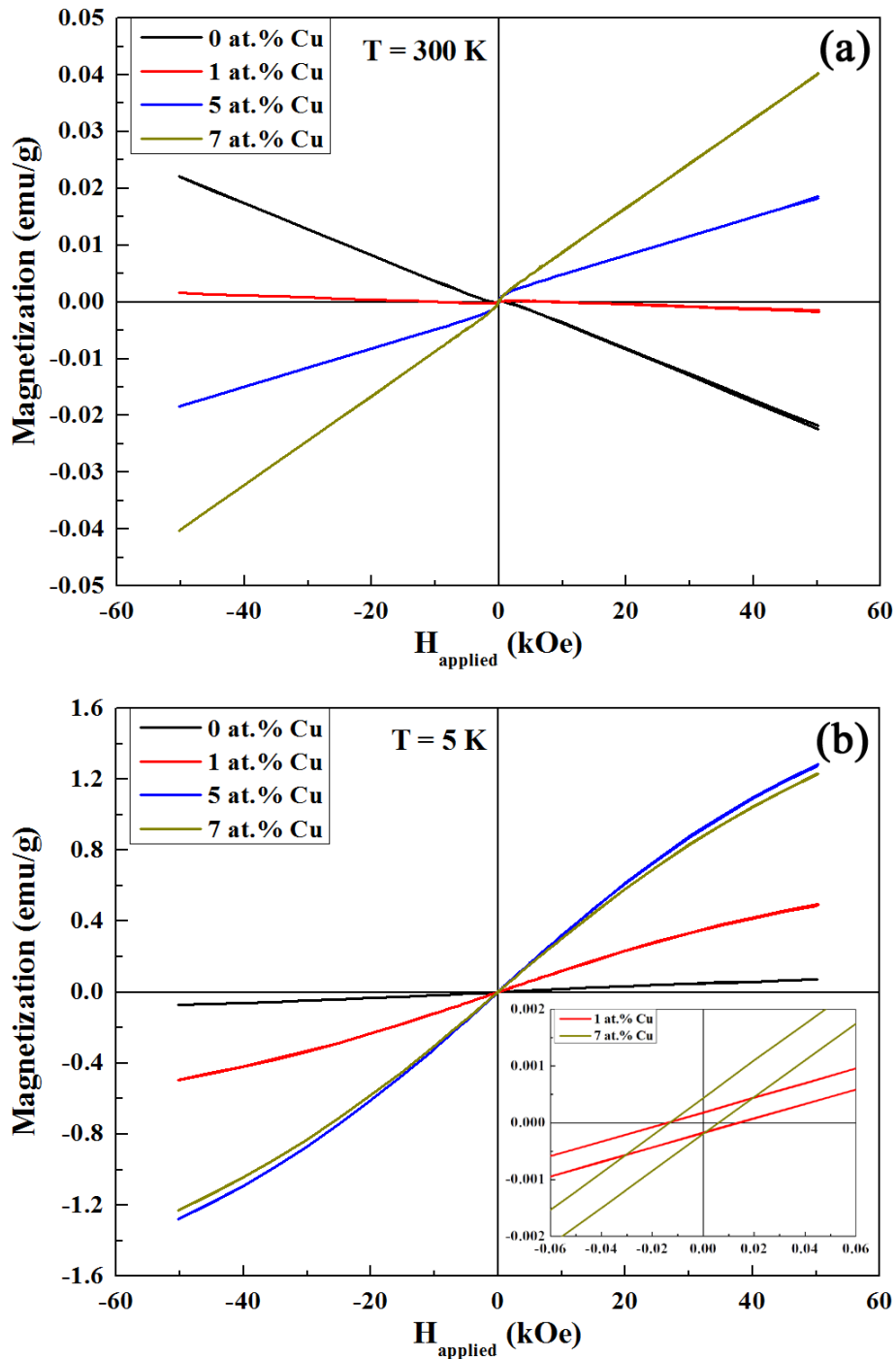
Fig. 3.3.7 (a) Room temperature (300 K) and (b) 5 K SQUID measurements of the ordered mesoporous Cu–doped SnO_2 powders containing 0 (undoped), 1, 5 and 7 at.% Cu. All measurements were recorded under an applied field of 50 kOe. The low temperature hysteresis loops were taken upon cooling from 300 K down to 5 K in an applied magnetic field of 50 kOe. The inset shows the vertical shift of samples doped with 1 and 7 at.% Cu.

All samples exhibit a weak hysteretic behaviour at room temperature superimposed to the diamagnetic or paramagnetic backgrounds, (i.e., mild RT ferromagnetism) whose origin remains rather intricate since no ferromagnetic phases are apparently involved. Some studies point to structural defects (such as oxygen vacancies) as the source of the observed ferromagnetism, [53], [54] whereas other investigations link it to either ferromagnetic contamination, arising from sample handling and/or the impurity of precursors, or instrumental artifacts.[54, 55] Inductively coupled plasma mass spectrometry (ICP–MS) measurements suggests the existence of Fe traces (of the order of a few hundreds of ppm) in all samples, which could explain the room temperature ferromagnetic behaviour. Namely, for instance, after subtracting the linear background of the measurement corresponding to the powders doped with 7 at.% Cu, a saturation magnetization (M_s) of around 9.5×10^{-4} emu/g is obtained. Upon assumption that ferromagnetism solely arises from Fe contamination (M_s of 217.2 emu/g at 298K),[56] just 33 ppm of Fe would be sufficient to obtain that M_S. However, the lack of information on the Fe distribution and morphology does not allow us to be completely conclusive on this issue, hence leaving the origin of the weak RT ferromagnetism open and possibly related to oxygen vacancies.

Fig. 3.3.7 (b) shows the raw SQUID measurements of the mesoporous SnO_2 powders containing 0 (undoped), 1, 5 and 7 at.% Cu carried out 5 K after field cooling from RT in an applied magnetic field of 50 kOe. Remarkably, the magnetization at high fields is significantly larger than that at RT (in particular, for the doped samples which contain CuO). For example, upon subtraction of the linear background of the measurement, the powders doped with 7 at.% Cu exhibit a M_s of 0.32 emu/g. This value is more than 300 times larger than that of RT (9.5×10^{-4} emu/g). For metallic bulk iron, the saturation magnetization at 0 K is only 1.02 times larger than that of RT.[56] Therefore, this suggests the presence of another source of magnetic moment rather than iron at low temperature and, the CuO present in the doped samples is a clear candidate as it shows low temperature antiferromagnetic order. Incommensurate helix–like antiferromagnetism is observed below 230 K (Néel temperature T_{N2}) down to 213 K (Néel temperature T_{N1}). Below T_{N1}, CuO shows commensurate antiferromagnetic order.[57] Even though no net magnetization is expected in CuO, low–dimensional (i.e., nanoscale) forms of CuO might give rise to weak ferromagnetism due to size effects.[52,58] Among them, the presence of uncompensated spins at the surface ascribed to low coordination of surface sites and shape–mediated spin canting, as it happens with other antiferromagnets in nanoscale form ($BiFeO_3$ or NiO),[17,59] can result in ferromagnetic–like behaviour. Comparing the magnetization at high fields for the Cu–doped samples, it is clear the signal is much higher for the 5 and 7 at.% Cu powders than for the 1 at.% Cu sample, evidencing that the contribution of uncompensated spins and

spin canting is larger and similar for the 5 and 7 at.% Cu samples. The magnetization of these samples scales with the amount of Cu at room temperature, whereas, at low temperature, the sample with 5 at.% Cu shows a slightly larger saturation magnetization than that of 7 at.% Cu. This phenomenon rules out a spin–1/2 paramagnetic behaviour[60] and, thus, further confirms the presences of magnetic order at low temperature.

A common feature of these nanoscale antiferromagnets is spin frustration which usually results in vertical shifts (in particular upon field cooling from a temperature above the T_N).[61,62] Actually, a little vertical shift of around 3×10^{-4} emu/g towards positive M is observed in the powders with 7 at.% Cu (inset of Fig. 3.3.7 (b)), corroborating size effects in the formed CuO. A vertical shift of the same order of magnitude but slightly weaker is also observed in the sample with 1 and 5 at.% Cu (being smaller in the sample with lower Cu content), whereas the undoped SnO_2 powders exhibit no vertical asymmetry.

To further investigate the origin of the magnetic properties, an element–specific synchrotron technique was employed. Namely, XMCD at the Cu $L_{2,3}$ edge was performed at the UE46_PGM1 beamline (High–Field Diffractometer station of the synchrotron radiation source BESSY II). Since the powders containing 5 and 7 at.% show a similar magnetic behaviour, the samples with 1 and 7 at.% Cu were selected for XMCD measurements.

Fig. 3.3.8 (a) and (c) show the room temperature Cu $L_{3,2}$ edge X–ray absorption (XAS) spectra for right (μ^+) and left (μ^-) circularly polarized light corresponding to the samples with 1 and 7 at.% Cu, respectively, obtained under an applied magnetic field of 50 kOe. Fig. 3.3.8 (b) and (d) represent the XMCD signal, taken as the difference (in arbitrary units) between the right and left circularly polarized spectra presented in (a) and (c), respectively. The XAS spectra of the samples doped with 1 and 7 at.% of Cu (Fig. 3.3.8 (a) and (c), respectively) are consistent with a predominant CuO phase.[63,64,65,66] However, traces of Cu in 1+ valence (peak at around 934.5 eV) are present in the sample doped with 1 at.% of Cu. This is in agreement with the XRD and XPS characterization where only clear crystalline peaks of CuO and a well–defined Cu^{2+} signal are observed in the sample with higher Cu contents. For both samples, the absorption intensity is independent of the light polarization (i.e., no asymmetry in the intensity between the right (μ^+) and left (μ^-) circularly polarized X–ray absorption spectra), indicating no dichroism in copper and, thus, no ferromagnetic behaviour in agreement with the paramagnetic character of the CuO at room temperature.

Fig. 3.3.8 (a), (c) Cu $L_{3,2}$ edge XAS spectra, measured in total electron yield mode for right (+) and left (−) circularly polarized light, recorded at room temperature in an applied magnetic field of 50 kOe for the SnO_2 powders doped with (a) 1 at.% Cu and (c) 7 at.% Cu, respectively. (b) and (d) are the corresponding XMCD signals (i.e., difference between right and left circularly polarized light) for the SnO_2 powders doped with 1 and 7 at.% Cu, respectively.

Conversely, as can be seen in Fig. 3.3.9, there is a pronounced intensity asymmetry between the right (μ^+) and left (μ^-) circularly polarized X–ray absorption spectra for both samples at 5 K, evidencing a significant dichroism in Cu and, consequently, a magnetic moment at the Cu site. The temperature of the measurement (i.e., 5 K) is below the bulk Néel temperatures of the CuO, therefore, even an ordered Cu moment may be anticipated. Due to finite size effects, uncompensated Cu moments as well as spin canting may lead to a net magnetization.

Fig. 3.3.9 (a), (c) Cu L$_{3,2}$ edge XAS spectra, measured in total electron yield mode for right (+) and left (−) circularly polarized light, recorded at 5 K (after cooling in 50 kOe) under an applied magnetic field of 50 kOe for the SnO$_2$ powders doped with (a) 1 at.% Cu and (c) 7 at.% Cu, respectively. (b) and (d) are the corresponding XMCD signals at 5 K (i.e., difference between right and left circularly polarized light) for the SnO$_2$ powders doped with 1 and 7 at.% Cu, respectively.

The presence of ordered Cu moments in contrast to paramagnetic behaviour is further corroborated by the evolution of the XMCD with temperature as shown in Fig. 3.3.10 for the sample doped with 7 at.% Cu. Remarkably, the XMCD signal (i.e., Cu dichroism) has already vanished at 30 K, ruling out a paramagnetic behaviour, and rather indicating a connection with Cu ordering. This, in fact, then indicates a strongly reduced Néel temperature, or, when physical confinement plays a role, a blocking temperature. Hence, the formed CuO is highly affected by size effects in agreement with the structural characterization. There XMCD results suggest an ordered, ferromagnetic–like phase of Cu moments with a finite magnetization. It is to be noted, however, that any possible hysteretic behaviour at low temperature escaped unambiguous detection within the experimental limitations.
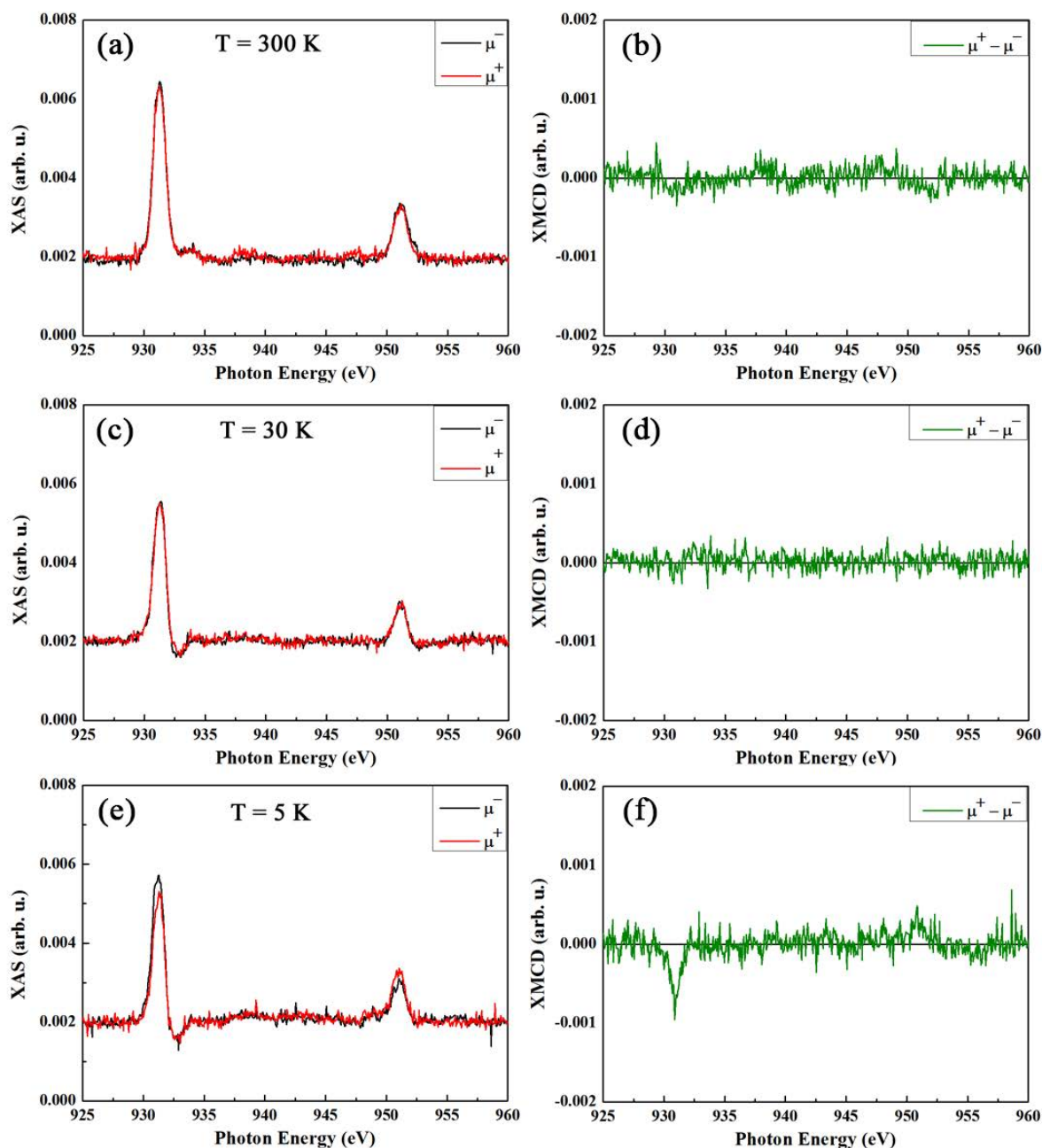
Fig. 3.3.10 Cu $L_{3,2}$ edge XAS spectra of the powders doped with 7 at.% Cu, measured in total electron yield mode for right (μ^+) and left (μ^-) circularly polarized light, recorded at (a) 300 K, (c) 30 K and (e) 5 K under an applied magnetic field of 50 kOe. The cooling was done in 50 kOe. (b), (d) and (f) are the corresponding XMCD signals (i.e., differences between right and left circularly polarized light).

Further support for size effects on this low–temperature ferromagnetic–like response in CuO may be obtained from a quantification of the XMCD. For quantification purposes, the relative XMCD signal, as shown in Fig. 3.3.11, is defined as the amplitude (y_1) between the valley and the peak of the difference between the right and left circularly polarized

119

spectra (i.e., $\mu^+ - \mu^-$) divided by the average of the Cu L_3 absorption peak y_2 ($y_2 = \left(\frac{y_2^- + y_2^+}{2}\right)$). All the calculated values are listed in Table 3.3.2. The presented absorption spectra for both right (μ^+) and left (μ^-) circularly polarized light are the average of two times measurements.
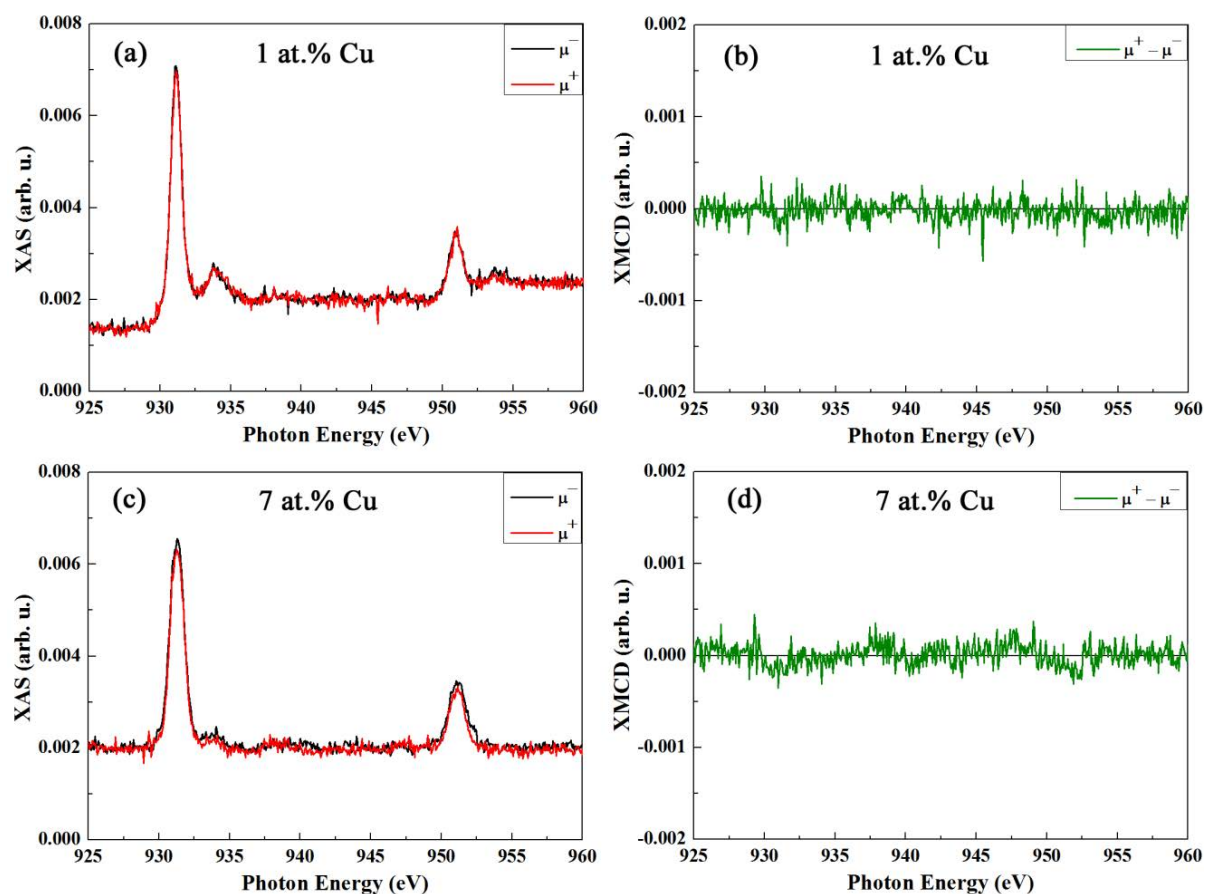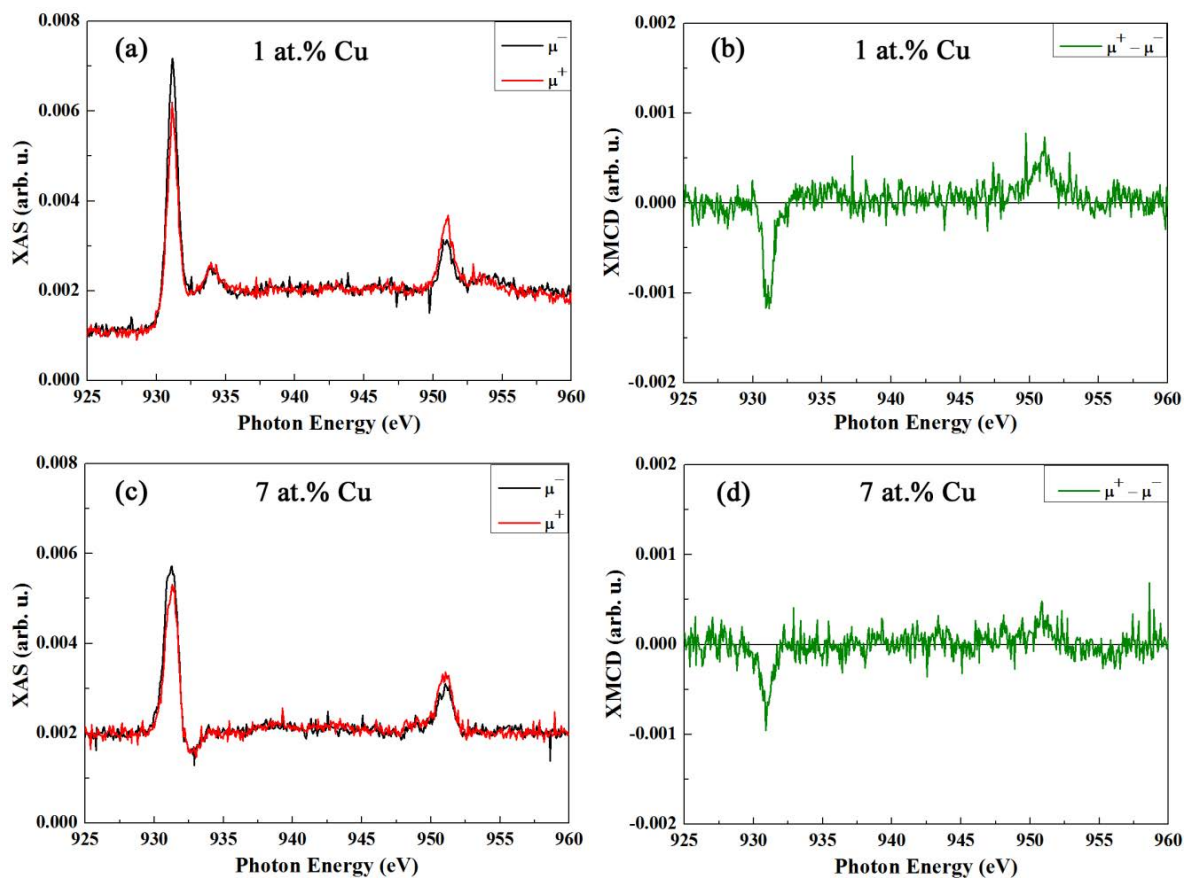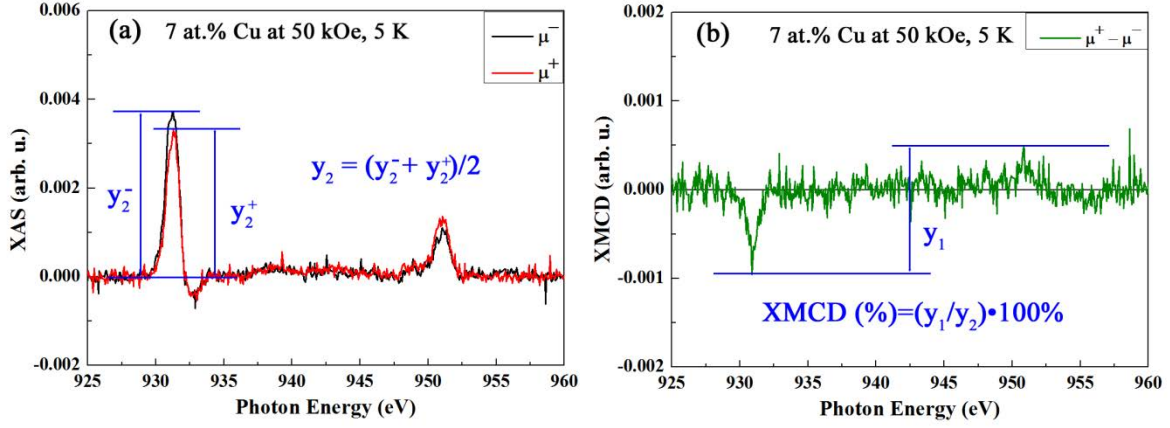

Fig. 3.3.11 (a) Cu $L_{3,2}$ edge XAS spectra, measured in total electron yield mode for right (+) and left (–) circularly polarized light, recorded at 5 K (after cooling in 50 kOe) under an applied magnetic field of 50 kOe for the SnO_2 powders doped with 7 at.% Cu. (b) the corresponding relative XMCD signals (i.e., difference between right and left circularly polarized light). The parameters to quantify the relative XMCD signal are also presented.

	1 at.% Cu		7 at.% Cu	
	50 kOe	**−50 kOe**	**50 kOe**	**−50 kOe**
y_1	1.91×10^{-3}	1.51×10^{-3}	1.42×10^{-3}	0.98×10^{-3}
y_2	5.56×10^{-3}	5.19×10^{-3}	3.55×10^{-3}	3.17×10^{-3}

Table 3.3.2 y_1 and y_2 values for the XMCD signal quantification corresponding to the samples with 1 and 7 at.% Cu measured at 5 K under 50 kOe and −5 kOe.

The XMCD signal quantification is evaluated as follow:

$$\text{XMCD}(\%) = \left(\frac{y_1}{y_2}\right) \cdot 100\ \% \qquad [\text{eq. } 3.1]$$

The error in the relative XMCD signal quantification is propagated assuming dependent errors among the y_1 and y_2 variables, as shown in [eq. 3.2].

$$\delta[\text{XMCD}(\%)] = \left(\left| \frac{1}{y_2} \right| \delta y_1 + y_1 \left| -\frac{1}{y_2{}^2} \right| \delta y_2 \right) \cdot 100\ \% \qquad [\text{eq. 3.2}]$$

Where

$$\delta y_2 = \frac{1}{2}(\delta y_2^+ + \delta y_1^-) \qquad [\text{eq. 3.3}]$$

$\delta y_2{}^+$ and $\delta y_2{}^-$ are taken as half of the amplitude of the background signal which, for both samples, is around 5×10^{-5}. Hence, $\delta y_2 = 5 \times 10^{-5}$. δy_1 is twice δy_2 because it involves the difference of two spectra (i.e., $\mu^+ - \mu^-$). Thus, $\delta y_2 = 1 \times 10^{-4}$.

Table 3.3.3 exhibits the relative XMCD signals of the SnO_2 powders doped with 1 and 7at.% Cu measured at 5 K under 50 kOe and −50 kOe. As expected, the XMCD signal for sample with 7 at.% Cu is larger than for the one with 1 at.% Cu. This is ascribed to the larger amount CuO, probably also more stoichiometric. Note that traces of Cu^{1+} are only observable in the XAS spectra of the sample containing 1 at.% of Cu.

	1 at.% of Cu		7 at.% of Cu	
	50 kOe	**−50 kOe**	**50 kOe**	**−50 kOe**
XMCD ± δXMCD	36 ± 2 %	29 ± 2 %	39 ± 3 %.	33 ± 3 %

Table 3.3.3 XMCD signals and corresponding errors of the SnO_2 powders doped with 1 and 7 at.% Cu measured at 5 K under 50 kOe and −50 kOe.

As aforementioned, a common feature of nanoscale antiferromagnets is to show hysteresis loops with vertical shifts which ultimately stem from size effects. As it happens with the SQUID characterization, the XMCD analysis also reveals this phenomenon. Namely, the XMCD signal at +50 kOe is significantly larger than at −50 kOe (Table 3.3.3), confirming spin frustration upon reversal due to size effects. This is more pronounced in the sample with higher Cu content, suggesting that, at higher doping concentrations, a more stoichiometric CuO phase with a better defined magnetic anisotropy is formed.[67]

3.3.3 Chapter summary

To sum up, ordered mesoporous Cu–doped SnO_2 powders could be satisfactorily prepared by hard–templating from KIT–6 silica. While Fe contamination or the presence of oxygen vacancies could be plausible explanations for the room temperature ferromagnetism, the

low temperature ferromagnetism unambiguously arises from the nanoscale nature of the formed antiferromagnetic CuO which results in a net magnetization (as evidenced by XMCD) due to both uncompensated spins and shape–mediated spin canting. The reduced blocking temperature, which resides between 30 and 5 K, and traces of vertical shifts in the hysteresis loops confirm size effects in CuO. This offers new prospects in the field of spintronics as the amount of surface area–to–volume ratio is highly increased, rendering potential for novel applications that could be based on magnetic surface effects.

References

[1] Z. C. Liu, H. R. Chen, W. M. Huang, J. L. Gu, W. B. Bu, Z. L. Hua and J. L. Shi, Synthesis of a new SnO_2/mesoporous silica composite with room–temperature photoluminescence, *Microporous Mesoporous Mater.*, 2006, **89**, 270–275.

[2] D. K. Pandya, K. Gopinadhan, S. C. Kashyap and S. Chaudhary, On the role of impurities on ferromagnetism in nanocrystalline SnO_2: Ni thick films, *Synth. React. Inorg. Met. Nano–Metal Chem.*, 2008, **38**, 162–167.

[3] P. P. Dorneanu, A. Airinei, M. Grigoras, N. Fifere, L. Sacarescu, N. Lupu and L. Stoleriu, Structural, optical and magnetic properties of Ni doped SnO_2 nanoparticles, *J. Alloys Compd.*, 2016, **668**, 65–72.

[4] S. Lepoutre, J. H. Smått, C. Laberty, H. Amenitsch, D. Grosso and M. Lindén, Detailed study of the pore–filling processes during nanocasting of mesoporous films using SnO_2/SiO_2 as a model system, *Microporous Mesoporous Mater.*, 2009, **123**, 185–192.

[5] J. K. Shon, S. S. Kong, Y. S. Kim, J. H. Lee, W. K. Park, S. C. Park and J. M. Kim, Solvent–free infiltration method for mesoporous SnO_2 using mesoporous silica templates, *Microporous Mesoporous Mater.*, 2009, **120**, 441–446.

[6] T. Waitz, B. Becker, T. Wagner, T. Sauerwald, C. D. Kohl and M. Tiemann, Ordered nanoporous SnO_2 gas sensors with high thermal stability, *Sensors Actuators, B Chem.*, 2010, **150**, 788–793.

[7] D. L. Hou, H. J. Meng, L. Y. Jia, X. J. Ye, H. J. Zhou and X. L. Li, Oxygen vacancy enhanced the room temperature ferromagnetism in Ni–doped TiO_2 thin films, *Phys. Lett. A*, 2007, **364**, 318–322.

[8] M. Kwoka, L. Ottaviano, M. Passacantando, S. Santucci, G. Czempik and J. Szuber, XPS study of the surface chemistry of L–CVD SnO_2 thin films after oxidation, *Thin Solid Films*, 2005, **490**, 36–42.

[9] A. Thøgersen, M. Rein, E. Monakhov, J. Mayandi and S. Diplas, Elemental distribution and oxygen deficiency of magnetron sputtered indium tin oxide films, *J. Appl. Phys.*, 2011, **109**, 113532.

[10] B. P. Payne, M. C. Biesinger and N. S. McIntyre, The study of polycrystalline nickel metal oxidation by water vapour, *J. Electron Spectros. Relat. Phenomena*, 2009, **175**, 55–65.

[11] I. S. Mulla, V. J. Rao, H. S. Soni, S. Badrinarayanan and A. P. B. Sinha, Electron spectroscopic studies on films of SnO_2 and SnO_2:Sb, *Surf. Coatings Technol.*, 1987, **31**, 77–88.

[12] A. D. Vogt, T. Han and T. P. Beebe, Adsorption of 11–mercaptoundecanoic acid on Ni(111) and its interaction with probe molecules, *Langmuir*, 1997, **13**, 3397–3403.

[13] A. Lebugle, U. Axelsson, R. Nyholm and N. Mårtensson, Experimental *L* and *M* core level binding energies for the metals ^{22}Ti to ^{30}Zn, *Phys. Scr.*, 1981, **23**, 825–827.

[14] M. C. Biesinger, B. P. Payne, L. W. M. Lau, A. Gerson and R. S. C. Smart, X–ray photoelectron spectroscopic chemical state quantification of mixed nickel metal, oxide and hydroxide systems, *Surf. Interface Anal.*, 2009, **41**, 324–332.

[15] E. Pellicer, M. Cabo, A. López–Ortega, M. Estrader, L. Yedra, S. Estradé, F. Peiró, Z. Saghi, P. Midgley, E. Rossinyol, I. V Golosovsky, A. Mayoral, J. D. Prades, S. Suriñach, M. D. Baró, J. Sort

and J. Nogués, Controlled 3D–coating of the pores of highly ordered mesoporous antiferromagnetic Co_3O_4 replicas with ferrimagnetic $Fe_xCo_{3-x}O_4$ nanolayers, *Nanoscale*, 2013, **5**, 5561–5567.

[16] H. Wang, Y. Yan, X. Du, X. Liu, K. Li and H. Jin, Origin of ferromagnetism in Ni–doped SnO_2: First–principles calculation, *J. Appl. Phys.*, 2010, **107**, 103923.

[17] R. Kodama, S. Makhlouf and A. Berkowitz, Finite size effects in antiferromagnetic NiO nanoparticles, *Phys. Rev. Lett.*, 1997, **79**, 1393–1396.

[18] P. Ravikumar, B. Kisan and A. Perumal, Enhanced room temperature ferromagnetism in antiferromagnetic NiO nanoparticles, *AIP Adv.*, 2015, **5**, 087116.

[19] J. C. Loudon, Antiferromagnetism in NiO observed by transmission electron diffraction, *Phys. Rev. Lett.*, 2012, **109**, 267204.

[20] J. Stöhr, A. Scholl, T. Regan, S. Anders, J. Lüning, M. Scheinfein, H. Padmore and R. White, Images of the antiferromagnetic structure of a NiO(100) surface by means of X–ray magnetic linear dichroism spectromicroscopy, *Phys. Rev. Lett.*, 1999, **83**, 1862–1865.

[21] P. H. Suman, A. A. Felix, H. L. Tuller, J. A. Varela and M. O. Orlandi, Comparative gas sensor response of SnO_2, SnO and Sn_3O_4 nanobelts to NO_2 and potential interferents, *Sens. Act. B. Chem.*, 2015, **208**, 122–127.

[22] K. Barbalace, *Periodic Table of Elements – Sorted by Ionic Radius*, EnvironmentalChemistry.com, (1995–2017). Accessed on–line: 1/3/2017, http://EnvironmentalChemistry.com/yogi/periodic/ionicradius.html.

[23] M. Bernicke, B. Eckhardt, A. Lippitz, E. Ortel, D. Bernsmeier, R. Schmack and R. Kraehnert, Synthesis and OER activity of NiO coatings with micelle–templated mesopore structure, *ChemistrySelect,* 2016, **3**, 482–489.

[24] R. Shiratsuchi, K. Hongo and G. Nogami, Reduction of CO_2 on fluorine–doped SnO_2 thin–film electrodes, *J. Electrochem. Soc.*, 1992, **139**, 2544–2549.

[25] M. Batzill, J. Kim, D. E. Beck and B. E. Koel, Epitaxial growth of tin oxide on Pt(111): Structure and properties of wetting layers and SnO_2 crystallites, *Phys. Rev. B*, 2004, **69**, 165403.

[26] D. L. Legrand, H. W. Nesbitt and G. M. Bancroft, X–ray photoelectron spectroscopic study of a pristine millerite (NiS) surface and the effect of air and water oxidation, *Am. Mineral.*, 1998, **83**, 1256–1265.

[27] R. Noonuruk, W. Mekprasart, N. Vittayakorn, J. Sritharathikhun and W. Pecharapa, Physical, electrical and optical properties of F/Sb codoped SnO_2 synthesized via sonochemical process, *Ferroelectrics*, 2016, **490**, 136–148.

[28] S. K. Alla, R. K. Mandal and N. K. Prasad, Optical and magnetic properties of Mg^{2+} doped CeO_2 nanoparticles, *RSC Adv.* 2016, **6**, 103491–103498.

[29] N. Paunovic, Z. Dohcevic–Mitrovic, R. Scurtu, S. Askrabic, M. Prekajski, B. Matovic and Z. V. Popovic, Suppression of inherent ferromagnetism in Pr–doped CeO_2 nanocrystals, *Nanoscale*, 2012, **4**, 5469–5476.

124

[30] G. D. Park, J. S. Cho and Y. C. Kang, Sodium–ion storage properties of nickel sulfide hollow nanospheres/reduced graphene oxide composite powders prepared by a spray drying process and the nanoscale Kirkendall effect, *Nanoscale*, 2015, **7**, 16781–16788.

[31] S. N. Oliaee, C. Zhang, S. Y. Hwang, H. M. Cheung and Z. Peng, Synthesis and property of a Helwingia–structured nickel nitride/ nickel hydroxide nanocatalyst in hydrazine decomposition, *RSC Adv.*, 2016, **6**, 38494–38498.

[32] G. S. Chang, J. Forrest, E. Z. Kurmaev, A. N. Morozovska, M. D. Glinchuk, J. A. McLeod, A. Moewes, T. P. Surkova and N. H. Hong, Oxygen–vacancy–induced ferromagnetism in undoped SnO_2 thin films, *Phys. Rev. B*, 2012, **85**, 165319.

[33] Y. Matsumoto, M. Murakami, T. Shono, T. Hasegawa, T. Fukumura, M. Kawasaki, P. Ahmet, T. Chikyow, S.–y. Koshihara and H. Koinuma, Room–temperature ferromagnetism in transparent transition metal–doped titanium dioxide, *Science*, 2001, **291**, 854–856.

[34] J. M. D. Coey, M. Venkatesan and C. B. Fitzgerald, Donor impurity band exchange in dilute ferromagnetic oxides, *Nat. Mater.*, 2005, **4**, 173–179.

[35] E. Pellicer, M. Cabo, E. Rossinyol, P. Solsona, S. Suriñach, M. D. Baró and J. Sort, Nanocasting of mesoporous In–TM (TM = Co, Fe, Mn) oxides: towards 3D diluted–oxide magnetic semiconductor architectures, *Adv. Funct. Mater.*, 2013, **23**, 900–911.

[36] E. Pellicer, E. Menéndez, J. Fornell, J. Nogués, A. Vantomme, K. Temst and J. Sort, Mesoporous oxide–diluted magnetic semiconductors prepared by Co implantation in nanocast 3D–ordered In_2O_{3-y} materials, *J. Phys. Chem. C*, 2013, **117**, 17084–17091.

[37] J. Fan, J. Zhang, P. Solsona, S. Suriñach, M. D. Baró, J. Sort and E. Pellicer, Nanocasting synthesis of mesoporous SnO_2 with a tunable ferromagnetic response through Ni loading, *RSC Adv.*, 2016, **6**, 104799–104807.

[38] S. Hu, S. Yan, X. Lin, X. Yao, Y. Chen, G. Liu and L. Mei, Electronic structure of Fe–doped In_2O_3 magnetic semiconductor with oxygen vacancies: Evidence for F–center mediated exchange interaction, *Appl. Phys. Lett.*, 2007, **91**, 262514.

[39] A. M. H. R. Hakimi, F. Schoofs, R. Bali, N. A. Stelmashenko, M. G. Blamire, S. Langridge, S. A. Cavill, G. van der Laan and S. S. Dhesi, Origin of magnetism in cobalt–doped indium tin oxide thin films, *Phys. Rev. B*, 2010, **82**, 144429.

[40] A. M. H. R. Hakimi, M. G. Blamire, S. M. Heald, M. S. Alshammari, M. S. Alqahtani, D. S. Score, H. J. Blythe, A. M. Fox and G. A. Gehring, Donor–band ferromagnetism in cobalt–doped indium oxide, *Phys. Rev. B*, 2011, **84**, 085201.

[41] N. H. Hong, J. Sakai, N. Poirot and V. Brizé, Room–temperature ferromagnetism observed in undoped semiconducting and insulating oxide thin films, *Phys. Rev. B*, 2006, **73**, 132404.

[42] D. Bérardan and E. Guilmeau, Magnetic properties of bulk Fe–doped indium oxide, *J. Phys.: Condens. Matter*, 2007, **19**, 236224.

[43] R. H. Kodama, S. A. Makhlouf and A. E. Berkowitz, Finite size effects in antiferromagnetic NiO nanoparticles, *Phys. Rev. Lett.*, 1997, **79**, 1393–1396.

[44] Y. Iijima, N. Niimura and K. Hiraoka, Prevention of the reduction of CuO during X–ray photoelectron spectroscopy analysis, *Surf. interface Anal.*, 1996, **24**, 193–197.

[45] J. P. Espinós, J. Morales, A. Barranco, A. Caballero, J. P. Holgado and A. R. González–Elipe, Interface effects for Cu, CuO , and Cu_2O deposited on SiO_2 and ZrO_2. XPS determination of the valence state of copper in Cu/SiO_2 and Cu/ZrO_2 catalysts, *J. Phys. Chem. B*, 2002, **106**, 6921–6929.

[46] D. E. Diaz–Droguett, R. Espinoza and V. M. Fuenzalida, Copper nanoparticles grown under hydrogen: Study of the surface oxide, *Appl. Surf. Sci.*, 2011, **257**, 4597–4602.

[47] W. Wang, G. Wang, X. Wang, Y. Zhan, Y. Liu and C. Zheng, Synthesis and characterization of Cu_2O nanowires by a novel reduction route, *Adv. Mater.*, 2002, **14**, 67–69.

[48] M. Younas, J. Shen, M. He, R. Lortz, F. Azad, M. J. Akhtar, A. Maqsood and F. C. C. Ling, Role of multivalent Cu, oxygen vacancies and CuO nanophase in the ferromagnetic properties of ZnO:Cu thin films, *RSC Adv.*, 2015, **5**, 55648–55657.

[49] Q. Wu, A. Thissen, W. Jaegermann and M. Liu, Photoelectron spectroscopy study of oxygen vacancy on vanadium oxides surface, *Appl. Surf. Sci.*, 2004, **236**, 473–478.

[50] J. Navas, A. Sánchez–Coronilla, T. Aguilar, N. C. Hernández, D. M. de los Santos, J. Sánchez–Márquez, D. Zorrilla, C. Fernández–Lorenzo, R. Alcántara and J. Martín–Calleja, Experimental and theoretical study of the electronic properties of Cu–doped anatase TiO_2, *Phys. Chem. Chem. Phys.*, 2014, **16**, 3835–3845.

[51] D. J. Keavney, D. B. Buchholz, Q. Ma and R. P. H. Chang, Where does the spin reside in ferromagnetic Cu–doped ZnO?, *Appl. Phys. Lett.*, 2007, **91**, 012501.

[52] A. Punnoose, H. Magnone, M. S. Seehra and J. Bonevich, Bulk to nanoscale magnetism and exchange bias in CuO nanoparticles, *Phys. Rev. B*, 2001, **64**, 174420.

[53] P. S. Vachhani, O. Šipr, A. K. Bhatnagar, R. K. Ramamoorthy, R. J. Choudhary, D. M. Phase, G. Dalba, A. Kuzmin and F. Rocca, Local structure and magnetization of ferromagnetic Cu–doped ZnO films: No magnetism at the dopant?, *J. Alloys Compd.*, 2016, **678**, 304–311.

[54] L. M. C. Pereira, J. P. Araújo, M. J. Van Bael, K. Temst and A. Vantomme, Practical limits for detection of ferromagnetism using highly sensitive magnetometry techniques, *J. Phys. D. Appl. Phys.*, 2011, **44**, 215001.

[55] L. M. C. Pereira, J. P. Araújo, U. Wahl, S. Decoster, M. J. Van Bael, K. Temst and A. Vantomme, Searching for room temperature ferromagnetism in transition metal implanted ZnO and GaN, *J. Appl. Phys.*, 2013, **113**, 023903.

[56] H. Danan, A. Herr and A. J. P. Meyer, New determinations of the saturation magnetization of nickel and iron, *J. Appl. Phys.*, 1968, **39**, 669–670.

[57] Z. Wang, N. Qureshi, S. Yasin, A. Mukhin, E. Ressouche, S. Zherlitsyn, Y. Skourski, J. Geshev, V. Ivanov, M. Gospodinov and V. Skumryev, Magnetoelectric effect and phase transitions in CuO in external magnetic fields, *Nat. Commun.*, 2016, **7**, 10295.

[58] S. R. Mishra, J. Losby, I. Dubenko, S. Roy, N. Ali and K. Marasinghe, Magnetic properties of mechanically milled nanosized cupric oxide, *J. Magn. Magn. Mater.*, 2004, **279**, 111–117.

[59] M. Ramazanoglu, M. Laver, W. Ratcliff, S. M. Watson, W. C. Chen, A. Jackson, K. Kothapalli, S. Lee, S. W. Cheong and V. Kiryukhin, Local weak ferromagnetism in single–crystalline ferroelectric $BiFeO_3$, *Phys. Rev. Lett.*, 2011, **107**, 1–5.

[60] B. D. Cullity and C. D. Graham, *Introduction to Magnetic Materials*, Wiley–IEEE Press, 2nd edn., 2008.

[61] M. J. Benitez, O. Petracic, E. L. Salabas, F. Radu, H. Tüysüz, F. Schüth and H. Zabel, Evidence for core–shell magnetic behavior in antiferromagnetic Co_3O_4 nanowires, *Phys. Rev. Lett.*, 2008, **101**, 097206.

[62] E. C. Passamani, C. Larica, C. Marques, J. R. Proveti, A. Y. Takeuchi and F. H. Sanchez, Exchange bias and anomalous vertical shift of the hysteresis loops in milled Fe/MnO_2 material, *J. Magn. Magn. Mater.*, 2006, **299**, 11–20.

[63] P. Thakur, V. Bisogni, J. C. Cezar, N. B. Brookes, G. Ghiringhelli, S. Gautam, K. H. Chae, M. Subramanian, R. Jayavel and K. Asokan, Electronic structure of Cu–doped ZnO thin films by x–ray absorption, magnetic circular dichroism, and resonant inelastic x–ray scattering, *J. Appl. Phys.*, 2010, **107**, 103915.

[64] J. M. Chen, S. C. Chang, R. S. Liu, J. M. Lee, M. Park and J. H. Choy, Soft–x–ray absorption spectroscopy of heterostructured high–T_C superconducting nanohybrids: X–$Bi_2Sr_2CaCu_2O_8$ [X=I, HgI_2, and $(Py–CH_3)_2HgI_4$], *Phys. Rev. B*, 2005, **71**, 94501.

[65] T. Mizokawa and A. Fujimori, Electronic structure of tetragonal $LaCuO_3$ studied by photoemission and x–ray–absorption spectroscopy, *Phys. Rev. B*, 1998, **57**, 9550–9556.

[66] M. Karppinen, M. Kotiranta, H. Yamauchi, P. Nachimuthu, R. S. Liu and J. M. Chen, O K–edge and Cu L_{23}–edge XANES study on the concentration and distribution of holes in the $(Pb_{2/3}Cu_{1/3})_3Sr_2(Y, Ca)Cu_2O_{8+z}$ superconductive phase, *Phys. Rev. B – Condens. Matter Mater. Phys.*, 2001, **63**, 1845071–1845076.

[67] E. Menéndez, J. Demeter, J. Van Eyken, P. Nawrocki, E. Jedryka, M. Wójcik, J. F. Lopez–Barbera, J. Nogués, A. Vantomme and K. Temst, Improving the magnetic properties of Co–CoO systems by designed oxygen implantation profiles, *ACS Appl. Mater. Interfaces*, 2013, **5**, 4320–4327.
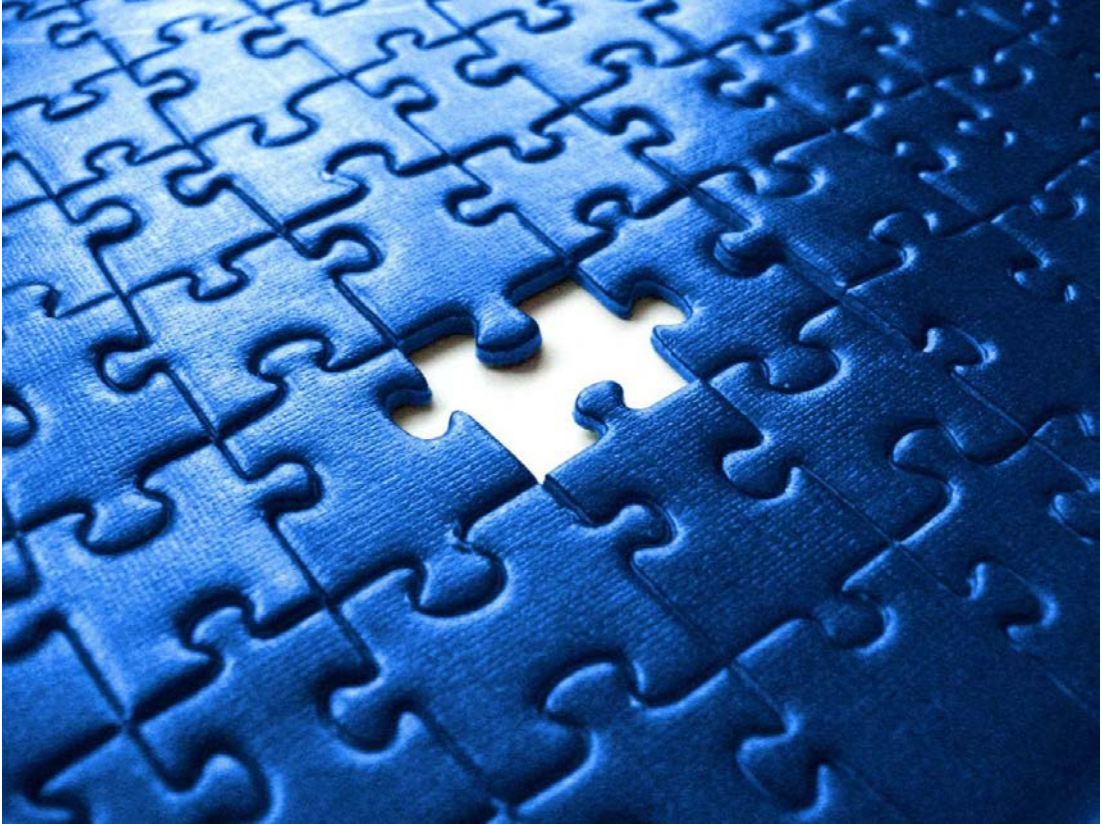
4. General conclusions

General conclusions

In this Thesis, two different fabrication approaches have been followed to produce mesoporous Ni/Cu–doped SnO_2 powders and thin films with ordered mesoporosity, namely: nanocasting and evaporation–induced self–assembly (EISA). The morphology, crystallographic structure, elemental distribution, and oxidation state of Ni and Cu dopants, have been fully investigated. Furthermore, the effect of dopant ions on the resulting magnetic properties of the materials has been explored by different magnetometry techniques.

The following bullet points summarize the conclusions that have been reached:

1. Ni–doped ordered mesoporous SnO_2 powders with minimum amount of residual silica template can be synthesized by nanocasting method. The replicas, with pore size around 10 nm, exhibit tunable room–temperature ferromagnetic response as a function of Ni doping amount (0–9 at.%). The optimum [Ni(II)]/[Sn(II)] molar ratio to guarantee the formation of a fully mesoporous product with the highest saturation magnetization (M_s) is 15:85, which corresponds to 6 at.% Ni.

2. Ni–doped mesoporous SnO_2 films, with thickness about 100–150 nm, can be successfully obtained by EISA method using P–123 as structure directing agent. Truly 3–D nanoporous structures with worm–like pore morphologies and pore sizes in the range 5–10 nm have been obtained. From a magnetic point of view, Ni incorporation drastically modifies the magnetic response of the material, from a purely diamagnetic (undoped SnO_2) to mainly paramagnetic with a small ferromagnetic contribution (for SnO_2 films with the highest Ni content).

3. Similar to the Ni case, Cu can also be introduced as a dopant in mesoporous SnO_2 powders following the nanocasting method, from KIT–6 silica template. The ferromagnetism seen at low temperature mainly arises from the nanoscale nature of the antiferromagnetic CuO nanoparticles formed during the synthetic process. The observed net magnetization is attributed to both uncompensated spins and shape–mediated spin canting.

4. Structural characterization studies have revealed that all Ni– and Cu–doped samples consist of rutile–type tetragonal phase of SnO_2 and no extra phases are present expect for the highest [M(II)]/[Sn(II)] molar ratios used in the synthesis. Since the ionic radii of dopant ions (Ni^{2+}, Cu^{2+}) and Sn^{4+} are similar, no significant changes are observed regarding the lattice parameters.

5. Concerning XPS analyses, all the doped samples contain mixed Ni/Cu valence states (M^{1+} and M^{2+}). This partial non–stoichiometry of the metal oxides is caused by the occurrence of oxygen vacancies associated with the synthesis method and could be also one of the explanations to the observed magnetic properties.

5. Future perspectives

Future perspectives

Although this Thesis has greatly contributed to the progress in the field mesoporous metal oxides–based materials, new exciting perspectives are envisaged on the basis of their potential electronic/magnetic applications. In the following, issues that deserve more attention and directions for future research are briefly overviewed.

❖ Hard template nanocasting method is effective for the preparation of mesoporous materials. However, most studies on mesoporous materials have focused on materials synthetized in powders or thin films. Little effort has been paid to the fabrication of mesoporous nanoscopic materials (e.g. nanowires, nanotubes or nanorods). Taking into account their electrical conductivity, these mesoporous structures have excellent perspective for application in multi–sensory devices in the immediate future.

❖ Using P–123 as the structure directing agent, truly 3–D mesoporous films have been prepared by EISA. This work shows that, based on magnetic surface effects, the surface area–to–volume ratio plays an important role in the magnetic properties. Currently, the fabrication of mesoporous TM–doped mesoporous SnO_2 films with controlled thickness and pore size is under progress. The purpose is to tune the morphology and increase the specific surface. A systematic study of the magnetic response among samples with the same doping level but different specific surface areas could be drawn.

❖ The dip–coating technique used for preparing homogeneous thin films can be exploited to fabricate mesoporous sandwich (or multilayer) structured materials in order to study interface effects. For example, different kinds of mesoporous materials can be integrated layer by layer to obtain semiconductor active materials (e.g., quantum wells and dots). Altogether, this could open up new perspectives for spintronic applications or optical modulation.

❖ XPS analysis reveals that, despite the synthesis process, dopants ions have multiple valences, which, in turn, could be one of the reasons of the observed magnetism. As the valence state is affected by the calcination temperature,[1,2] a systematic study about the influence of calcination conditions on the magnetic response could be carried out.

❖ As mentioned, mesoporous transition metal–doped SnO_2 materials are one of the most promising candidates for the fabrication of diluted magnetic semiconductor devices and even empower a new generation of applications. For this reason, element distribution, oxygen vacancies tuning, and magnetic properties are of special interest. The dopants distribution and magnetic properties have been reported in this Thesis. However, the study on the generation mechanism of oxygen vacancies is rather limited. Moreover, little is known about the conductivity of transition metal–doped mesoporous SnO_2

materials. With these purposes, the oxygen vacancies could be controlled by changing the oxygen partial pressure during the calcination, and the conductivity could be measured by four–probe technique.

References

[1] M. D. Romero, J. A. Calles, A. Rodríguez and J. C. Cabanelas, The influence of calcination treatment over bifunctional Ni/HZSM–5 catalysts, *Ind. Eng. Chem. Res.*, 1998, **37**, 3846–3852.

[2] O. Amadine, Y. Essamlali, A. Fihri, M. Larzek and M. Zahouily, Effect of calcination temperature on the structure and catalytic performance of copper–ceria mixed oxide catalysts in phenol hydroxylation, *RSC Adv.*, 2017, **7**, 12586–12597.

Curriculum vitae

Junpeng Fan

Contact information

- ⊠ Address: Physics Department, Sciences Buiding, C3/202, Universitat Autònoma de Barcelona
- ⊠ City, State: 08193 Bellaterra, Spain
- ⊠ E–mail: junpeng.fan@gmail.com
- ⊠ Mobile phone: +34 657154468

Education

2014–Currently: **PhD of Materials Science**

Universitat Autònoma de Barcelona, Barcelona, Spain.

Group of Smart Nanoengineered Materials, Nanomechanics and Nanomagnetism (Gnm^3)

Supervisor: Prof. Jordi Sort, Dr. Eva Pellicer and Dr. Miguel Guerrero

Place: Física de Materials II, Universitat Autònoma de Barcelona (Barcelona), Spain.

2011–2014: **Master of Material Science**

Shandong University, Shandong province, China

Supervisor: Prof. Xiufang, Bian and A/Prof. Pengchao Si

Place: School of Material Science and Engineering, Shandong University

2007–2011: **Bachelor of Material Engineering**

Shandong University, Shandong province, China

Place: School of Material Science and Engineering, Shandong University

Publications

- ➢ J. Fan, X. Bian, Y. Niu, Y. Bai, X. Xiao, C. Yang, J. Yang and J. Yang, Formation of three–dimensional nano–porous silver films and application toward electrochemical detection of hydrogen peroxide, *Appl. Surf. Sci.*, 2013, **285**, 185–189.
- ➢ J. Fan, J. Zhang, P. Solsona, S. Suriñach, M. D. Baró, J. Sort and E. Pellicer, Nanocasting synthesis of mesoporous SnO_2 with a tunable ferromagnetic response through Ni loading, *RSC Adv.*, 2016, **6**, 104799–104807.
- ➢ J. Fan, M. Guerrero, A. Carretero–Genevrier, M. D. Baró, S. Suriñach, E. Pellicer and J. Sort, Evaporation–induced self–assembly synthesis of Ni–doped mesoporous SnO_2 thin

films with tunable room temperature magnetic properties, *J. Mater. Chem. C,* 2017, **5**, 5517–5527.

➢ J. Fan, E. Menéndez, M. Guerrero, A. Quintana, E. Weschke, E. Pellicer and J. Sort, Unraveling the origin of magnetism in mesoporous Cu–doped SnO_2 magnetic semiconductors, *Phys. Chem. Chem. Phys.,* submitted.

Contributions to Conferences

Junpeng Fan, Pau Solsona, Jin Zhang, Jordi Sort, Eva Pellicer, Ordered mesoporous Ni, Cu doped SnO_2 materials prepared by nanocasting: structure and magnetic properties, *1st Scientific Meeting of BNC–b Students*, May 20–21, 2015. **Poster**

Junpeng Fan, Jordi Sort, Eva Pellicer, Synthesis and potential applications of mesoporous Ni–doped SnO_2: powders versus films, *FEMS Junior Euromat*, July 10–14, 2016. **Oral presentation**

User participation in synchrotron experiments

BESSY II–Helmholtz–Zentrum Berlin
Proposal: 16204243–ST–11–P
Date: 6–12 February 2017
Location: Albert–Einstein–Straße 15, 12489 Berlin (Adlershof), Germany

Skills and Expertise

Preparation of Low–dimensional materials:
Nanocasting, Dip–coating, Ion–beam Sputtering, Magnetron Co–sputtering

Material characterization:
X–ray Diffraction (XRD), Field Emission Scanning Electron Microscopy (FE–SEM), Energy–dispersive X–ray spectroscopy (EDX), Transmission Electron Microscopy (TEM), Atomic Force Microscopy (AFM), Vibrating sample magnetometer (VSM), X–ray absorption spectroscopy (XAS)

Other techniques:
High Vacuum Tube Furnace, Nanoindentation, Electrochemical Workstation (Autolab)

Graph and Data Analysis:
Origin 8.5, X'Pert HighScore, MagicPlotStudent, PyMcaMain, Gatan DigitalMicrograph, TIA, Image J